UNIVERSITY OF LONDON THESIS

Degree PhD Year 2007 Name of Author WILSON, Emma Louise

The interaction of CO with Pd supported on CeO_x ultrathin films

Emma Louise Wilson

Thesis for the degree of Doctor of Philosophy

University College London

University of London

2006

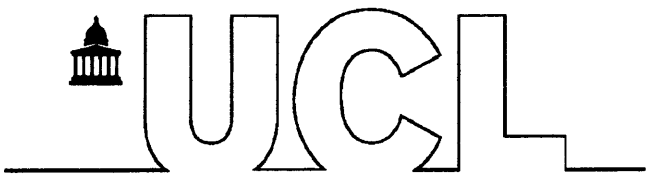

ProQuest LLC
789 East Eisenhower Parkway
P.O. Box 1346
Ann Arbor, MI 48106-1346

Abstract

A key goal in oxide surface science is to determine the mechanism of catalytic reactions at the atomic level. Here we are ultimately interested in CO oxidation over a model automobile catalyst: Pd supported on $CeO_2(111)$ ultrathin films. The degree of reduction (Ce^{3+} concentration) is thought to play an important role in determining the catalyst performance. In this work X-ray photoelectron spectroscopy (XPS) and low energy electron diffraction (LEED) is used to study the degree to which the Ce^{3+} concentration can be varied in $CeO_2(111)$ ultrathin films on Pt(111) and Rh(111) and how they are modified by Pd. Reflection absorption infrared spectroscopy (RAIRS) has also been used to investigate the adsorption of CO on $Pd/CeO_{2-x}/Pt(111)$.

The stoichiometry of three layer $CeO_{2-x}(111)$ grown on Pt(111) has been varied between $CeO_{1.91}$ and $CeO_{1.84}$ by UHV annealing at 970 K. Pd deposition induces an additional reduction of the film, for instance one monolayer equivalent of Pd on $CeO_{1.91}$ changes the stoichiometry to $CeO_{1.87}$. This reduction, which is dependent on the initial stoichiometry, is thought to be due to charge transfer from Pd to CeO_{2-x}. CO adsorbs only in the presence of Pd, independent of the stoichiometry of the original film, without affecting the Ce^{3+} concentration.

Reflection absorption infrared spectroscopy (RAIRS) has been used to investigate the adsorption of CO on CeO_{2-x}-supported Pd nanoparticles at room temperature. RAIRS results show that when CeO_{2-x} is initially grown on Pt(111), a small proportion of the surface remains as bare Pt sites. However, when Pd is deposited onto $CeO_{2-x}/Pt(111)$, most of the Pd grows directly on top of the $CeO_{2-x}(111)$. RAIR spectra of CO adsorption on 1 ML $Pd/CeO_{2-x}/Pt(111)$ show a broad CO-Pd band, which is inconsistent with a single crystal Pd surface. However, the 5 ML and 10 ML $Pd/CeO_{2-x}/Pt(111)$ spectra show vibrational bands consistent with the presence of Pd(111) and (100) faces, suggesting the growth of Pd nanostuctures with well defined facets.

XPS studies of CeO_{2-x} films grown on Rh(111) have also been carried out. It has been shown that by altering the oxygen pressure during Ce deposition the Ce^{3+} concentration of the resultant CeO_{2-x} thin film can be altered by up to 60%, whilst still observing the same LEED pattern. The effect of dosing Pd onto CeO_{2-x} thin films has been shown to be highly dependent on the initial oxidation state of the CeO_{2-x} thin films. On Pd deposition onto $CeO_{1.91}$ and $CeO_{1.84}$ thin films an increase in Ce^{3+} concentration has been observed. However, in direct contrast, a decrease in Ce^{3+} concentration is observed when Pd is deposited on $CeO_{1.71}$ and $CeO_{1.61}$ thin films. CO adsorbs only in the presence of Pd, independent of the stoichiometry of the original film, without affecting the Ce^{3+} concentration.

Acknowledgements

I would like to thank my supervisors, Wendy Brown and Geoff Thornton, for all their help during my PhD.

Many thanks to everyone in the physical chemistry group at UCL for their help, support, and invaluable friendship, which was provided along with lots of cups of tea.

I would also like to thank everyone in technical support for their expertise, especially Dick who revived many old pieces of electronics, independent of the number of times I blew them up.

Special thanks to Dave for putting up with me through the more stressful periods of my PhD, and to my family for supporting me throughout my education.

Publications

RAIRS studies of CO adsorption on Pd/CeO_{2-x}(111)/Pt(111)

E.L. Wilson, W.A. Brown and G. Thornton.

Surface Science 600, 2555 (2006).

In preparation:

CO adsorption on the model catalyst Pd/CeO_{2-x}(111)/Pt(111)

E.L. Wilson, Q. Chen, W.A. Brown and G. Thornton.

XPS studies of CO adsorption on Pd/CeO_{2-x}(111)/Rh(111)

E.L. Wilson, Q. Chen, W.A. Brown and G. Thornton.

Abbreviations

AES	Auger Electron Spectroscopy
AFM	Atomic Force Microscopy
cm^{-1}	Wavenumber
DFT	Density Functional Theory
eV	Electronvolt
FTIR	Fourier Transform Infrared
FWHM	Full Width at Half Maximum
HREELS	High Resolution Electron Energy Loss Spectroscopy
IR	Infrared
L	Langmuir
LEED	Low Energy Electron Diffraction
MCT	Mercury Cadmium Telluride
ML	Monolayer
MLE	Monolayer Equivalent
PED	Photoelectron diffraction
QMS	Quadrupole Mass Spectrometer
RAIRS	Reflection Absorption Infrared Spectroscopy
RFA	Retarding Field Analyser
STM	Scanning Tunnelling Microscopy
TPD	Temperature Programmed Desorption
UHV	Ultra High Vacuum
UPS	Ultraviolet Photoelectron Spectroscopy
XPS	X-ray Photoelectron Spectroscopy

Contents

Figures

Tables

Chapter 1 : Introduction

Metal–oxide interfaces play an important role in many industrial applications, such as metal-oxide mechanical seals, metal-oxide contacts in microelectronics fabrication, and heterogeneous catalysis. Oxide supported metal nanoparticles can also be used as model catalysts. Oxide supports are often used for precious metal catalysts in order to provide the largest possible surface area of the catalytically active metal and to prevent sintering. In some cases the oxide can also act to increase the catalytic activity of the metal [1, 2].

Currently there is only a basic understanding of the mechanisms occurring at metal–oxide interfaces at the atomic level. However, there is a great deal of interest within this area and a large number of studies are being carried out on a variety of different metal/metal-oxide systems [3-7]. The aim of the work presented here is to contribute to this understanding by investigating adsorption and reactions at a metal/metal-oxide interface. This will be achieved by depositing metal nanoparticles on an ordered, well characterised oxide support under ultra high vacuum (UHV) conditions. The interaction of this system with a small probe molecule will be studied using surface science techniques including low energy electron diffraction (LEED), X-ray photoelectron spectroscopy (XPS) and reflection absorption infrared spectroscopy (RAIRS). XPS has been used to identify surface species and to determine the CeO_{2-x} stoichiometry. LEED has been used to determine surface order, and RAIRS has been used to study the interaction of CO with the model catalyst surface and to determine the surface structure of metal nanoparticles deposited on the oxide surface.

The system of interest comprises Pd nanoparticles deposited on $CeO_{2-x}(111)$ thin films grown on Pt(111) and Rh(111) substrates, and the interaction of these surfaces with CO. The main application of this system is in the field of automobile catalysts, of which CeO_2 is a key component [8-10]. CeO_2 was originally included in the automobile catalyst because of its high oxygen

transport and storage capacity [10]. It has since been shown that CeO_2 can also increase the catalytic activity of noble metal particles. For example, it has been shown that CeO_2/Pt is a better CO oxidation catalyst than either of the individual components [2].

Automobile catalysts

Catalysts were first introduced to treat automobile exhausts in the early 1970s. Initially they only dealt with removal of products from incomplete combustion, such as carbon monoxide and residual hydrocarbons [10]. This was done using a single oxidation catalyst that catalysed the oxidation of the products of incomplete oxidation from the combustion engine, in the presence of excess air. Automobile catalysts have evolved considerably since then, and now also aid in the reduction of NO, in what has become quite a chemically complex three-way automobile exhaust catalyst.

Modern three-way automobile catalysts consist of a thin layer of porous material, with the pores axially orientated in the direction of flow of the exhaust gases. 80% of the catalyst is Al_2O_3, which acts as a stabilised support for the noble metals. The remainder is composed of a mixture of rare earth oxides, such as CeO_2, and alkaline earth oxides such as BaO, which provide oxygen for certain reactions. The noble metals rhodium, platinum and/or palladium are only present in small amounts, approximately 1-2% [11].

The main reactions occurring in the three way catalyst are:

$$2CO + O_2 \rightarrow 2CO_2$$ **Equation 1.1**

$$2NO_x \rightarrow N_2 + xO_2$$ **Equation 1.2**

$$C_xH_y + \left(1 + \frac{y}{4}\right)O_2 \rightarrow xCO_2 + \frac{y}{2}H_2O$$ **Equation 1.3**

Cerium oxides were originally added to catalysts to increase the dispersion and stability of the metal component, and to act as an oxygen storage and release component [10]. Hence ceria is able to promote the conversion of NO to N_2, through storage of excess oxygen, and to provide oxygen when required for reaction with carbon monoxide, hydrogen or hydrocarbons. For reactions in which ceria is a source of oxygen, it is thought that the reductant adsorbs on the noble metal, the oxygen is then extracted from the ceria and the reaction between the oxygen and the reductant takes place on the metal [12].

Ceria can be catalytically active for reactions such as CO oxidation [13], however it is believed that contact with a precious metal gives a much more efficient catalyst. Studies of the reaction rate for CO oxidation on ceria supported noble metals show that the observed rate of reaction is much higher than that observed from either of the two elements acting in isolation [2, 13, 14].

Surface science studies of model catalysts

A large variety of experimental and theoretical techniques have been used to study ceria and its role as an automotive catalyst. The most common experimental studies use powdered and mixed samples to carry out rate studies to determine the efficiency of a particular mix of components to catalyse specific reactions [15]. These methods show that the specific mixture of materials used work to catalyse specific reactions, but the actual mechanism of the catalytic reaction on the atomic scale cannot be deduced. In order to determine the mechanisms occurring at metal–oxide interfaces at the atomic level, surface science studies are required. UHV conditions are used in order to eliminate any contaminants and to ensure that only the reactants required are present. In this way the interaction of a small number of the components can be studied individually in order to gain a better understanding of the system as a whole.

A large number of surface science studies on a wide variety of model catalyst surfaces have been carried out, and a number of reviews have been written on the subject [3-7]. Model-catalyst investigations into Pd clusters supported on

various metal oxides, such as TiO_2 [16, 17], Al_2O_3 [5, 7, 18-21], SiO_2 [21, 22], MgO[23] and ZnO [24], have also taken place. RAIRS experiments on CO adsorption on a $Pd/TiO_2(110)$ surface have shown that for Pd coverages above 10 ML, the Pd particles exhibit (111) facets parallel to the substrate. However, for lower Pd coverages, CO-Pd bridge species characteristic of CO adsorption on Pd(110) and (100) facets are observed [16]. STM studies of Pd deposited on $Al_2O_3/NiAl(110)$ at room temperature [25] show that on Al_2O_3, palladium particles grown are cubo-octahedral in shape with a flat (111) top, and (111) and (100) lateral facets.

For Pd particles supported on stoichiometric $TiO_2(110)$ [17] and polycrystalline ZnO [24] there has been no evidence of Pd oxidation, and it has been found that stoichiometric $TiO_2(110)$ is not reduced when Pd is dosed onto the sample surface [17]. However, in an XPS and HREELS study of Al_2O_3-supported Pd it has been shown that reduced alumina surfaces induce a stronger electronic interaction with palladium than with stoichiometric surfaces [18]. This is in agreement with studies of Pt on $TiO_2(110)$ [26], where it was found that there is no charge transfer between Pt and stoichiometric $TiO_2(110)$. However, a decrease in Ti^{3+} ions was observed when Pt was evaporated onto reduced $TiO_2(110)$.

A number of studies into the effect of Rh deposition on CeO_x surfaces have also been carried out [14, 27-40]. Stubenrauch *et al.* [27] used AES to determine that Rh grows as three dimensional particles on $CeO_2(111)$ at 300 K. Pfau *et al.* have also studied Rh/CeO_2 surfaces [40] in order to determine the effects of dosing Rh onto CeO_2 thin films, on the valence band structure. It was found that, as Rh is deposited onto the CeO_2 surface, the Ce^{3+} concentration increases. This was thought to be due to Rh-catalysed desorption of surface oxygen and the creation of positively charged oxygen anion vacancies at the surface.

Cerium dioxide thin films

There is a critical disadvantage in studying CeO_2 using surface science techniques such as electron diffraction, electron spectroscopy and scanning tunnelling microscopy, which is that it has a very low electrical conductivity. The two principal solutions to this problem are to use reduced CeO_2 samples [27] or thin films of CeO_2 grown on underlying metallic substrates. The latter approach is used in the experiments described in this thesis.

A large number of studies have been conducted into the growth of CeO_2 thin films on a range of substrates. Bunluesin *et al.* have grown CeO_2 films on Al_2O_3 by spray pyrolysis resulting in disordered, electrically insulating films [28]. $CeO_2(001)$ films have been grown on $SrTiO_3(001)$ by laser ablation [37, 41, 42]. This method was found to form well ordered, highly crystalline CeO_2. However, the CeO_2 oxidation state could only be altered by Ar ion sputtering of the surface, which is undesirable due to its affect on the surface morphology. Alexandrou *et al.* have formed $CeO_2(111)$ films on Pd(111) by oxidising evaporated Ce [43], and it was shown that these thin films could be reduced by annealing in UHV.

Mullins *et al.* [44] have grown $CeO_2(111)$ thin films on Ru(0001) by evaporation of Ce in an oxygen atmosphere. Stoichiometric CeO_2 and reduced CeO_2 thin films have been obtained by varying the oxygen pressure during Ce deposition. $CeO_2(111)$ thin films grown on Ru(0001) have been successfully used in a number of SXPS and TPD studies on the interaction of small molecules, such as CO and NO, with ceria supported Rh nanoparticles [29, 30, 34-36, 38, 45]. Lu *et al.* [46] have also studied the growth of $CeO_2(111)$ on Ru(0001) using STM. They have developed the method of $CeO_2(111)$ thin film growth used by Mullins *et al.* [44] by increasing oxidation temperatures, resulting in larger, flatter terraces of $CeO_2(111)$.

$CeO_2(111)$ has also been grown on Rh(111) by Ce evaporation in an oxygen atmosphere [47-49], and by Ce evaporation followed by oxidation at elevated sample temperature and oxygen pressure [50]. Eck *et al.* produced a

comprehensive study of CeO_x growth on Rh(111) as a function of temperature and ceria film thickness [49]. STM has shown that deposition of CeO_x at 523 K results in the Rh(111) surface being completely covered after the growth of a 2 layer oxide. The CeO_x has been shown to grow as islands as the film thickness is increased and there is evidence of ordered crystalline structure within the island structures [49]. The CeO_x thin films used by Eck *et al.* have also been successfully reduced by annealing in UHV conditions.

A large number of studies have been carried out on CeO_x(111) grown on Pt(111) [2, 40, 51-57] and a wide variety of different growth methods have been used. Hardacre *et al.* [2, 53] evaporated Ce onto Pt(111) followed by oxidation in O_2, resulting in an ordered film of varying oxidation state dependent on the surface temperature and the amount of O_2 dosed. The method of CeO_x thin film production utilised by the Schierbaum group [40, 52, 54-57] involves evaporation of Ce onto the clean Pt(111) crystal. This is followed by annealing in UHV to produce a Pt-Ce alloy, and then finally annealing in oxygen to produce reduced CeO_2(111)/Pt(111). STM studies [54, 55] showed that the CeO_x forms islands leaving bare Pt sites visible on the surface, however a complete covering of the Pt(111) surface was achieved by repeated Ce deposition and annealing/oxidation cycles [55]. STM also showed crystalline structure within the islands, and concluded that oxygen terminated fluorite-type CeO_x(111) had been produced [55].

The choice of substrate for this study is dependent on a number of factors. A well ordered, single crystal surface is ideal when considering structural effects. The ability to alter the CeO_2 oxidation state is also necessary when considering the effects of the CeO_2 oxygen storage and release capacity on catalytic activity. It has also been shown that the substrate can affect the chemical behaviour of the CeO_2 thin film [58], and hence this should also be taken into consideration. Due to the possible effect of the substrate on the chemical behaviour of the ceria thin films, two different substrates will be used and compared in this thesis. Both Pt(111) and Rh(111) will be used as both have previously been studied

extensively [2, 40, 47-57], and have been well characterised using a variety of techniques including XPS, LEED and STM.

CO adsorption

In this thesis studies of CO adsorption on $Pd/CeO_x(111)$ surfaces will be described. The oxidation of CO is one of the main reactions taking place in automobile catalytic converters, therefore an in depth understanding of how CO interacts with $Pd/CeO_x(111)$ will enable a better understanding of how catalytic activity can be optimised. Experimental studies of how the interactions of CO and Pd with CeO_2 affect its oxidation state will also provide information on the storage and release of oxygen from ceria and how it is altered by other components present in automobile catalysts.

CO also acts as a good probe molecule for RAIRS studies of the Pd/CeO_x surface and the observed CO stretching frequencies can be used to provide information about the Pd/CeO_x surface structure. This allows the morphology of Pd clusters grown on $CeO_x(111)$ to be determined.

A previous TPD investigation of CO adsorption on ceria supported Pt nanoparticles has been carried out [59]. In this study a macroscopically rough, amorphous CeO_2 surface was used. TPD following a saturation exposure of CO at room temperature on the Pt/CeO_2 surface showed two desorption features assigned to CO desorption from Pt(111) and Pt(110) surfaces. As the size of Pt clusters on the CeO_2 surface was increased the CO-Pt(111) related peak became the dominant feature. It was also concluded that the adsorption properties of Pt were not affected by interactions with the CeO_2 support.

A large number of studies of CO adsorption on ceria supported Rh nanoparticles have been carried out [14, 27-33, 39]. Stubenrauch *et al.* [27] studied the adsorption of CO on $Rh/CeO_2(111)$ surfaces at 300 K using TPD. They observed that the main contribution to the TPD spectra was from CO desorbing from low index planes of Rh single crystal surfaces. It was found that less than 2% of the

adsorbed CO was oxidised to CO_2. In a similar study of CO adsorption on Rh on polycrystalline CeO_2, approximately 20% of the adsorbed CO was oxidised to CO_2 [39]. A study of CO adsorption and reaction on CeO_2/Rh(111) inverse model catalyst surfaces [48] showed that CO dissociation is not observed on this surface, even with the presence of bare Rh(111) sites. It was concluded that low coordinated Rh atoms such as those found on small metal particles are the active centres for CO dissociation.

Experiments involving CO adsorption on Rh deposited on reduced CeO_2(111) have shown that the degree of CO dissociation is directly dependent on the degree of oxidation of the CeO_x [29, 32]. In both studies the fraction of adsorbed CO which was dissociated increased as the CeO_2 was further reduced, suggesting that oxygen vacancies on the CeO_2 surface are involved in the dissociation reaction. Mullins *et al.* [29] also demonstrated that the degree of CO dissociation was independent of the amount of Rh or its morphology.

There have also been a large number of previous studies of CO adsorption on a variety of other metal/oxide surfaces. Extensive research of CO adsorption on Pd clusters grown on Al_2O_3 thin films has been carried out [5, 7, 21, 25, 60-66]. STM studies [25] show that palladium particles grown on Al_2O_3/NiAl(110) at room temperature are cubo-octahedral in shape with a flat (111) top, and (111) and (100) lateral facets. RAIRS experiments showed good agreement with these observations, as peaks assigned to CO-Pd(111) and (100) stretching frequencies were observed. Similar results were obtained from CO adsorbed on Pd/SiO_2/Mo(112) [21, 67, 68].

RAIRS studies of CO adsorption onto the Pd/Al_2O_3 surface also show that the size of the Pd clusters has a significant effect on the types and intensities of vibrational modes observed [21, 62-66]. The effects of elevated temperatures and high pressure CO exposure on the Pd/Al_2O_3 surface have also been studied [21, 61, 64, 65] to more closely mimic the operating conditions of a catalytic converter.

Thesis overview

The aim of the work described in this thesis is to determine how the interactions of CO and Pd with CeO_{2-x}(111) thin films affect the ceria oxidation state. This has been achieved using XPS, which has been used to identify surface species. Ce 3d XP spectra have also been used in order to calculate the ceria oxidation state. The effect of the substrate onto which the CeO_{2-x} thin films are grown has also been explored. CO is also used as a probe molecule in RAIRS studies of the $Pd/CeO_{2-x}/Pt(111)$ surface in order to determine the structure of the Pd nanoclusters grown on the CeO_{2-x} thin films.

In chapter 2 the theory behind the experimental methods used will be discussed, and in chapter 3 the set up of the experimental apparatus will be described. Chapter 4 reviews previous experiments on ceria thin films grown on Pt(111), and then goes on to describe in detail how the thin films were grown in this set of experiments. Methods for characterising CeO_{2-x} thin films, and calculating the CeO_{2-x} thin film thickness and oxidation state, are also described. Experiments have also been carried out to change the oxidation state of the CeO_{2-x} thin films. In chapter 5 RAIRS experiments of CO adsorbed on $Pd/CeO_{1.91}(111)/Pt(111)$ are described. CO adsorption and desorption experiments have been carried out on $Pd/CeO_{1.91}(111)/Pt(111)$ surfaces as a function of Pd coverage. The observed CO stretching frequencies have been used to deduce information about the morphology of the Pd clusters as a function of coverage. In chapter 6 XPS investigations of CO adsorbed on $Pd/CeO_{2-x}(111)/Pt(111)$ are described. The effect of Pd coverage and CO adsorption on the oxidation state of ceria thin films is discussed. Experiments have also been carried out using CeO_{2-x} thin films with different initial oxidation states. By studying how the oxidation state of the CeO_{2-x} is affected it is hoped that information on the catalytic activity of the system can be inferred. XPS experiments of CO adsorbed on $Pd/CeO_{2-x}(111)/Rh(111)$ have also been carried out, and are described in detail in chapter 7. By comparing experiments where Rh(111) has been used as the substrate to those where Pt(111) has been used, the effect of the substrate on the CeO_{2-x} thin films can be inferred. Finally, in chapter 8 the $CeO_{2-x}/Pt(111)$ and

CeO_{2-x}/Rh(111) surfaces will be compared and possibilities of substrate dependent chemical effects will be discussed.

References

1. Haruta M., Tsubota S., Kobayashi T., Kageyama H., Genet M. J., and Delmon B., *Low-Temperature Oxidation of CO over Gold Supported on TiO_2, α-Fe_2O_3, and Co_3O_4.* J. Catal., 1993. **144**(1): p. 175.
2. Hardacre, C., Ormerod, R.M., and Lambert, R.M., *Platinum promoted catalysis by ceria: a study of carbon monoxide oxidation over $Pt(111)/CeO_2$.* J. Phys. Chem., 1994. **98**: p. 10901.
3. Campbell, C.T., *Ultrathin metal films and particles on oxide surfaces: Structural, electronic and chemisorptive properties.* Surf. Sci. Rep., 1997. **27**(1-3): p. 1.
4. Baumer, M. and Freund, H.J., *Metal deposits on well-ordered oxide films.* Prog. Surf. Sci., 1999. **61**(7-8): p. 127.
5. Rainer, D.R. and Goodman, D.W., *Metal clusters on ultrathin oxide films: model catalysts for surface science studies.* J. Mol. Catal. A, 1998. **131**(1-3): p. 259.
6. Henry, C.R., *Surface studies of supported model catalysts.* Surf. Sci. Rep., 1998. **31**(7-8): p. 235.
7. Rainer, D.R., Xu, C., and Goodman, D.W., *Characterization and catalysis studies of small metal particles on planar model oxide supports.* J. Mol. Catal. A, 1997. **119**(1-3): p. 307.
8. Kaspar, J., Fornasiero, P., and Graziani, M., *Use of CeO_2-based oxides in the three-way catalysis.* Catalysis Today, 1999. **50**(2): p. 285.
9. Trovarelli, A., *Catalysis by ceria and related materials.* Catalytic Science Series, ed. G. Hutchings. Vol. 2. 2000, London: Imperial College Press.
10. Diwell, A.F., Rajaram, R.R., Shaw, H.A., and Truex, T.J., *The role of Ceria in three-way catalysts*, in *Catalysis and Automotive Pollution Control II*, A. Crucq, Editor. 1991, Elsevier Science Publishers: Amsterdam. p. 139.
11. Thomas, J.M. and Thomas, W.J., *Automobile exhaust catalysts*, in *Principles and practice of heterogeneous catalysis.* 1997, VCH.
12. Shelef, M., Graham, G., and McCabe, R., *Ceria and other oxygen storage components in automotive catalysts*, in *Catalysis by Ceria and related*

materials, A. Trovarelli, Editor. 2002, Imperial College Press: London. p. 343.

13. Bunluesin, T., Putna, E.S., and Gorte, R.J., *A comparison of CO oxidation on ceria-supported Pt, Pd, and Rh.* Catal. Lett., 1996. **41**: p. 1.
14. Zafiris, G.S. and Gorte, R.J., *Evidence for a second CO oxidation mechanism on Rh/ceria.* J. Catal., 1993. **143**(1): p. 86.
15. Trovarelli, A., de Leitenburg, C., Boaro, M., and Dolcetti, G., *The utilization of ceria in industrial catalysis.* Catalysis Today, 1999. **50**(2): p. 353.
16. Evans, J., Hayden, B.E., and Lu, G., *The adsorption of carbon monoxide on TiO_2(110) supported palladium.* Surf. Sci., 1996. **360**(1-3): p. 61.
17. Diebold, U., Pan, J.-M., and Madey, T.E., *Ultrathin metal film growth on TiO_2(110): an overview.* Surface Science: Proceedings of the 14th European Conference on Surface Science, 1995. **331-333**(Part 2): p. 845.
18. Ealet, B. and Gillet, E., *Palladium alumina interface: influence of the oxide stoichiometry studied by EELS and XPS.* Surf. Sci., 1993. **281**(1-2): p. 91.
19. Sandell, A., Libuda, J., Bruhwiler, P.A., Andersson, S., Maxwell, A.J., Baumer, M., Martensson, N., and Freund, H.J., *Interaction of CO with Pd clusters supported on a thin alumina film.* J. Vac. Sci. Technol. A-Vac. Surf. Films, 1996. **14**(3): p. 1546.
20. Baumer, M., Libuda, J., Sandell, A., Freund, H.J., Graw, G., Bertrams, T., and Neddermeyer, H., *The growth and properties of Pd and Pt on Al_2O_3/NiAl(110).* Berichte Der Bunsen-Gesellschaft-Physical Chemistry Chemical Physics, 1995. **99**(11): p. 1381.
21. Ozensoy, E. and Goodman, D.W., *Vibrational spectroscopic studies on CO adsorption, NO adsorption CO plus NO reaction on Pd model catalysts.* Phys. Chem. Chem. Phys., 2004. **6**(14): p. 3765.
22. Zilm, K.W., Bonneviot, L., Haller, G.L., Han, O.H., and Kermarec, M., *C-13 NMR-spectra of CO-13 adsorbed on silica-supported palladium particles - particle-size dependence of the surface-diffusion rate and the C-13 Knight-shift.* J. Phys. Chem., 1990. **94**(23): p. 8495.

23. Kasper, N., Stierle, A., Nolte, P., Jin-Phillipp, Y., Wagner, T., de Oteyza, D.G., and Dosch, H., *In situ oxidation study of MgO(1 0 0) supported Pd nanoparticles*. Surf. Sci., 2006. **600**(14): p. 2860.

24. Leighton, C.A., Swift, A.J., and Vickerman, J.C., *Further characterisation of Pd deposited on an extensively oxidised Zn(001) support*. Surf. Sci., 1991. **253**(1-3): p. 220.

25. Hansen, K.H., Worren, T., Stempel, S., Laegsgaard, E., Baumer, M., Freund, H.J., Besenbacher, F., and Stensgaard, I., *Palladium nanocrystals on Al_2O_3: Structure and adhesion energy*. Phys. Rev. Lett., 1999. **83**(20): p. 4120.

26. Schierbaum, K.D., Fischer, S., Torquemada, M.C., de Segovia, J.L., Roman, E., and Martin-Gago, J.A., *The interaction of Pt with TiO_2(110) surfaces: a comparative XPS, UPS, ISS, and ESD study*. Surf. Sci., 1996. **345**(3): p. 261.

27. Stubenrauch, J. and Vohs, J.M., *Interaction of CO with Rh supported on stoichiometric and reduced CeO_2(111) and CeO_2(100) surfaces*. J. Catal., 1996. **159**: p. 50.

28. Bunluesin, T., Cordatos, H., and Gorte, R.J., *A study of CO oxidation kinetics on Rh/Ceria*. J. Catal., 1995. **157**: p. 222.

29. Mullins, D.R. and Overbury, S.H., *CO dissociation on Rh deposited on reduced cerium oxide thin films*. J. Catal., 1999. **188**: p. 340.

30. Mullins, D.R., Kundakovic, L., and Overbury, S.H., *The interaction between NO and CO on Rh-loaded CeO_x(111)*. J. Catal., 2000. **195**: p. 169.

31. Cordatos, H., Bunluesin, T., Stubenrauch, J., Vohs, J.M., and Gorte, R.J., *Effect of ceria structure on oxygen migration for Rh/ceria catalysts*. J. Phys. Chem., 1996. **100**(2): p. 785.

32. Stubenrauch, J. and Vohs, J.M., *Support effects in the dissociation of CO on Rh/CeO_2(111)*. Catal. Lett., 1997. **47**(1): p. 21.

33. Putna, E.S., Gorte, R.J., Vohs, J.M., and Graham, G.W., *Evidence for enhanced dissociation of CO on Rh/ceria*. J. Catal., 1998. **178**(2): p. 598.

34. Mullins, D.R., *Reactions on model emission control catalysts studied by soft X-ray photoemission.* J. Electron Spectrosc. Relat. Phenom., 2001. **114**: p. 333.

35. Mullins, D.R. and Overbury, S.H., *Coverage dependent dissociation of NO on Rh supported on cerium dioxide thin films.* Surf. Sci. Lett., 2002. **511**: p. L293.

36. Overbury, S.H., Mullins, D.R., and Kundakovic, L., *Enhancement of dissociation by metal-support interaction: reaction of NO on Rh supported by ceria films of controlled oxidation state.* Surf. Sci., 2001. **470**: p. 243.

37. Overbury, S.H., Huntley, D.R., Mullins, D.R., Ailey, K.S., and Radulovic, P.V., *Surface studies of model supported catalysts: NO adsorption on Rh/CeO_2(001).* J. Vac. Sci. Technol. A, 1997. **15**(3): p. 1647.

38. Xu, J. and Overbury, S.H., *H_2 reduction of CeO_2(111) surfaces via boundary Rh-O mediation.* J. Catal., 2004. **222**(1): p. 167.

39. Zafiris, G.S. and Gorte, R.J., *Evidence for Low-Temperature Oxygen Migration from Ceria to Rh.* J. Catal., 1993. **139**(2): p. 561.

40. Pfau, A., Schierbaum, K.D., and Gopel, W., *The electronic structure of CeO_2 thin films: the influence of Rh surface dopants.* Surf. Sci., 1995. **331-333**: p. 1479.

41. Overbury, S.H., Mullins, D.R., Huntley, D.R., and Kundakovic, L., *Chemisorption and reaction of NO and N_2O on oxidised and reduced ceria surfaces studied by soft x-ray photoemission spectroscopy and desorption spectroscopy.* J. Catal., 1999. **186**: p. 296.

42. Mullins, D.R., Overbury, S.H., and Huntley, D.R., *Electron spectroscopy of single crystal and polycrystalline cerium oxide surfaces.* Surf. Sci., 1998. **409**: p. 307.

43. Alexandrou, M. and Nix, R.M., *The growth, structure and stability of ceria overlayers on Pd(111).* Surf. Sci., 1994. **321**(1-2): p. 47.

44. Mullins, D.R., Radulovic, P.V., and Overbury, S.H., *Ordered cerium oxide thin films grown on Ru(0001) and Ni(111).* Surf. Sci., 1999. **429**(1-3): p. 186.

45. Mullins, D.R., Overbury, S.H., and Kundakovic, L., *Reactions between co-adsorbates on Rh loaded CeO_x thin films.* Abstr. Pap. Am. Chem. Soc., 2001. **221**: p. 435.

46. Lu, J.-L., Gao, H.-J., Shaikhutdinov, S., and Freund, H.-J., *Morphology and defect structure of the CeO_2(111) films grown on Ru(0001) as studied by scanning tunneling microscopy.* Surf. Sci. **In Press**.

47. Castellarin-Cudia, C., Surnev, S., Schneider, G., Podlucky, R., Ramsey, M.G., and Netzer, F.P., *Strain-induced formation of arrays of catalytically active sites at the metal-oxide interface.* Surf. Sci. Lett., 2004. **554**: p. L120.

48. Eck, S., Castellarin-Cudia, C., Surnev, S., Prince, K.C., Ramsey, M.G., and Netzer, F.P., *Adsorption and reaction of CO on a ceria-Rh(111) "inverse model catalyst" surface.* Surf. Sci., 2003. **536**(1-3): p. 166.

49. Eck, S., Castellarin-Cudia, C., Surnev, S., Ramsey, M.G., and Netzer, F.P., *Growth and thermal properties of ultrathin cerium oxide layers on Rh(111).* Surf. Sci., 2002. **520**(3): p. 173.

50. Belton, D. and Schmieg, S., *Low temperature oxidation and reduction of ceria particles on Rh(111).* J. Vac. Sci. Technol. A, 1993. **11**: p. 2330.

51. Wilson, E.L., Brown, W.A., and Thornton, G., *RAIRS studies of CO adsorption on Pd/CeO_{2-x}(111)/Pt(111).* Surf. Sci., 2006. **600**(12): p. 2555.

52. Schierbaum, K.-D., *Ordered ultra-thin cerium dioxide overlayers on Pt(111) single crystal surfaces studied by LEED and XPS.* Surf. Sci., 1998. **399**: p. 29.

53. Hardacre, C., Roe, G.M., and Lambert, R.M., *Structure, composition and thermal properties of cerium oxide films on Pt(111).* Surf. Sci., 1995. **326**: p. 1.

54. Berner, U. and Schierbaum, K.-D., *Cerium oxide layers on Pt(111): a scanning microscopy study.* Thin Solid Films, 2001. **400**(1-2): p. 46.

55. Berner, U. and Schierbaum, K.-D., *Cerium oxides and cerium-platinum surface alloys on Pt(111) single-crystal surfaces studied by scanning tunneling microscopy.* Phys. Rev. B, 2002. **65**: p. 235404.

56. Berner, U., Schierbaum, K.-D., Jones, G., Wincott, P., Haq, S., and Thornton, G., *Ultrathin ordered CeO_2 overlayers on Pt(111): interaction with NO_2, NO, H_2O and CO*. Surf. Sci., 2000. **467**: p. 201.

57. Pfau, A. and Schierbaum, K.-D., *The electronic structure of stoichiometric and reduced CeO_2 surfaces: an XPS, UPS and HREELS study*. Surf. Sci., 1994. **321**: p. 71.

58. Overbury, S.H., Huntley, D.R., Mullins, D.R., and Glavee, G.N., *XANES studies of the reduction behavior of $(Ce_{1-y}Zr_y)O_2$ and $Rh/(Ce_{1-y}Zr_y)O_2$*. Catal. Lett., 1998. **51**(3 - 4): p. 3.

59. Zafiris, G.S. and Gorte, R.J., *A study of CO, NO, and H_2 adsorption on model Pt/CeO_2 catalysts*. Surf. Sci., 1992. **276**(1-3): p. 86.

60. Rainer, D.R., Vesecky, S.M., Koranne, M., Oh, W.S., and Goodman, D.W., *The CO+NO reaction over Pd: A combined study using single-crystal, planar-model-supported, and high-surface-area Pd/Al_2O_3 catalysts*. J. Catal., 1997. **167**(1): p. 234.

61. Unterhalt, H., Galletto, P., Morkel, M., Rupprechter, G., and Freund, H.J., *Sum frequency generation study of CO adsorption on palladium model catalysts*. Physica Status Solidi A-Applied Research, 2001. **188**(4): p. 1495.

62. Wolter, K., Seiferth, O., Libuda, J., Kuhlenbeck, H., Baumer, M., and Freund, H.J., *Infrared study of CO adsorption on alumina supported palladium particles*. Surf. Sci., 1998. **404**(1-3): p. 428.

63. Wolter, K., Seiferth, O., Kuhlenbeck, H., Baumer, M., and Freund, H.J., *Infrared spectroscopic investigation of CO adsorbed on Pd aggregates deposited on an alumina model support*. Surf. Sci., 1998. **399**(2-3): p. 190.

64. Unterhalt, H., Rupprechter, G., and Freund, H.J., *Vibrational sum frequency spectroscopy on Pd(111) and supported Pd nanoparticles: CO adsorption from ultrahigh vacuum to atmospheric pressure*. J. Phys. Chem. B, 2002. **106**(2): p. 356.

65. Rainer, D.R., Wu, M.C., Mahon, D.I., and Goodman, D.W., *Adsorption of CO on $Pd/Al_2O_3/Ta(110)$ model catalysts*. J. Vac. Sci. Technol. A-Vac. Surf. Films, 1996. **14**(3): p. 1184.

66. Lear, T., Marshall, R., Lopez-Sanchez, J.A., Jackson, S.D., Klapotke, T.M., Baumer, M., Rupprechter, G., Freund, H.J., and Lennon, D., *The application of infrared spectroscopy to probe the surface morphology of alumina-supported palladium catalysts*. J. Chem. Phys., 2005. **123**(17): p. 174706.

67. Ozensoy, E., Min, B.K., Santra, A.K., and Goodman, D.W., *CO dissociation at elevated pressures on supported Pd nanoclusters*. J. Phys. Chem. B, 2004. **108**(14): p. 4351.

68. Giorgi, J.B., Schroeder, T., Baumer, M., and Freund, H.J., *Study of CO adsorption on crystalline-silica-supported palladium particles*. Surf. Sci., 2002. **498**(1-2): p. L71.

Chapter 2 : Theoretical considerations

Introduction

This chapter describes the theoretical basis behind the two main experimental techniques used in this study, reflection absorption infrared spectroscopy (RAIRS) and X-ray photoelectron spectroscopy (XPS). RAIRS involves the interaction of infrared (IR) light with adsorbed molecules, and gives information on the vibrational frequencies of these adsorbates. XPS involves the interaction of photons with a sample surface resulting in the emission and detection of photoelectrons. The kinetic energy of these photoelectrons is used to identify all species present in the top 10 nm of the sample.

RAIRS

Historical development

The first IR spectroscopy experiments to look at vibrational frequencies of adsorbed species on a surface were carried out in 1938 [1]. This involved the use of transmission IR spectroscopy, where spectra were compared before and after passing IR light through a sample, resulting in absorption bands with frequencies specific to sample components [2]. This technique was very limited when studying surface interactions, as samples used had to be very thin and transparent to IR light. Also, in the resulting absorption spectrum, bands due to surface species only consisted of a very small proportion of the total absorption, so were difficult to identify. Due to the difficulties of using transmission experiments to study surface species, reflection techniques were later developed. The very first reflection experiments, which involved the use of multiple reflections from the surface, were carried out in 1959 [3, 4]. It was initially thought that multiple reflections would be necessary to gain adequate sensitivity in order to detect surface interactions, however the theoretical studies of Greenler later proved that single reflection was sufficient [5, 6]. RAIRS experiments have since been used to study a variety of single crystal metal surfaces, and hence a number of reviews have been written on the subject [7-10].

General principles

In RAIRS experiments IR light is focused onto the sample surface, and is reflected through a thin layer of adsorbates. When the reflected light is detected, losses in the intensity of the light occur at frequencies corresponding to vibrational modes of the adsorbed species. The absorption of IR light by adsorbates is dominated by the dielectric behaviour of the metal substrate [8].

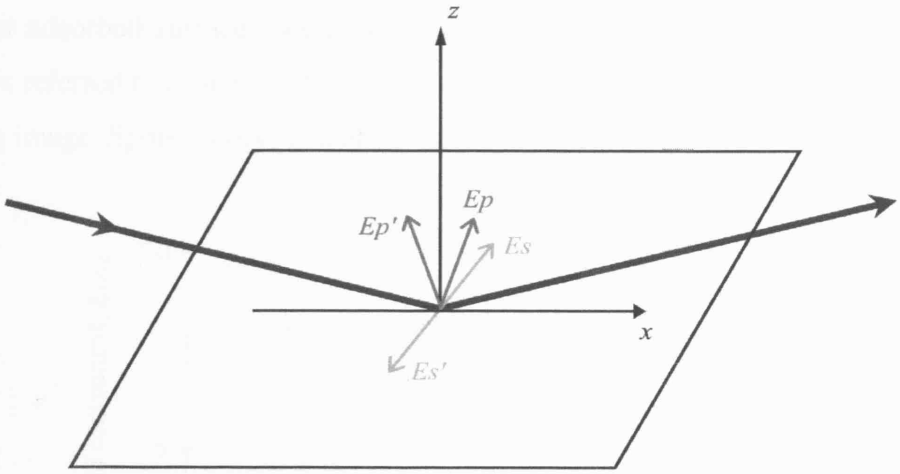

Figure 2.1 Diagram showing the electric fields associated with incident and reflected IR radiation at a clean metal surface. E_p and E_s are the p-polarised and s-polarised components of the incident radiation respectively. E_p' and E_s' are the reflected components of the IR beam. The plane of incidence is the xz plane.

Figure 2.1 shows the electric field associated with incident and reflected light at a metal surface, indicating the perpendicularly polarised (p) and parallel polarised (s) components of the radiation. $\mathbf{E}_p$ and $\mathbf{E}_s$ are the p-polarised and s-polarised components of the incident radiation respectively, and $\mathbf{E}_p'$ and $\mathbf{E}_s'$ are the reflected components of the IR beam. At all angles of incidence, the s-polarised component reverses in phase by 180° upon reflection, and the reflection coefficient is near unity. Therefore, the vector sum of incident and reflected components is close to zero, meaning that the s-polarised component of the IR light will not interact significantly with the surface dipoles. However, the phase change of the p-polarised component is highly dependent on the angle of

incidence. Figure 2.2 shows how the amplitude of the resulting electric field vectors is dependent on the angle of incidence, relative to the amplitude of the incident beam ($\mathbf{E}_0$). It can be seen that at grazing incidence the tangential vector ($\mathbf{E}_{p\perp}$) is almost doubled, whereas the parallel vector of the p-polarised light ($\mathbf{E}_{p||}$) remains insignificant at all angles. The p-component of IR radiation will therefore interact strongly with perpendicularly orientated vibrational modes of surface adsorbates, however IR radiation is not sensitive to adsorbates with vibrational modes parallel to the surface. This means that RAIRS will only detect adsorbed surface species with components normal to the surface plane, and is referred to as the "surface selection rule". This rule can also be explained using image dipole theory, as demonstrated in Figure 2.3.

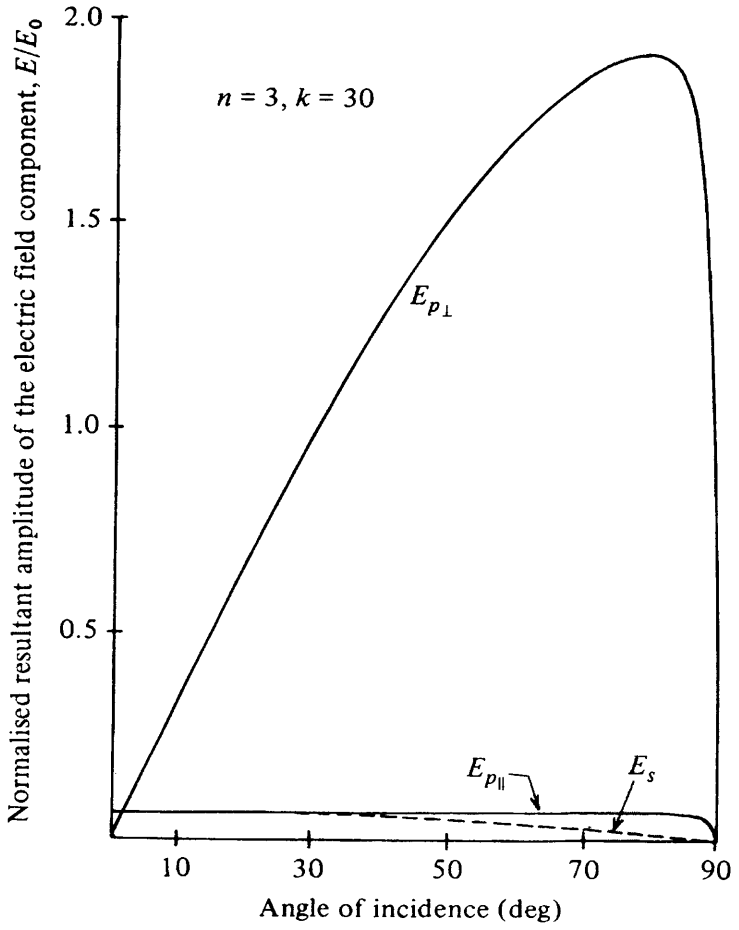

Figure 2.2 A graph showing the angular dependence of the resultant amplitude of the electric field components of an incident IR beam at a clean metal surface. $E_{p||}$ and $E_{p\perp}$ are the parallel and tangential components of the p-polarised incident radiation respectively [2].

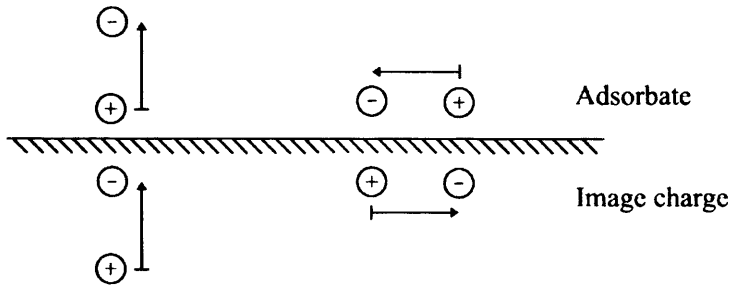

Figure 2.3 A diagrammatic representation of the image dipoles induced within a metal surface by parallel and perpendicularly orientated dipoles adsorbed on the surface.

Figure 2.3 shows the formation of image dipoles in a metal substrate for parallel and perpendicularly orientated dipoles adsorbed on the surface. The long range electromagnetic field cannot distinguish between the dipole and its image, and hence interacts with the vector sum of the dipole fields [11]. For a dipole that is perpendicularly orientated with respect to the sample surface, the sum of the dipole and the image results in a reinforcement of the dipole moment. In the case of a dipole orientated parallel to the surface the vector sum of the two components is near zero. Hence, surface adsorbates with dipole moments parallel to the surface will not be detected by RAIRS, however dipoles with a component perpendicular to the surface will be detected.

Another important consideration when conducting RAIRS experiments is that the intensity of absorption by surface adsorbates is highly dependent on the angle of incidence of the IR beam [2]. The absorption intensity increases as the angle of incidence is increased (Figure 2.4), due to a larger area of the surface being irradiated and hence a larger number of adsorbed species being sampled. The area of irradiation increases as sec θ, where θ is the angle of incidence. Therefore, the total absorption intensity is proportional to E^2 sec θ, where E is the amplitude of the electric field [2]. As shown in Figure 2.4 the optimum angle of the incident IR beam for maximum absorption intensity is 88°.

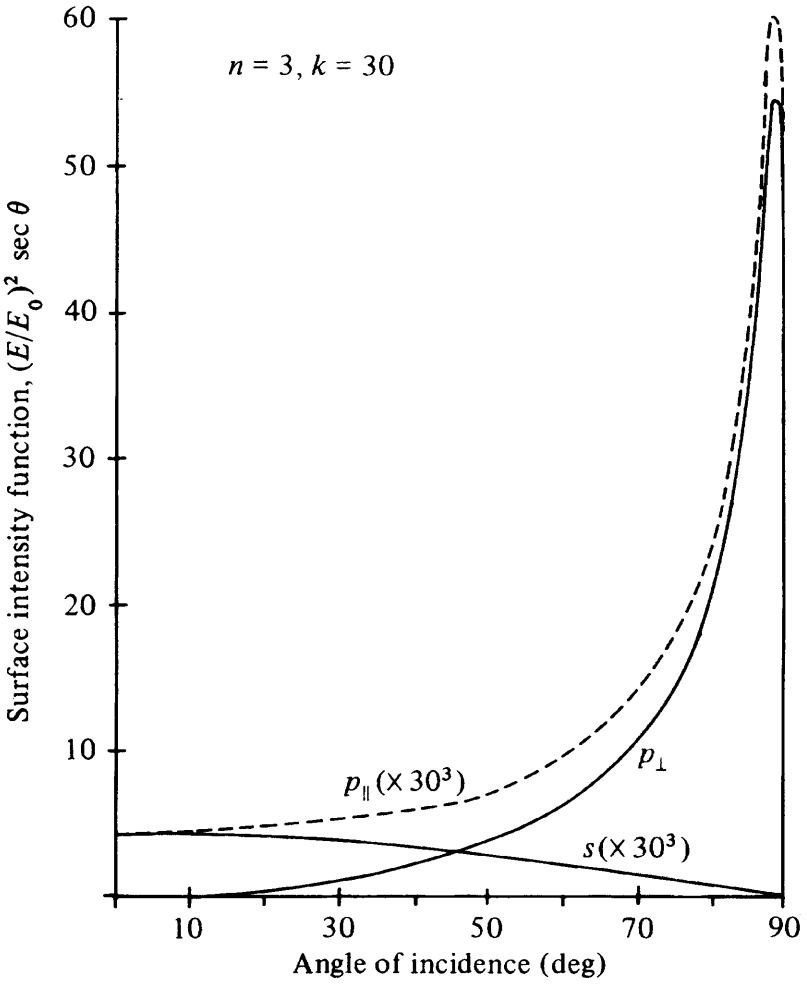

Figure 2.4 A graph showing the angular dependence of the surface intensity function for the electric field components of incident IR radiation at a clean metal surface [2].

In summary, the following points must be considered when conducting RAIRS experiments on highly reflective metal surfaces:

1. Only interactions between the adsorbate and perpendicular components of the IR beam will be observed.
2. Only vibrations of absorbates with a component of the dipole perpendicular to the surface will be observed.
3. The maximum absorption intensity will be observed for IR light at grazing incidence to the sample surface.
4. For higher values of sample surface reflectivity, larger absorbance will be observed.

RAIRS on oxide thin films

The use of RAIRS on insulating surfaces, such as bulk CeO_2, is limited due to poor reflectivity and poor IR absorption by the surface, hence resulting in a two- to three-fold drop in sensitivity compared to a highly reflective metal surface [12]. Insulating surfaces can be more effectively studied when grown as thin films on top of a metallic substrate, using a method known as the buried metal layer approach. If the film thickness is considerably smaller than the wavelength of the IR radiation being used, the reflectivity is that of the metallic substrate, increasing the sensitivity. Despite the fact that the IR light is reflecting from the metal substrate the chemistry being observed is that of adsorbates on the oxide thin film. A number of groups have successfully employed the use of the buried metal layer approach to study oxide thin films [12-16]. There are also a number of theoretical studies on the subject [17, 18].

XPS

Historical development

The first investigations into the use of X-rays came about due to the discovery of the photoelectric effect by Hertz in 1887 [19]. In 1905 Einstein was able to theoretically justify the original observations made by Hertz. Einstein correctly proposed that quanta of light, in the form of energy packets called photons, were able to directly transfer their energy to electrons within an atom resulting in the emission of electrons without energy loss [20].

In the early 1900's rapid developments were made with the use of radioactive X-ray sources. However in 1957 electron spectroscopy using X-ray excitation was discovered by Kai Siegbahn's group, and successfully employed to observe the first well resolved X-ray photoelectron spectra [21, 22]. The group subsequently observed the chemical shift of core level binding energies [23, 24], and during the period 1955-1970 went on to develop the whole field of electron spectroscopy [25].

General principles

X-ray photoelectron spectroscopy (XPS) is, in principle, a relatively simple technique which can identify all the elements present in the top 10 nm of a sample utilising the photoelectric effect [26]. An X-ray gun is used to emit photons of a known energy, hν, which are aimed at the sample surface. The surface atoms emit photoelectrons after direct energy transfer from the photon to the core level electrons. This process is described by the following equation:

$$E_K = h\nu - E_B - \phi \qquad \textbf{Equation 2.1}$$

where E_K is the measured electron kinetic energy, E_B is the binding energy of the electron within the atom, and ϕ is the work function. Hence, the energy distribution of the photoemitted electrons is directly related to the energy distribution of the electronic states in the surface of the solid. The collection of the kinetic energies of the ejected photoelectrons can therefore provide a spectrum of binding energies which is both elementally and chemically specific, providing a fingerprint of the material analysed. Figure 2.5 shows an XPS spectrum of a clean Rh(111) surface, taken using Mg Kα radiation from a standard laboratory X-ray gun.

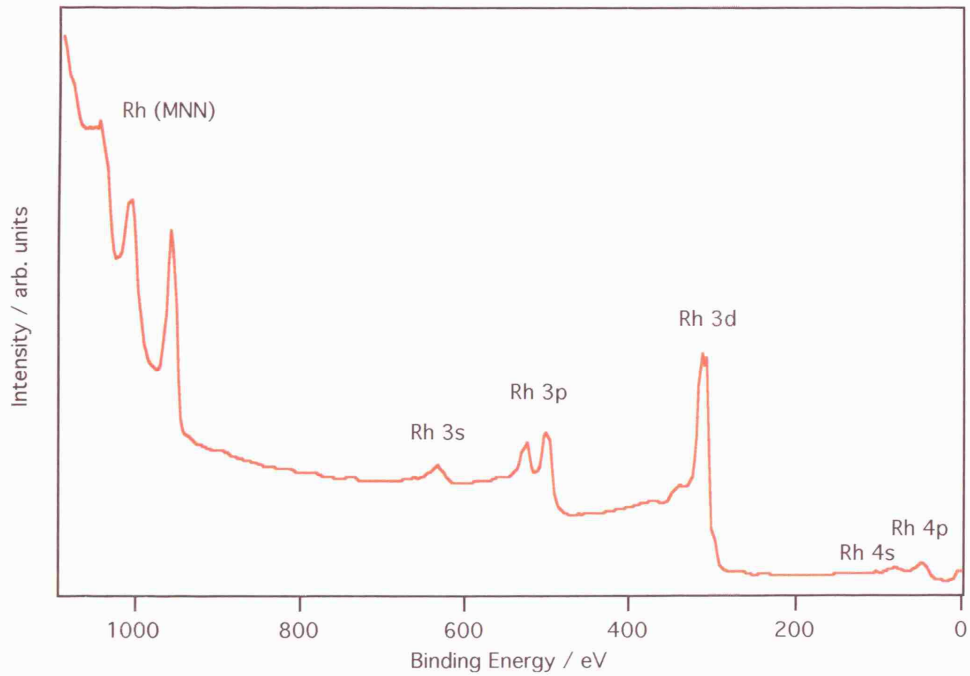

Figure 2.5 XPS overview scan of a Rh(111) crystal, taken using Mg Kα radiation from a standard laboratory X-ray gun.

Main spectral features

The main spectral features that can be observed on a typical wide scan XP spectrum, such as the one shown in Figure 2.5, can be categorised as core level peaks, valence band peaks, or Auger peaks.

Core level peaks show the electronic structure of the sample used. Mg Kα radiation, as used to take the spectrum in Figure 2.5, only has enough energy to probe the core levels of the Rh atoms to the 4p level. The ejection of photoelectrons from s-orbitals results in single peaks, whereas non-s-levels are observed as doublets due to spin-orbit coupling. Relative peak intensities are mainly dependent on the atomic cross section (α), and the line width (Γ) is directly related to the uncertainty in the lifetime of the core hole after photoemission, as given by Heisenberg's uncertainty principle:

$$\Gamma = \frac{h}{\tau} \qquad \textbf{Equation 2.2}$$

where h is Planck's constant, and τ is the core hole lifetime.

Valence band peaks are observed at low binding energies, between 0-20 eV. These features are due to photoelectron emission from valence levels, as opposed to core level electrons. The peaks in this region are very closely packed, resulting in a band-like structure.

Photoemitted electrons are not the only type of electrons observed in XP spectra, Auger electrons can also be detected. When an atom is ionised by a photon this results in the production of a core hole. The ion can lose potential energy by filling the core hole with an electron from a higher energy level. The resultant energy produced by this process can be released by ejecting a photon or another electron. The process releasing an electron is known as Auger decay, during which an Auger electron is emitted.

Initial and final state effects

Koopmans' theorem

It has previously been stated that the photoelectron spectrum should simply show the density of occupied electronic states on the sample surface plus the photon energy. However, this assumes that the binding energy of a given electronic state is the same before the interaction with the photon as it is after, and that all other electrons in the system remain in the same state as before the photoionisation event occurred. Hence, the binding energy (E_B) of an emitted photoelectron can be expressed as the difference between the (n-1)-electron final state energy and the n-electron initial state energy, as shown in Koopmans' theorem:

$$E_B = E_f(n-1) - E_i(n) \qquad \textbf{Equation 2.3}$$

where $E_f(n-1)$ is the final state energy, and $E_i(n)$ is the initial state energy. The assumptions made thus far imply that the observed binding energy is equal to the negative orbital energy ($-\varepsilon_K$) of the ejected photoelectron, which is an approximation of Koopmans' theorem. However, this assumption is not generally valid because, after the creation of a core hole, the remaining electrons respond by rearranging to minimise the energy of the ionised atom, and hence maximise the energy available to the outgoing photoelectron. The energy reduction caused by this rearrangement of electrons is the relaxation energy, which contributes to the binding energy observed. Initial state effects can also contribute to the binding energy.

Initial state effects

The initial state of an atom is the ground state before photoemission occurs. The energy of the atom's initial state, before any interactions, can be changed by formation of chemical bonds with other atoms. For example, as the oxidation state of an atom is increased the binding energy of the ejected photoelectrons will also increase. The consequent change in binding energy is referred to as the chemical shift.

Spin-orbit splitting is another initial state effect, which causes non-s levels to appear as doublet peaks. Coupling between the magnetic fields of spin and angular momentum (j-j coupling) occurs in all electrons. The total orbital angular momentum (j) is given by:

$$j=l+s \qquad \textbf{Equation 2.4}$$

where l is the orbital angular momentum and s is the spin angular momentum. For $l > 0$, two possible states arise, giving two XPS peaks for non-s level electrons.

Final state effects

Final state effects are changes to the binding energy caused by the electron rearrangements resulting from photoemission.

Multiplet splitting is due to the interactions between unpaired electrons in the valence level and the electrons in core levels. An example of multiplet splitting observed in this study is seen in the core level Ce 3d peaks in the XP spectra of CeO_{2-x}. Photoemission causes the creation of core holes in the Ce 3d level, which results in the rearrangement of valence electrons, reducing the energy of the 4f level, due to reduced electron shielding. This means that hybridization of the O 2p levels with the Ce 4f levels will occur more readily [27]. This process results in the observation of a number of peaks at different kinetic energies. XP spectra of the Ce $3d_{5/2}$ level consist of five gaussian contributions, three of which are due to the presence of Ce^{4+} ions and are observed in CeO_2. The remaining two peaks are associated with Ce^{3+} ions, and are observed in XPS of Ce_2O_3. Accounting for spin-orbit coupling, there are 10 Ce 3d peaks in total, which can all be observed in the CeO_{2-x} XP spectrum.

Shake-up satellites are caused by the excitation of a valence electron to a higher unoccupied energy state during photoemission. If the photoelectron provides enough energy on emission to promote the valence electron to a free electron state, an ion with vacancies in the core and valence levels results, and shake-off peaks are observed.

Analysis Depth

The analysis depth achieved in XPS is limited by the inelastic mean free path of the emitted photoelectrons, which is relatively short compared to that of the photons. Only photoelectrons which escape from the surface with minimal energy loss will appear as photoemission peaks in an XP spectrum. Any electrons which have significant energy loss will contribute to the background signal. Figure 2.6 shows how the escape depth of electrons varies with respect to their kinetic energy. In XPS experiments typical photoelectron kinetic energies are in the range of 15-1000 eV, which relates to an escape depth of between 10 and 20 Å. Therefore XPS is highly surface sensitive, and hence can be used effectively to detect surface adsorbates.

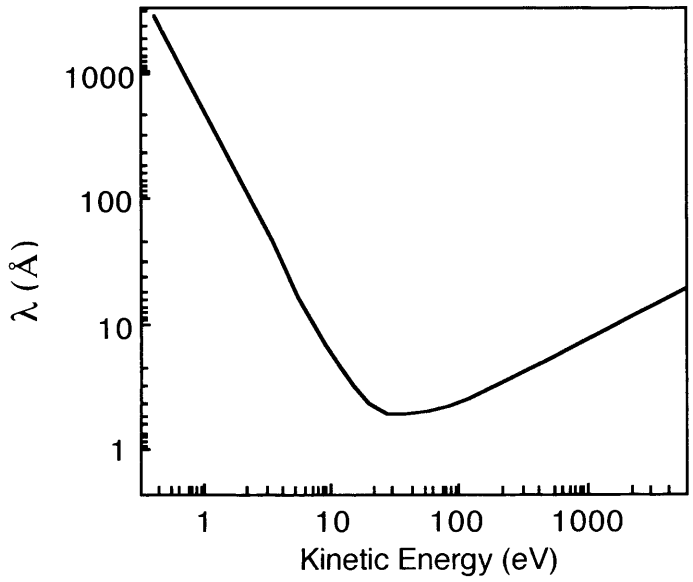

Figure 2.6 Graph showing the escape depth (λ) of electrons against kinetic energy.

References

1. Buswell, A.M., Krebs, K., and Rodebush, W.H., *Infrared Studies. III. Absorption Bands of Hydrogels between 2.5 and 3.* Journal of the American Chemical Society, 1937. **59**(12): p. 2603.
2. Riviere, J.C., *Surface Analytical Techniques.* Monographs on the Physics and Chemistry of Materials. 1990, Oxford: Clarendon Press.
3. Francis, S.A. and Ellison, A.H., *Infrared spectra of monolayers on metal mirrors.* Journal of the Optical Society of America, 1959. **49**(2): p. 131.
4. Pickering, H.L. and Eckstrom, H.C., *Heterogeneous reaction studies by infrared absorption.* J. Phys. Chem., 1959. **63**(4): p. 512.
5. Greenler, R.G., *Reflection method for obtaining the infrared spectrum of a thin layer on a metal surface.* J. Chem. Phys., 1969. **50**(5): p. 1963.
6. Greenler, R.G., *Infrared study of adsorbed molecules on metal surfaces by reflection techniques.* J. Chem. Phys., 1966. **44**(1): p. 310.
7. Chabal, Y.J., *Surface Infrared-Spectroscopy.* Surf. Sci. Rep., 1988. **8**(5-7): p. 211.
8. Hoffmann, F.M., *Infrared reflection-absorption spectroscopy of adsorbed molecules.* Surf. Sci. Rep., 1983. **3**(2/3): p. 107.
9. Hirschmugl, C.J., *Frontiers in infrared spectroscopy at surfaces and interfaces.* Surf. Sci., 2002. **500**(1-3): p. 577.
10. Horn, A., *Infrared spectroscopic techniques for the study of thin interfacial films*, in *Spectroscopy for surface science*, R.J.H. Clark and R.E. Hester, Editors. 1998, John Wiley and Sons.
11. Yates, J.T. and Madey, T.E., *Vibrational spectroscopy of molecules on surfaces.* Methods of surface characterization. Vol. 1. 1987, New York: Plenum Press.
12. Pilling, M.J., Gardner, P., Pemble, M.E., and Surman, M., *A far-infrared RAIRS investigation of $SnCl_4$ on a silica surface using the buried metal layer approach.* Surf. Sci., 1998. **418**(1): p. L1.
13. McKelvy, M.L., Britt, T.R., Davis, B.L., Gillie, J.K., Graves, F.B., and Lentz, L.A., *Infrared spectroscopy.* Analytical Chemistry, 1998. **70**(12): p. 119R.

14. Ahmad, I., Dines, T.J., Rochester, C.H., and Anderson, J.A., *IR study of nitrotoluene adsorption on oxide surfaces*. J. Chem. Soc. Faraday Trans., 1996. **92**(17): p. 3225.
15. Purnell, S.K., Xu, X., Goodman, D.W., and Gates, B.C., *Adsorption and reaction of $Re_2(CO)_{10}$ on ultrathin MgO films grown on a Mo(110) surface: characterization by infrared reflection-absorption spectroscopy and temperature-programmed desorption*. J. Phys. Chem., 1994. **98**(15): p. 4076.
16. Xu, X.P., Vesecky, S.M., and Goodman, D.W., *Infrared reflection-absorption spectroscopy and STM studies of model silica-supported copper-catalysts*. Science, 1992. **258**(5083): p. 788.
17. Bermudez, V.M., *Infrared optical properties of dielectric/metal layer structures of relevance to reflection absorption spectroscopy*. Journal of Vacuum Science & Technology A: Vacuum, Surfaces, and Films, 1992. **10**(1): p. 152.
18. Gardner, P., LeVent, S., and Pilling, M., *A theoretical investigation of the far-infrared RAIRS experiment applied to a buried metal layer substrate*. Surf. Sci., 2004. **559**(2-3): p. 186.
19. Hertz, Annalen der Physik, 1887. **31**: p. 983.
20. Einstein, A., Annalen der Physik, 1905. **17**: p. 132.
21. Nordling, C., Sokolowski, E., and Siegbahn, K., *Precision method for obtaining absolute values of atomic binding energies*. Physical Review, 1957. **105**(5): p. 1676.
22. Sokolowski, E., Nordling, C., and Siegbahn, K., *Magnetic analysis of x-ray produced photo and Auger electrons*. Arkiv for Fysik, 1957. **12**(4): p. 301.
23. Sokolowski, E., Nordling, C., and Siegbahn, K., *Chemical shift effect in inner electronic levels of Cu due to oxidation*. Physical Review, 1958. **110**(3): p. 776.
24. Sokolowski, E. and Nordling, C., *Experimental studies of the KLL Auger spectra of Cu and Ge*. Arkiv for Fysik, 1959. **14**(6): p. 557.

25. Siegbahn, K., *Electron Spectroscopy for Chemical Analysis (ESCA).* Philosophical Transactions of the Royal Society of London Series a-Mathematical and Physical Sciences, 1970. **268**(1184): p. 33.

26. Vickerman, J.C., *Surface Analysis - The principal techniques.* 1997: John Wiley and sons.

27. Romeo, M., Bak, K., Elfallah, J., Lenormand, F., and Hilaire, L., *XPS Study of the reduction of cerium dioxide.* Surface and Interface Analysis, 1993. **20**(6): p. 508.

Chapter 3 : Experimental apparatus

Introduction

In order to study the properties of a surface at an atomic level, accurate sample characterisation is necessary. This requires the use of UHV conditions in order to cut down the level of surface contaminants and to be able to control surface interactions. The work included in this thesis was performed using two experimental systems, which will be described separately in the following chapter.

FT-RAIRS system

Figure 3.1 shows a diagrammatic representation of the FT-RAIRS system. The UHV chamber consists of three experimental levels. The upper level contains apparatus necessary for sample cleaning and characterisation, including an Ar ion gun (Physical Electronics Inc.), LEED optics (ErLEED-100A, Specs GmbH) with AES capabilities, and a quadrupole mass spectrometer (QMS) (HAL 201, Hiden Analytical Ltd.). An ion gauge is also included on this level for pressure measurement down to UHV. The middle level is used for performing RAIRS experiments, and two differentially pumped KBr IR windows are situated on opposite sides of the chamber. A fourier transform infrared (FTIR) spectrometer and infrared optics are situated externally and allow the transfer of light from the FTIR to the sample and from the sample to the detector. The lower level was used for growing Pd/CeO_{2-x} samples and includes electron-beam Ce and Pd evaporators.

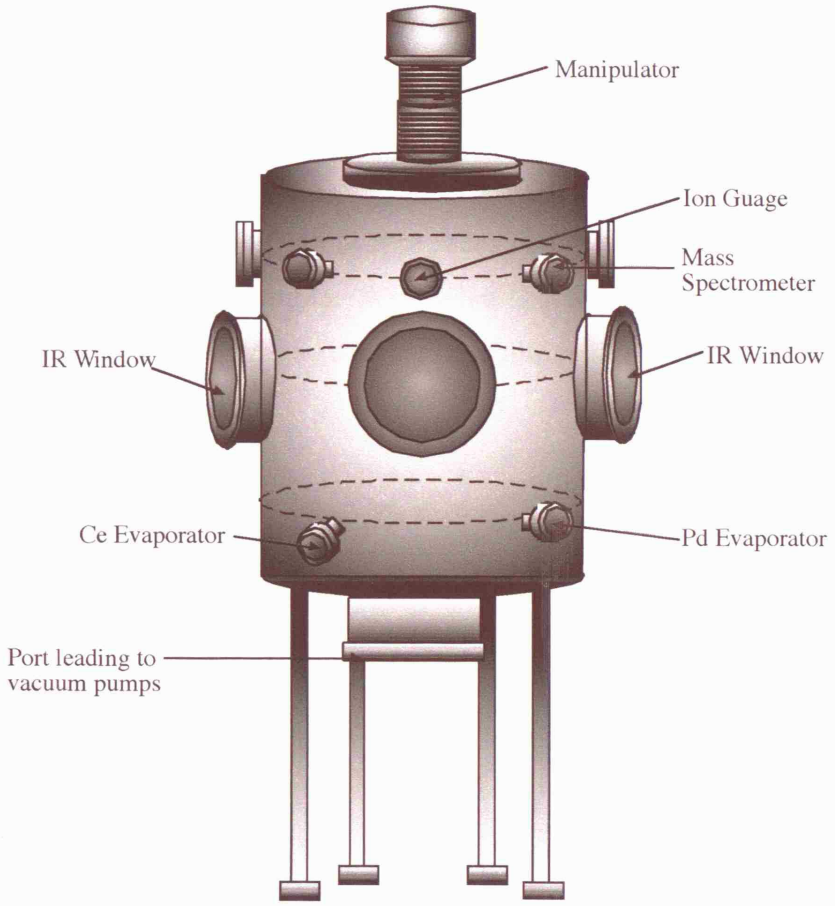

Figure 3.1 A diagrammatic representation of the FT-RAIRS system.

The chamber is also equipped with a high precision leak valve, which was used to deliver sample gas into the chamber. The leak valve was attached to a stainless steel manifold via a length of stainless steel pipe. The manifold connected to 4 separate gas lines, allowing several gases to be dosed into the chamber in succession. The gas manifold could be evacuated using a turbomolecular pump (Turbovac 151, Leybold Ltd.), backed with a rotary pump.

The single crystal sample was mounted on a high precision manipulator (Omniax Translator, MX Series, Vacuum Generators), which allows the sample to be moved in x, y, and z directions with micrometer precision. The sample can also be rotated through 360° through the use of a differentially pumped rotary feedthrough. This allows for accurate sample positioning, which is essential for RAIRS experiments.

The sample was suspended from the bottom of the manipulator using two Tungsten-Rhenium wires that were attached directly to the back of the sample and held in place by a layer of Mo foil. These wires were also used to resistively heat the sample by passing a large current through them. The sample temperature was measured by an N-type thermocouple, which was spot welded directly to the rear of the sample. A detailed description of the sample mount can be found in [1], although the cooling capabilities described were not used in the experiments in this thesis.

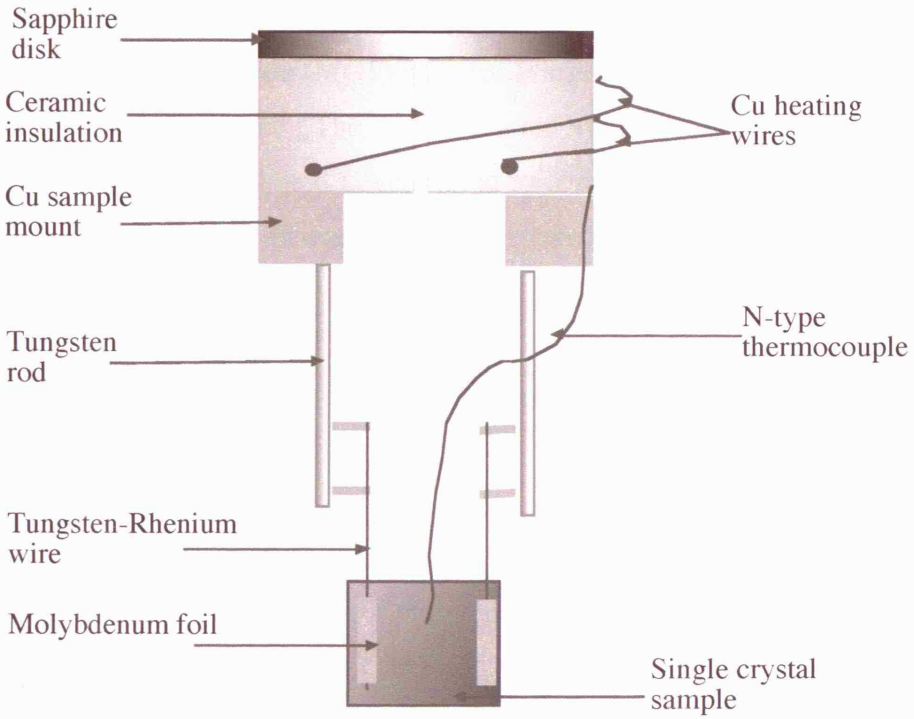

Figure 3.2 Diagram showing the back view of the sample mount which is positioned at the end of the manipulator.

The main experimental chamber is connected via a T-section at the base of the chamber to the pumps which are used to attain UHV. A turbomolecular pump, backed by a rotary vane pump, is used to pump the chamber from atmospheric pressure to high vacuum. In order to obtain UHV the chamber is baked, after which a combined ion and titanium sublimation pump (Captorr ion pump and Boostivac TSP, Physical Electronics) is used. Following this procedure a base pressure of at least 2×10^{-10} mbar is obtained in the main chamber.

RAIRS optical set-up

The RAIRS setup consists of an external FTIR spectrometer from which IR light is emitted. The IR light from the spectrometer is initially reflected off a polished, flat aluminium mirror, and then focused through a differentially pumped KBr window onto the sample at grazing incidence using a 90° off-axis parabolic mirror. Light reflected off the sample passes through a second KBr window before being focused into an IR detector using another 90° off-axis parabolic mirror and a 75° off-axis parabolic mirror. A liquid nitrogen cooled mercury cadmium telluride (MCT) detector is used, which has a spectral range between 700 and 4000 cm^{-1}. The signal detected by the MCT detector is then fed back to the spectrometer, and is converted to a spectrum by a computer using Win-First software. The optical path of the infrared light is shown in Figure 3.3.

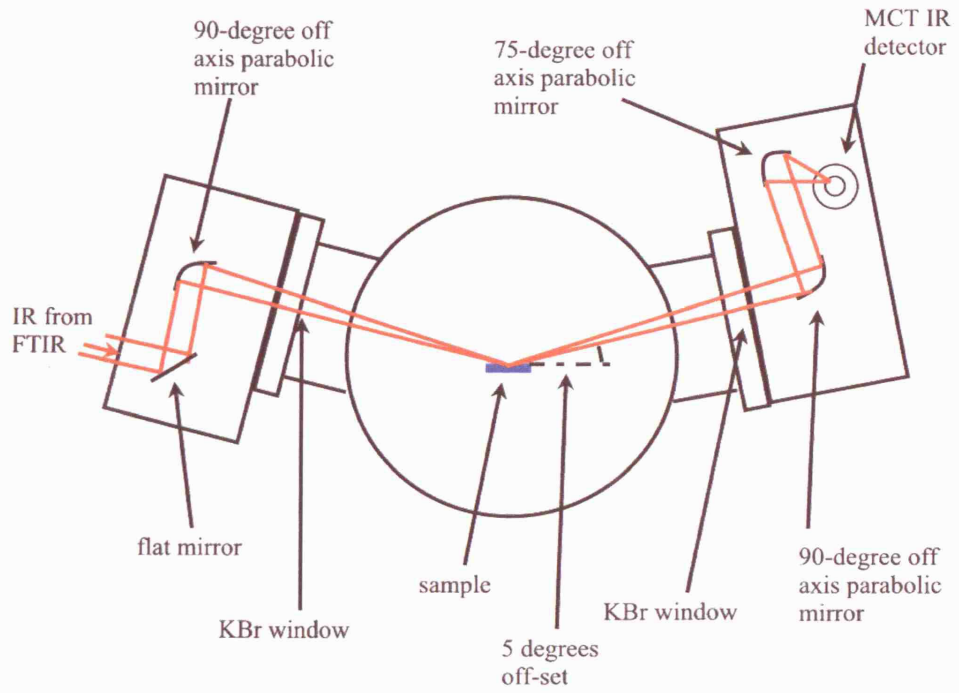

Figure 3.3 A diagram showing the optical path of IR light in a RAIRS experiment.

The IR optics are in two custom-built aluminium boxes, which are purged with dry, CO_2 free air. The spectrometer is also purged in order to prevent

atmospheric absorption bands in the optical path, as without a purge water and CO_2 peaks would be present in the RAIR spectra and would mask any signal observed from sample species.

RAIRS experiments

At the beginning of each set of RAIRS experiments a background spectrum of the clean sample surface was recorded. Sample gas was dosed onto the surface by backfilling the chamber via a high precision leak valve and then a sample spectrum was taken. Subtracting the background spectrum from the sample spectrum then resulted in absorption spectra, which were presented as a plot of $\Delta R/R$ against wavenumber. All RAIR spectra described in this thesis are the result of the coaddition of 512 scans and are taken at a resolution of 8 cm^{-1}, unless otherwise stated.

Desorption experiments were carried out by heating the dosed surface to a predetermined temperature, and then maintaining this temperature for 3 minutes whilst RAIR spectra were taken.

XPS system

Figure 3.4 shows a diagrammatic representation of the XPS vacuum chamber. The main chamber consists of three experimental levels. The upper level contains apparatus necessary for sample cleaning and characterisation, including an Ar ion gun, rear view LEED optics, and a quadrupole mass spectrometer (QMS). An ion gauge is also included on this level for pressure measurement down to UHV. The central level is used for XPS data acquisition and comprises of a hemispherical analyser (VSW/Omicron EA 125) and two viewing ports. The lower level includes the Mg Kα X-ray gun used as the X-ray source in XPS experiments. The chamber is also fitted with e-beam Ce and Pd dosers.

The chamber is also equipped with a high precision leak valve, which was used to deliver sample gas into the chamber. The leak valve was attached via a length of stainless steel pipe to five separate gas lines, allowing several gases to be

dosed into the chamber in succession. The gas line system could be evacuated using a turbomolecular pump, backed with a rotary pump.

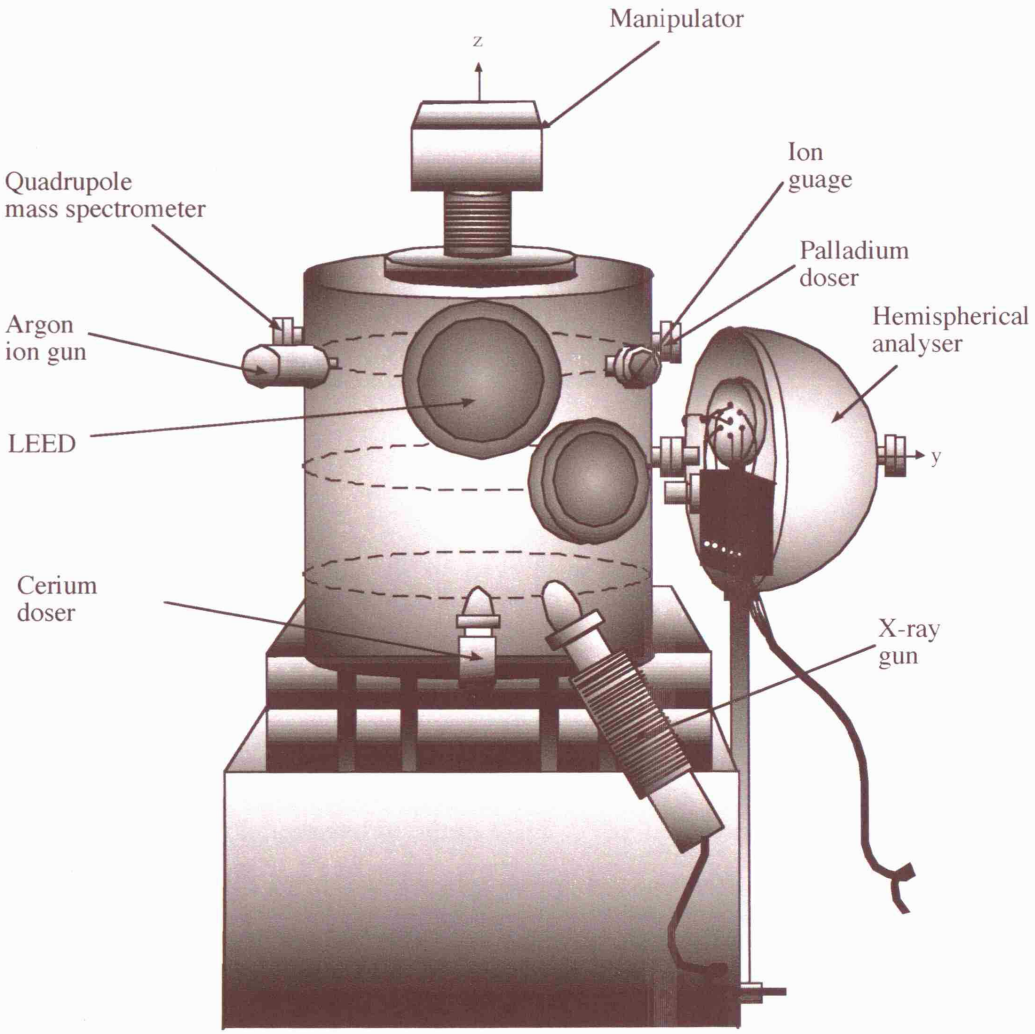

Figure 3.4 A diagram of the XPS vacuum chamber used in this study.

The single crystal sample was mounted on a high precision manipulator, which allows the sample to be moved in x, y, and z directions and rotated through 360°, allowing for accurate sample positioning for XPS data aquisition. The crystal was mounted on a sample holder using two thin tungsten wires that are held tight by screws either side of the sample. The sample holder consists of a back plate, which is electrically isolated from a molybdenum top plate, onto which the sample is mounted. Between the two layers are three tungsten filaments, which are used for electron beam heating of the sample [2], as shown in Figure 3.5. During electron beam heating, high voltage is applied to the back plate, as

current is passed through the tungsten filaments and the molybdenum top plate remains earthed. A K-type thermocouple, attached to the top plate, is used to determine the temperature of the sample.

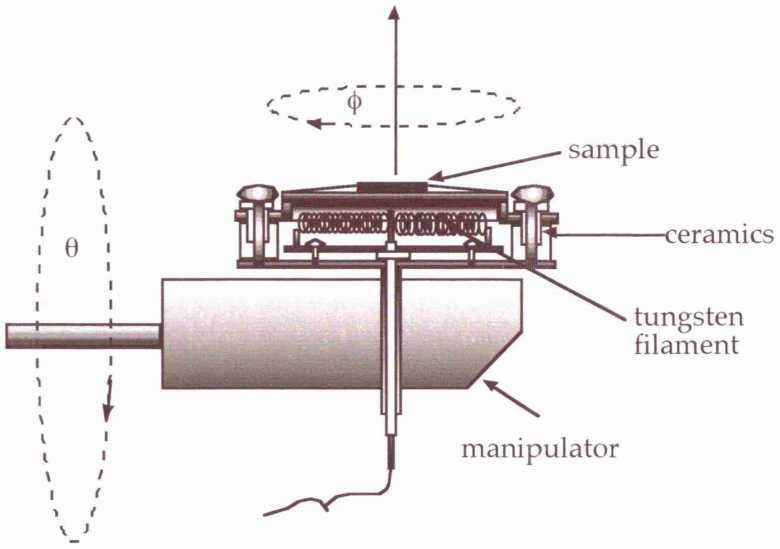

Figure 3.5 A diagram showing the side view of the sample mount used in the XPS system.

The main experimental chamber is connected, at the lower level of the chamber, to the pumps which are used to attain UHV. The chamber is first pumped down via the gas line with a turbo-molecular pump, backed with a rotary vane pump, to a pressure of at least 1×10^{-3} mbar. A water-cooled diffusion pump backed with a rotary vane pump is then used to reach high vacuum. In order to obtain UHV the chamber is baked, after which a titanium sublimation pump is used. Following this procedure a base pressure of at least 2×10^{-10} mbar is obtained in the main chamber. An ion gauge is fitted to the chamber to allow pressure measurement down to UHV.

XPS experiments

For XPS experiments the sample is centred on the entrance slit of the analyser and is aligned perpendicularly with respect to the analyser entrance slit. X-rays are aimed at the sample surface at an angle of 45° with respect to the sample surface. The X-ray source used for XPS experiments had a single Mg anode and

was also equipped with a linear drive mechanism in order to optimize the distance between the X-ray source and the sample.

The main experimental constraints of this technique are related to the production of X-rays by an X-ray gun and the detection of photoelectrons by the hemispherical analyser. The X-ray source being used creates X-rays by bombarding a solid target with high energy electrons. The emission from the target is composed of characteristic line emissions due to the filling of core holes created by the electron beam and background energy due to Bremsstrahlung. In XPS experiments, it is important to have as near a monochromatic X-ray beam as possible. In order to do this, a target with a low Bremsstrahlung background and narrow line emissions should be used. The most common targets used are aluminium and magnesium, which both have spectra dominated by K_{α} emission lines, specifically $K_{\alpha 1,2}$ which is caused by decay from $2p_{1/2} \rightarrow 1s$ and $2p_{3/2} \rightarrow 1s$. The X-ray gun used in this set of experiments uses a Mg target. It is also important to cool the target in order to prevent out-gassing as it is heated by excess energy from the electron bombardment process. Without this additional cooling, which is carried out by circulating cold water, out-gassing would cause fluctuations in the chamber pressure. The X-ray gun also has an aluminium foil window which prevents stray electrons from affecting experiments and filters out unwanted X-ray lines.

The photoelectrons emitted from the sample surface are detected using a hemispherical analyser (Figure 3.6). This consists of two concentric hemispheres with a potential difference placed across them so as to give a positively charged inner hemisphere and negative outer hemisphere with respect to the centre line equidistant between the two. The centre line potential is the pass energy, which remains constant for each scan. The analyser resolution can be defined as $\Delta E/E$, where ΔE is the absolute resolution, and E is the energy of an electron as it passes through the analyser. Both terms will be constant at a constant pass energy. Hence, this relationship proves that the lower the pass energy the higher the resolution will be. However the signal intensity is proportional to the pass energy, therefore as the pass energy decreases and the

resolution increases the signal intensity will decrease. Large pass energies of approximately 100 eV are used for overview scans looking at electrons of a wide range of kinetic energies, whereas lower pass energies, less than 40 eV, are used to acquire high resolution spectra over a narrow band of kinetic energies. Inside the hemispherical analyser, electrons are deflected by an electrostatic field. This results in a fixed range of electron energies that can pass through the analyser without colliding with one of the hemispheres. The magnitude of this range is dependent on the pass energy, the size of entrance and exit slits, and the angle at which the electrons enter the analyser. Once the electrons have passed through the analyser the number of electrons leaving at each energy is counted using a channeltron. The analyser used for this set of experiments utilises multichannel detection using 5 channels.

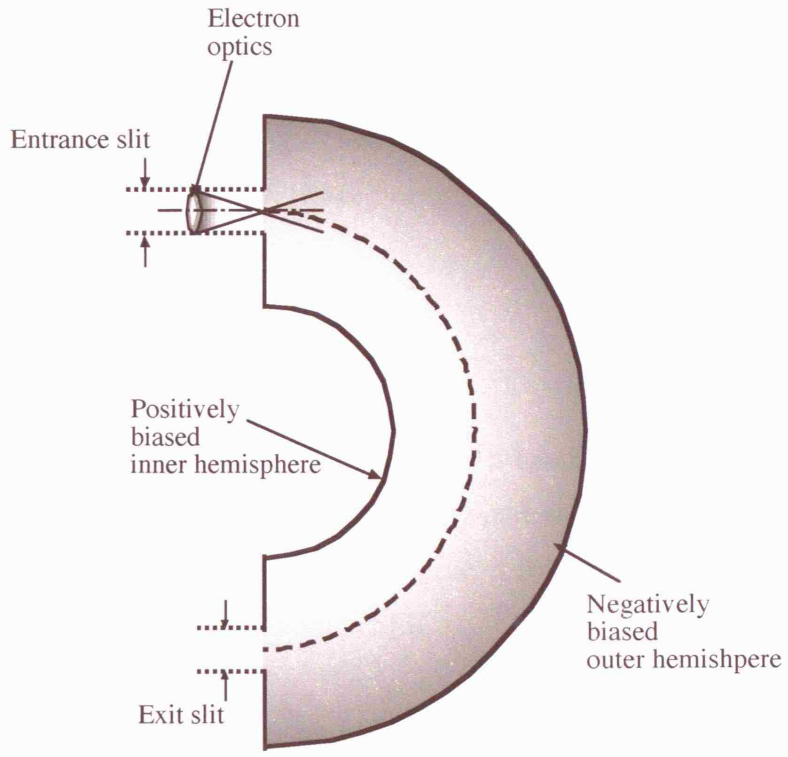

Figure 3.6 A diagrammatic representation of the hemispherical analyser used in these experiments.

Surface preparation and characterisation

The techniques and apparatus used for sample preparation and characterisation will now be described in more detail. Most of the techniques used were the same for both experimental systems, however any differences will be highlighted where appropriate.

Argon ion sputtering

Argon ion sputtering is one of the most widely used techniques for removing contaminants from metal samples. This technique involves the production of an ion beam, from an ion gun, which is focused at the sample surface. The argon ions are inert and collision with surface atoms on the sample results in their repulsion.

Argon ion sputtering of a sample results in a rough, highly defective surface possibly with some Ar remaining. Therefore every cycle of argon ion sputtering is followed by annealing to high temperatures. This results in a smooth, ordered surface with no argon contamination.

LEED

Low Energy Electron Diffraction (LEED) uses a beam of low energy electrons that are diffracted by the sample. The resulting pattern of spots is displayed on a fluorescent screen and can be used to give information about the surface symmetry of the sample or the overlayer [3].

Figure 3.7 shows the typical set up of a reverse view LEED system, similar to those used in both the XPS and RAIRS systems. An electron gun produces a beam of electrons of variable energy which are scattered from the sample surface, resulting in elastically and inelastically scattered electrons. The scattered electrons pass through a series of grids. The first grid is earthed and the fluorescent screen is kept at a high positive potential difference. Hence the elastically scattered electrons are accelerated towards the fluorescent screen with

adequate energy to excite the fluorescence. This results in a pattern of bright spots being seen on the LEED screen. The intermediate grids have a variable negative potential which repels the inelastically scattered electrons, which would otherwise form a bright background, making the diffraction pattern difficult to see. The resulting LEED pattern is recorded using a CCD camera mounted on the outside of the chamber.

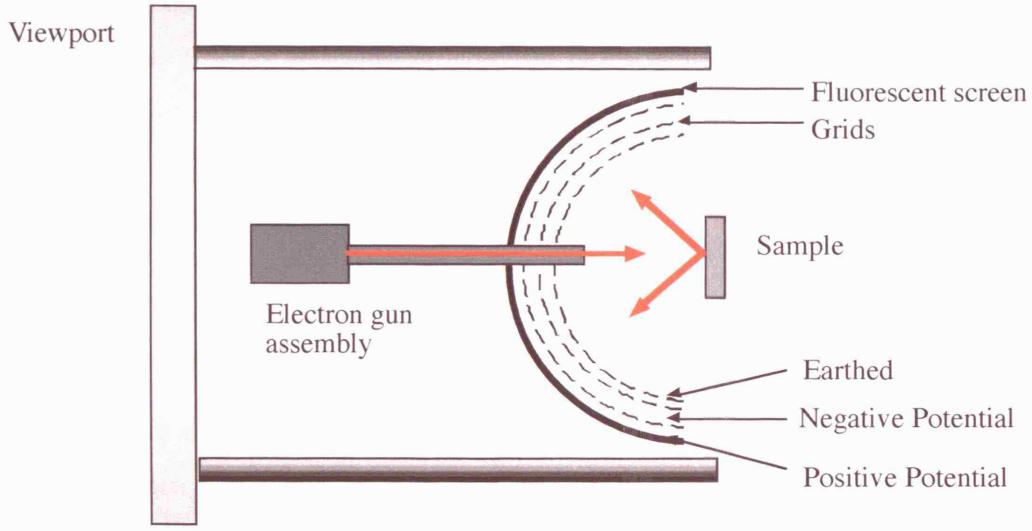

Figure 3.7 A diagram showing a typical reverse view LEED system.

It is possible to gain information from the LEED pattern from analysis of both the spot positions and their intensities. In this study the structural information required can be obtained by solely studying spot positions. However, spot intensities were also used as a comparison between CeO_{2-x} thin films produced in the XPS and RAIRS chambers (see chapter 5 for further detail). The pattern of LEED spots can be used to gain information about surface symmetry and about imperfections in the surface. The LEED pattern observed is a reflection of reciprocal space, hence the distance between the spots seen on the LEED screen will be inversely proportional to the distance between the corresponding points on the sample surface. By comparing the distances between spots, adlayer surface lattice constants can be determined.

AES

Auger electron spectroscopy was used to check the cleanliness and composition of samples in the RAIRS system. XPS was used for this purpose in the XPS chamber. In the RAIRS chamber, AES was carried out using a combined LEED-AES system. Electrons were emitted from an electron gun and focused onto the sample. Incident electrons ionise surface atoms by the production of core holes, which are then filled with electrons from a lower energy state. The resultant energy produced by this process can be released by ejecting a photon or another electron. The process releasing an electron is known as Auger decay, during which an Auger electron is emitted. LEED optics can be operated as a retarding field analyser (RFA), in order to detect the Auger electrons, by placing a modulated retarding voltage on the centre grid [4].

Metal evaporators

Electron beam evaporation techniques were used to evaporate both Ce and Pd onto the surface. The cerium evaporator was based on a design by Arayapochet *et al.* [5]. The evaporator consisted of a molybdenum crucible, which was held at high voltage, with a tungsten filament positioned approximately 5 mm away, as shown in Figure 3.8a. High voltage is applied to the crucible and current is passed through the filament resulting in electron bombardment of the crucible, which is heated adequately to evaporate the cerium foil placed inside. The palladium evaporator consisted of a similar design, however instead of using a crucible to hold the Pd a length of Pd wire was attached to the high voltage connection, as shown in Figure 3.8b.

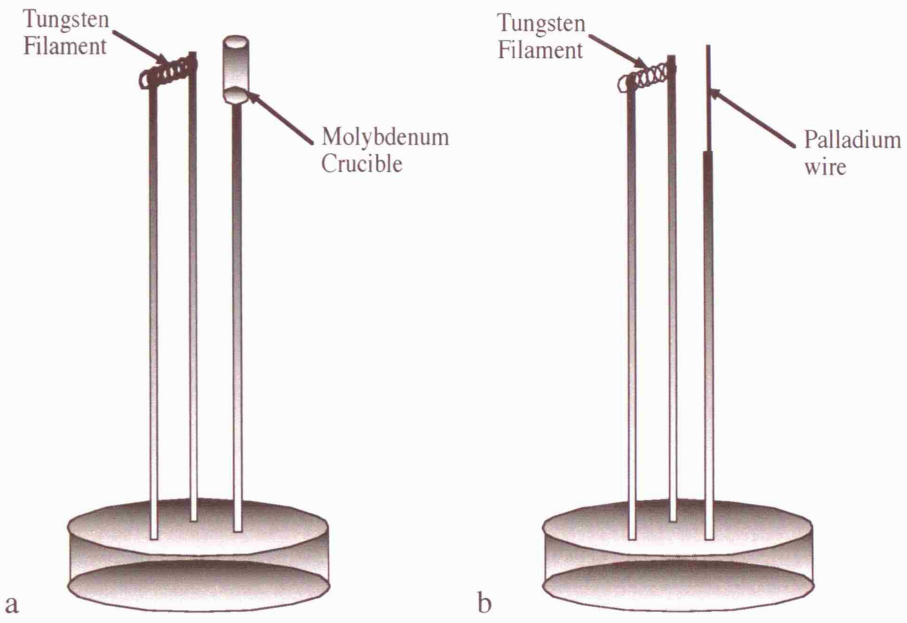

Figure 3.8 Diagrammatic representation of the a) cerium and b) palladium dosers.

References

1. Mukerji, R.J., *PhD Thesis*. 2003, University of London.
2. Michelangeli, E., *PhD Thesis*. 2004, University of Manchester.
3. Woodruff, D.P. and Delchar, T.A., *Modern techniques of surface science*. 2nd ed. Cambridge solid state science series. 1994, Cambridge: Cambridge University Press.
4. Specs, *User's manual: ErLEED optics and power supplies*.
5. Arayapochet, J., Mulhollan, G.A., and Erskine, J.L., *A simple substitute for knudsen cells using an existing pendant-drop type electron-beam evaporator*. Review of Scientific Instruments, 1991. **62**(9): p. 2288.

Chapter 4 : Growing CeO_{2-x} thin films on Pt(111)

Introduction

As already discussed cerium dioxide is a key ingredient in the modern three-way catalytic converter [1], and is known to improve catalytic performance by its ability to store and release oxygen [2, 3]. It is therefore of great interest to be able to reliably determine the oxidation state of ceria samples, and to monitor this as conditions are altered. Bulk CeO_2 has a very low electrical conductivity, and is hence difficult to study using electron spectroscopies, electron diffraction and scanning tunnelling microscopy. In order to overcome this problem CeO_2 thin films grown on metallic substrates can be used as an alternative.

A number of studies into the growth of ceria thin films on Pt(111) have been carried out previously [4-11]. The method of growth used by the Schierbaum group [7] involves reactive adsorption by evaporating cerium at an oxygen pressure of 6×10^{-5} mbar onto a clean Pt(111) crystal at room temperature, resulting in a disordered oxide. The sample is then heated to 1000 K under UHV conditions to form $Pt_5Ce(0001)$, which was shown to exhibit a $(2 \times 2)+(2 \times 2)R30°$ LEED pattern. The sample is then annealed in 6×10^{-5} mbar of oxygen at 1000 K to form a nonstoichiometric CeO_{2-x} thin film with a 1.4×1.4 LEED pattern. STM studies have confirmed the formation of $CeO_2(111)$ surfaces using this method of thin film growth [4, 6].

Hardacre *et al.* [8, 9] have also studied the growth of ceria thin films on Pt(111), using an alternative method to Schierbaum [4, 6, 7]. They deposited Ce onto the clean Pt(111) surface at room temperature in UHV conditions. Oxygen was dosed whilst maintaining the sample temperature at 300 K. The oxygen-saturated samples were then annealed to produce ordered cerium oxide films on top of the Pt(111) crystal. The surface structure of the resultant film proved to be highly dependent on the initial Ce coverage and on the annealing temperature, when using this method of production.

The three layer CeO_{2-x}(111) films used in these experiments were grown in situ using a similar method to that employed by Schierbaum [4, 6, 7]. The method of CeO_{2-x} thin film growth used in the experiments presented in this thesis will be discussed in this chapter. Methods of CeO_{2-x} thin film characterisation and new results related to altering the oxidation state of the CeO_{2-x} will also be presented.

Theory – Oxidation state of ceria thin films

The oxidation state of the cerium dioxide thin films can be estimated using the Ce 3d XP spectrum [7, 8, 12, 13]. After the first well resolved Ce 3d spectra were observed by Burroughs *et al.* in 1976 [13] there was initially some controversy about their interpretation. Currently, the widely accepted interpretation of the Ce 3d spectrum is that it consists of ten Gaussian-like contributions [7, 8, 14]. The additional peaks observed are due to multiplet splitting of the core level Ce 3d peaks. Photoemission causes the creation of core holes in the Ce 3d level, which results in the rearrangement of valence electrons, reducing the energy of the 4 f level, due to reduced electron shielding. This means that hybridisation of the O 2p levels with the Ce 4f levels will occur more readily [12]. This process results in the observation of a number of peaks at different kinetic energies.

In a Ce 3d XP spectrum there are six peaks which can be attributed to Ce^{4+} contributions and four which are due to Ce^{3+}. Hence, if a Ce 3d spectrum were taken of a CeO_2 sample only the six Ce^{4+} structures would be observed, and in the case of Ce_2O_3 only the four Ce^{3+} structures would be seen. However, for a reduced CeO_2 sample all ten peaks will be observed. Table 4.1 shows the binding energies and FWHM of these ten contributions as used in this study. Previous thin film CeO_{2-x}/Pt(111) studies [7, 8], and data for bulk CeO_2 [12] are also shown for comparison. For all cases shown in Table 4.1 the binding energies of the peaks have remained approximately the same, however slightly different FWHM values have been used in each case, possibly due to the different thicknesses of the CeO_{2-x} films used.

Peak	Present study		CeO_{2-x}/Pt(111) [7, 8]		Bulk CeO_2 [12]	
	Binding Energy / eV	FWHM / eV	Binding Energy / eV	FWHM / eV	Binding Energy / eV	FWHM / eV
v_0	880.1	2.3	880.1	2.0	880.60	1.80
v	882.3	2.8	882.3	2.1	882.60	1.80
v'	884.8	3.6	884.8	3.5	885.45	2.80
v''	888.8	4.3	888.8	5.0	888.85	3.08
v'''	898.2	3.1	898.2	2.4	898.40	1.80
u_0	898.8	2.3	898.8	2.9	898.90	1.80
u	901.0	2.8	901.0	2.7	901.05	2.00
u'	903.5	3.6	903.5	3.4	904.05	2.82
u''	907.4	4.3	907.4	4.4	907.45	3.06
u'''	916.7	3.1	916.7	2.7	916.70	2.00

Table 4.1 Notation, binding energies and line widths of the Ce3d photoemission peaks, taken from a number of different studies. Peaks labelled u are $3d_{3/2}$ transitions and those labelled v are $3d_{5/2}$ transitions. Peaks u_0 and v_0 represent the ground state of the core ionised system, whilst the remaining peaks represent various excited states. u', u_0, v', and v_0 are Ce^{3+} peaks, the remainder are Ce^{4+} peaks.

By fitting the 10 Gaussian contributions to a background subtracted Ce 3d spectrum for CeO_{2-x} it is possible to estimate the percentage of Ce^{3+} and Ce^{4+} contributions by comparing the areas under the fitted peaks. Figure 4.1 shows a Ce 3d XP spectrum of a 3 ML CeO_{2-x}(111)/Pt(111) sample, which has a 17.5% Ce^{3+} contribution. For all peak fitting of the Ce 3d spectra in this thesis the same binding energies and peak widths of the 10 Gaussians have always been used, as given in Table 4.1. The intensity ratio of the spin-orbit split doublets was set to a value of 1.5. The residuals were also monitored, as shown in Figure 4.1, in order to monitor the accuracy of the fitting procedure.

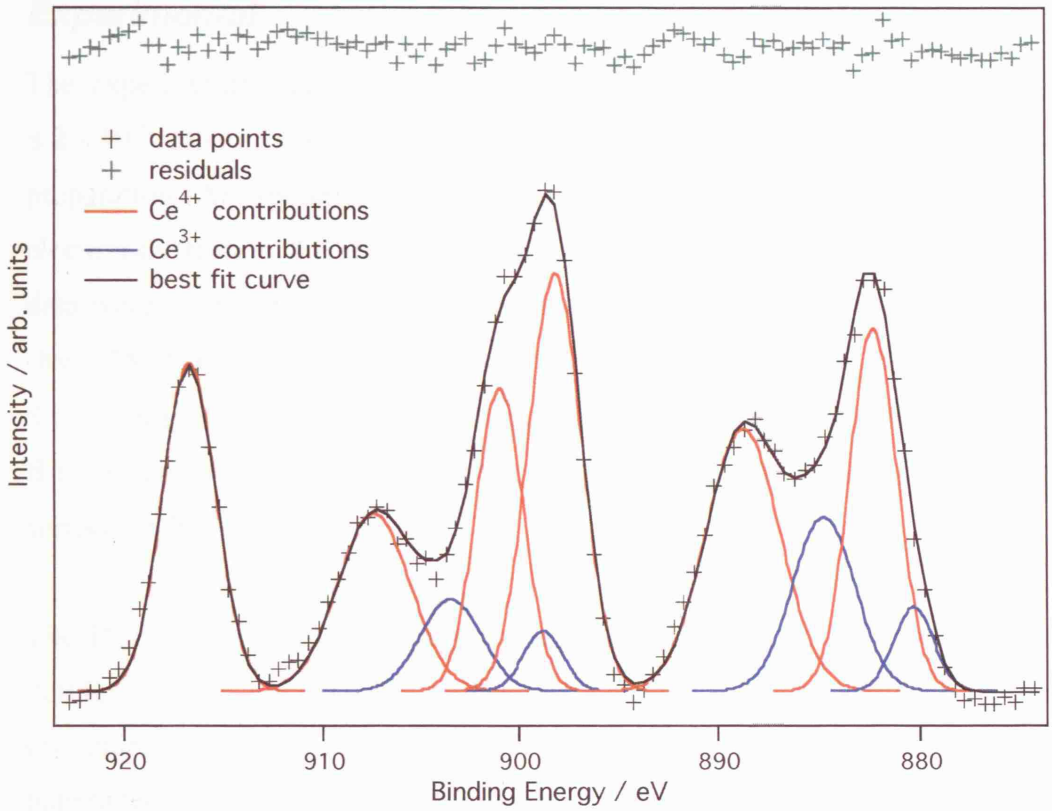

Figure 4.1 Deconvolution of background-subtracted Ce 3d core level spectra for a 3 ML CeO_{2-x}/Pt(111) sample at 300 K. Red Gaussians show the Ce^{4+} contributions, and blue Gaussians represent Ce^{3+} contributions. Residuals plotted are the difference between the data points and the best fit curve, and they have been offset for clarity.

The value of x for the CeO_{2-x} thin films can be calculated using the following equation, taken from [7]:

$$x = \frac{1}{2}\frac{v_0 + v' + u_0 + u'}{\Sigma(u+v)} \qquad \textbf{Equation 4.1}$$

where v_0, v', u_0, and u' are the areas under the Ce^{3+} related peaks, as indicated in Table 4.1. Therefore, for example, if a CeO_{2-x} thin film has a 17.5% Ce^{3+} concentration the value of x is calculated to be 0.0875.

Experimental

The experiments were performed in a UHV chamber with a base pressure $\leq 2 \times 10^{-10}$ mbar. The system contained all facilities necessary for sample preparation (Ar^+ sputtering and annealing) and characterisation (low energy electron diffraction (LEED) and X-ray photoelectron spectroscopy (XPS)). All data were recorded at room temperature, using unpolarised Mg Kα radiation (hν=1253.6 eV) as the photon source and a VSW/Omicron EA125 with a 5-channeltron detection system to analyse the photoelectrons (see chapter 3). Binding energies are referred to the Pt $4f_{7/2}$ core level of the clean Pt(111) surface, at 70.9 eV.

The Pt(111) sample was cleaned by repeated cycles of Ar ion sputtering at 300 K, and annealing at 1050 K. Sample cleanliness was confirmed if surface contamination was below the detectable limit of XPS, and if the expected LEED pattern for Pt(111) was observed.

O_2 was dosed into the chamber at room temperature via a high precision leak valve. The ion gauge sensitivity was not corrected for O_2. All exposures are measured in Langmuir (L), where 1 L is equivalent to a dose of 1.32×10^{-6} mbar for 1 second. The sample was electron-beam heated and the sample temperature was measured by a K-type thermocouple, attached to the sample back plate.

The three layer $CeO_{2-x}(111)$ films used in these experiments were grown in situ using a similar method to that employed by Schierbaum [7]. Cerium was evaporated onto the clean Pt(111) surface using electron beam evaporation in UHV conditions, which results in a disordered cerium layer with no clear LEED pattern. The sample was annealed to 1020 K in UHV, resulting in an ordered surface structure exhibiting a 2 × 2 LEED pattern, as shown in Figure 4.2. The sample was then annealed in 1×10^{-5} mbar O_2 to 1020 K for 3 minutes, which results in a $CeO_{2-x}(111)$ thin film with a 1.4 × 1.4 LEED pattern with respect to the LEED pattern for the clean Pt(111) surface, as shown in Figure 4.3.

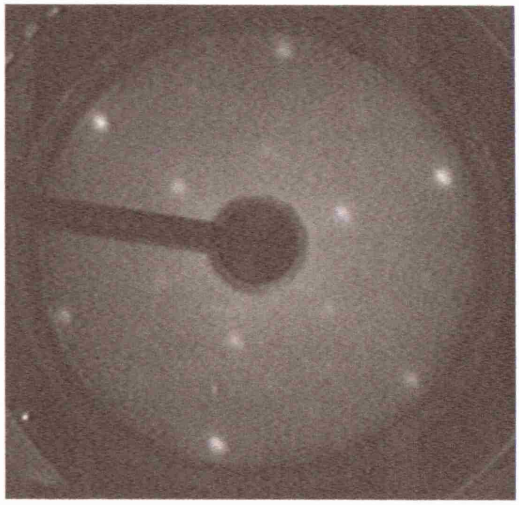

Figure 4.2 LEED pattern of the 3 ML Ce/Pt(111) surface after annealing to 1020 K in UHV. 2 × 2 and Pt(111) 1 × 1 spots are observed. The LEED pattern has been recorded at a beam energy of 45 eV.

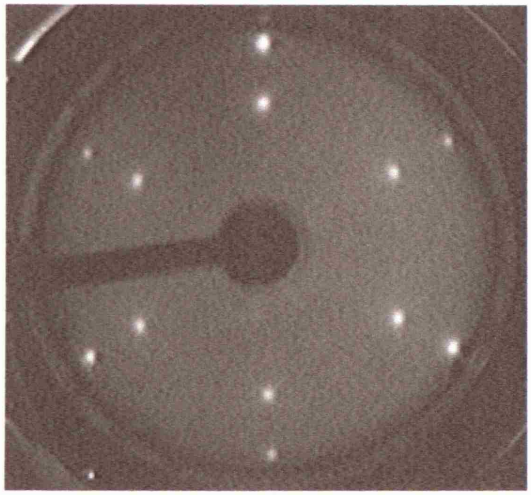

Figure 4.3 LEED pattern of the 3 ML CeO_{2-x}/Pt(111) surface after annealing to 1020 K in 1 × 10^{-5} mbar O_2 for 3 minutes. Pt(111) 1 × 1 and CeO_{2-x}(111) 1.4 × 1.4 spots are observed. The LEED pattern has been recorded at a beam energy of 45 eV.

Ce dosing and oxidation were carried out layer-by-layer to ensure even oxidation of the thin film. Figure 4.4 shows the Ce 3d XP spectra at all stages in the growth of a 3 layer CeO_{2-x}(111) film, and Figure 4.5 shows how the Ce^{3+} concentration varies according to the CeO_{2-x} film thickness.

The ceria film thickness was determined from the attenuation of Pt 4f and Ce 3d photoemission intensities. Film thicknesses quoted are approximations only and have been calculated using a quantification method devised by Seah et al. [15]. This method compares intensities of the substrate and adsorbate peaks in an XPS spectrum, in this case Pt 4f and Ce 3d. By using this information and constants, such as the cross sections of the substrate and adsorbate, and the kinetic energies of the relevant peaks in the spectra, the thickness of the adsorbate layer can be calculated (for parameters used see Appendix).

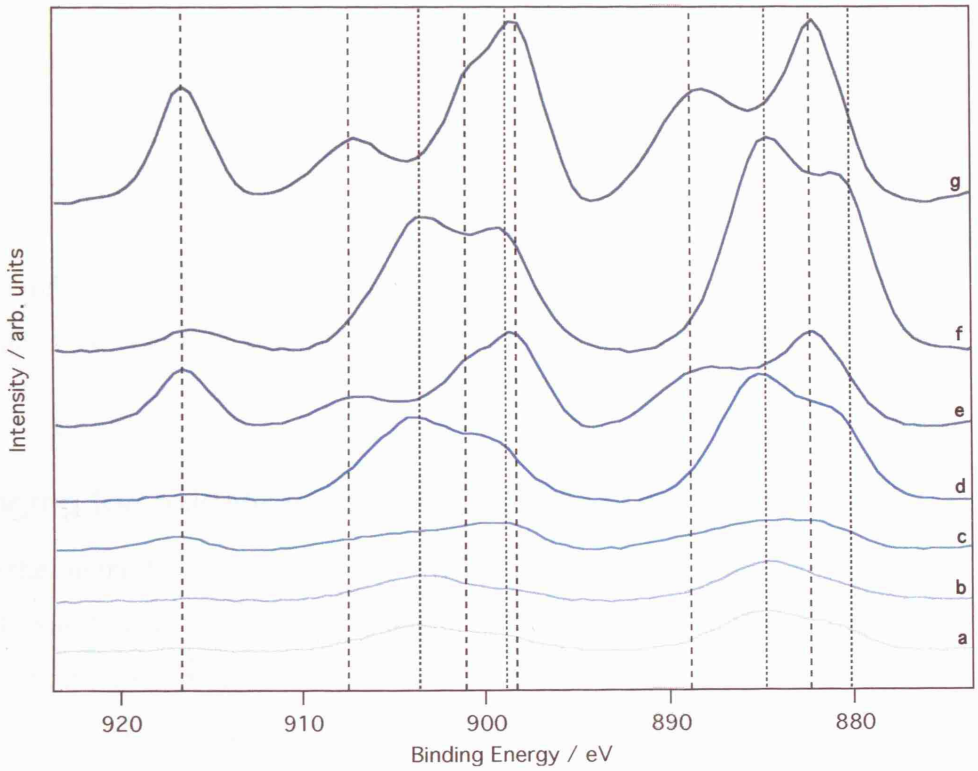

Figure 4.4 XPS spectra of the Ce 3d core level for (a) the as-deposited cerium layer; (b) after annealing the sample in UHV at 900 K for 5 minutes; (c) after annealing in O_2 (300 L); (d) after a second deposition of cerium; (e) after annealing in O_2 (300 L); (f) after a third deposition of cerium; (g) after annealing in O_2. Dashed vertical lines show the positions of Ce^{4+} related contributions and dotted lines show the positions of Ce^{3+} related contributions, as shown in Table 4.1.

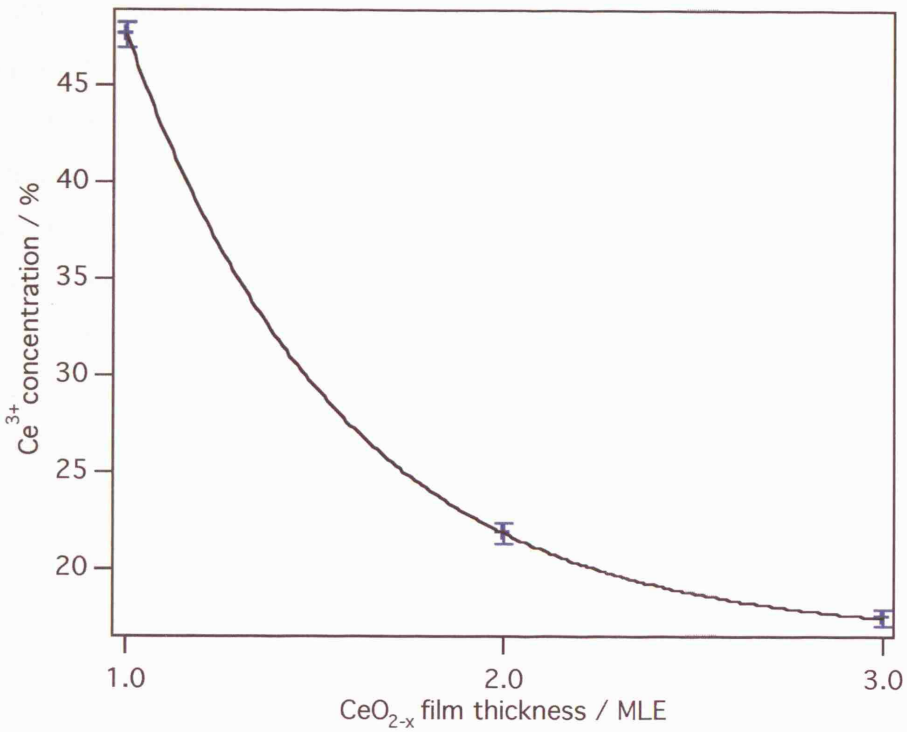

Figure 4.5 Graph showing the dependency of Ce^{3+} concentration on the CeO_{2-x} film thickness. The Ce^{3+} concentrations have been calculated using Ce 3d XPS.

Changing the oxidation state of CeO_{2-x}(111) thin films

Using the method described above, 3 MLE CeO_{2-x}(111) thin films grown on the Pt(111) single crystal consistently resulted in films with a 17.5 ± 0.4% Ce^{3+} contribution. It was found that annealing this film for 1 minute to 970 K in UHV resulted in an increase of up to 15% in the Ce^{3+} concentration, as shown in Figure 4.6, where the Ce^{3+} concentration has been increased from 17.5 ± 0.4% ($CeO_{1.91}$) to 32.2 ± 0.5% ($CeO_{1.84}$). Figure 4.6 also shows that further annealing at 970 K had no effect on the oxidation state of the CeO_{2-x} thin film. Figure 4.7 shows the O 1s spectra for the CeO_{2-x} thin film before and after annealing at 970 K. The intensities of the O 1s peaks were calculated, as given in Figure 4.8, and it can be clearly seen that the O 1s peak intensity decreases after annealing at 970 K. However, the CeO_{2-x} 1.4 × 1.4 LEED pattern is still observed after annealing, suggesting that the reduced ceria thin film is still of (111) configuration.

From Ce^{3+} concentration calculations, there has been a decrease in the amount of oxygen present in the CeO_{2-x} thin films by approximately 3.7% after annealing the sample to 970 K in UHV conditions for 1 minute. From Figure 4.8 it is estimated that there has also been an approximate decrease of 3.6% in the amount of oxygen present on the sample surface. Therefore the reduction of oxygen present in the CeO_{2-x} thin film after annealing is approximately the same as the reduction of oxygen from the sample surface, which suggests that the increase in Ce^{3+} concentration is due to oxygen desorption from the sample surface, and not due to oxygen migration into the Pt substrate.

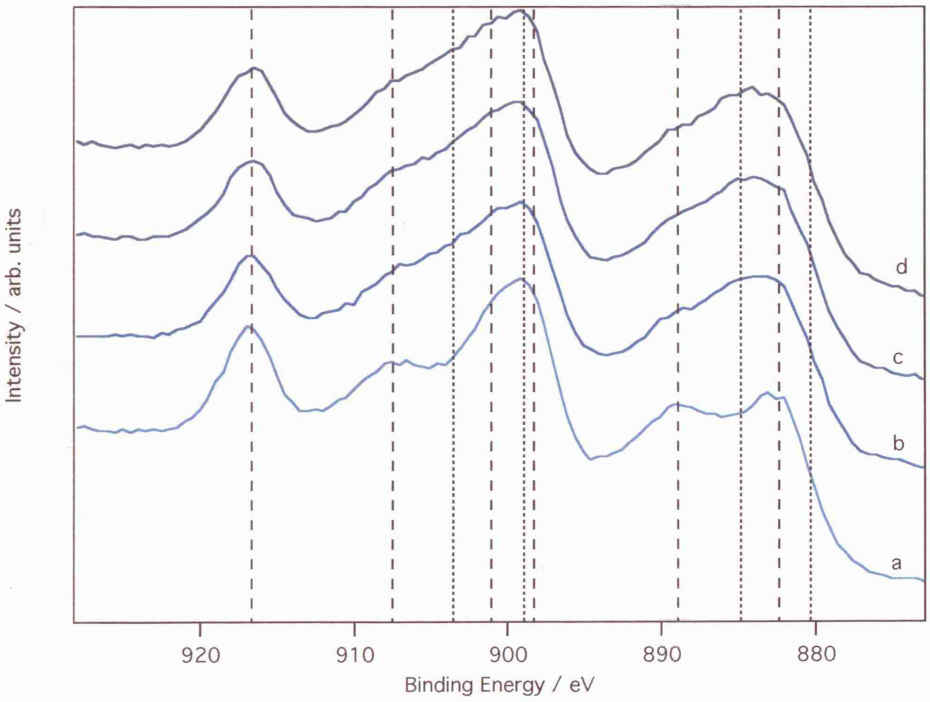

Figure 4.6 Ce3d XP spectra of a 3 MLE CeO_{2-x} thin film on Pt(111) a) after being annealed in UHV and O_2 to produce a 17.5% Ce^{3+} concentration, b) after subsequent annealing in UHV for 1 minute to 970 K, c) after 2 minutes annealing in UHV at 970 K, d) after 3 minutes annealing in UHV at 970 K. Dashed vertical lines show the positions of Ce^{4+} related contributions and dotted lines show positions of Ce^{3+} related contributions, as shown in Table 4.1.

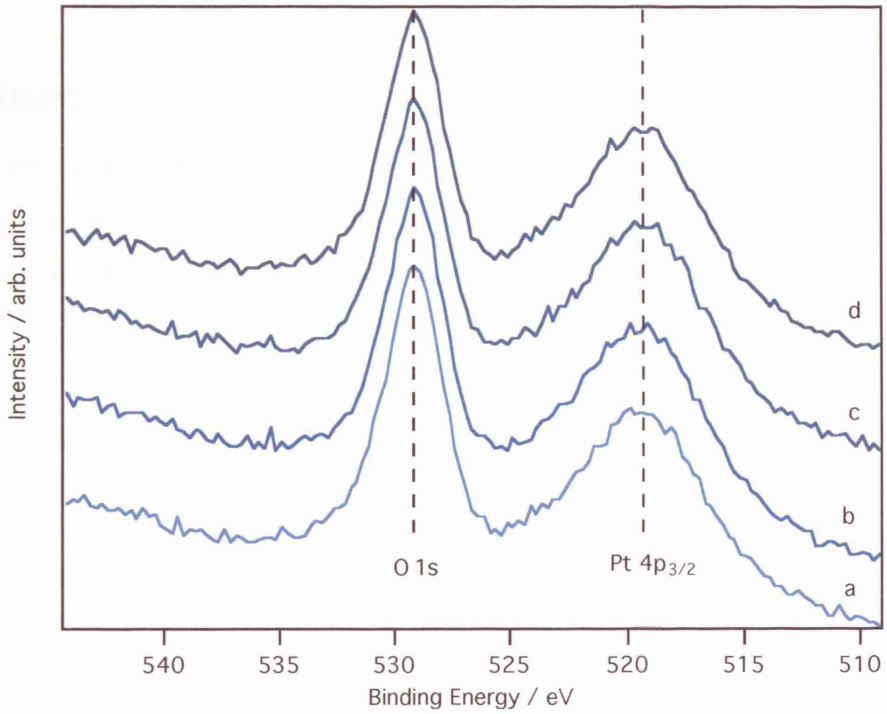

Figure 4.7 O 1s XP spectra of a 3 MLE CeO_{2-x} thin film on Pt(111) a) after being annealed in UHV and O_2 to produce a 18% Ce^{3+} concentration, b) after subsequent annealing in UHV for 1 minute to 970 K, c) after 2 minutes annealing in UHV at 970 K, d) after 3 minutes annealing in UHV at 970 K.

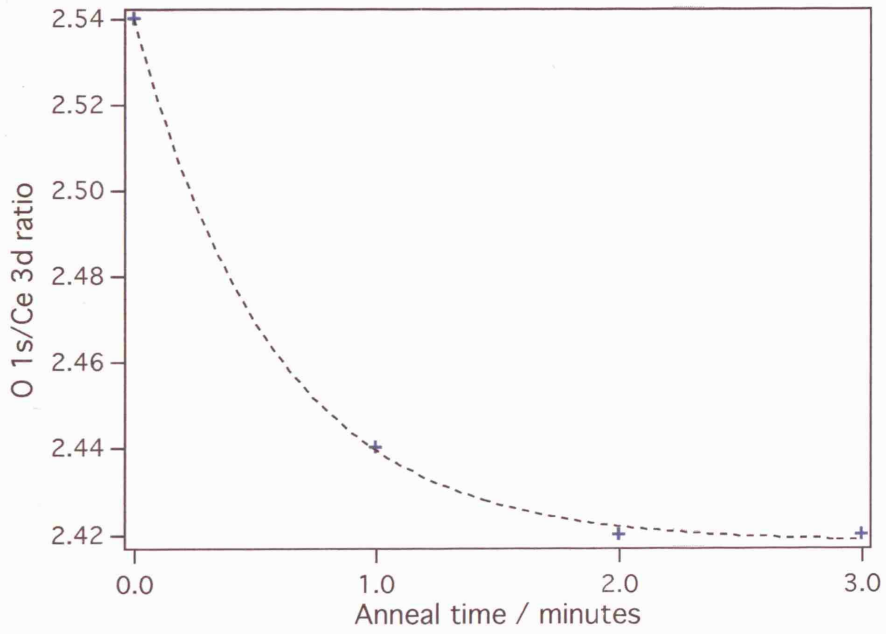

Figure 4.8 A graph showing the ratio of intensities of the O 1s to Ce 3d XPS peaks of the CeO_{2-x}/Pt(111) sample after annealing to 970 K in UHV conditions.

Conclusions

XPS and LEED studies of the growth of CeO_{2-x}(111) thin films on Pt(111) have been successfully carried out. The oxidation state of the CeO_{2-x} thin films has been calculated, and the Ce^{3+} concentration has been altered using vacuum annealing. It has also been determined that upon annealing CeO_{2-x}/Pt(111) to 970 K in UHV conditions, oxygen desorbs from the surface as opposed to migrating into the platinum.

References

1. Heck, R. and Farrauto, R., *Catalytic Air Pollution Control - Commercial Technology*. 1995, New York: Van Nostrand Reinhold.
2. Diwell, A.F., Rajaram, R.R., Shaw, H.A., and Truex, T.J., *The role of Ceria in three-way catalysts*, in *Catalysis and Automotive Pollution Control II*, A. Crucq, Editor. 1991, Elsevier Science Publishers: Amsterdam. p. 139.
3. Trovarelli, A., *Catalysis by ceria and related materials*. Catalytic Science Series, ed. G. Hutchings. Vol. 2. 2000, London: Imperial College Press.
4. Berner, U. and Schierbaum, K.-D., *Cerium oxide layers on Pt(111): a scanning microscopy study*. Thin Solid Films, 2001. **400**(1-2): p. 46.
5. Berner, U., Schierbaum, K.-D., Jones, G., Wincott, P., Haq, S., and Thornton, G., *Ultrathin ordered CeO_2 overlayers on Pt(111): interaction with NO_2, NO, H_2O and CO*. Surf. Sci., 2000. **467**: p. 201.
6. Berner, U. and Schierbaum, K.-D., *Cerium oxides and cerium-platinum surface alloys on Pt(111) single-crystal surfaces studied by scanning tunneling microscopy*. Phys. Rev. B, 2002. **65**: p. 235404.
7. Schierbaum, K.-D., *Ordered ultra-thin cerium dioxide overlayers on Pt(111) single crystal surfaces studied by LEED and XPS*. Surf. Sci., 1998. **399**: p. 29.
8. Hardacre, C., Roe, G.M., and Lambert, R.M., *Structure, composition and thermal properties of cerium oxide films on Pt(111)*. Surf. Sci., 1995. **326**: p. 1.
9. Hardacre, C., Ormerod, R.M., and Lambert, R.M., *Platinum promoted catalysis by ceria: a study of carbon monoxide oxidation over $Pt(111)/CeO_2$*. J. Phys. Chem., 1994. **98**: p. 10901.
10. Pfau, A. and Schierbaum, K.-D., *The electronic structure of stoichiometric and reduced CeO_2 surfaces: an XPS, UPS and HREELS study*. Surf. Sci., 1994. **321**: p. 71.
11. Pfau, A., Schierbaum, K.D., and Gopel, W., *The electronic structure of CeO_2 thin films: the influence of Rh surface dopants*. Surf. Sci., 1995. **331-333**: p. 1479.

12. Romeo, M., Bak, K., Elfallah, J., Lenormand, F., and Hilaire, L., *XPS Study of the reduction of cerium dioxide.* Surface and Interface Analysis, 1993. **20**(6): p. 508.

13. Burroughs, P., Hamnett, A., Orchard, A.F., and Thornton, G., *Satellite structure in x-ray photoelectron-spectra of some binary and mixed oxides of lanthanum and cerium.* Journal of the Chemical Society-Dalton Transactions, 1976(17): p. 1686.

14. Mullins, D.R., Overbury, S.H., and Huntley, D.R., *Electron spectroscopy of single crystal and polycrystalline cerium oxide surfaces.* Surf. Sci., 1998. **409**: p. 307.

15. Seah, M.P., *Quantification of AES and XPS*, in *Practical Surface Analysis - Auger and X-ray Photoelectron Spectroscopy*, D. Briggs and M.P. Seah, Editors. 1983, Wiley. p. 201.

Chapter 5 : RAIRS studies of CO adsorption on $Pd/CeO_{2-x}/Pt(111)$

Introduction

Ceria, platinum and palladium are all key ingredients in modern three-way catalytic converters [1]. By studying the interaction of CO with the $Pd/CeO_{2-x}/Pt(111)$ surface more information can be learnt about the mechanisms of the catalytic reaction at the atomic level. RAIRS studies of these surface interactions can also give information about the morphology of the $Pd/CeO_{2-x}/Pt(111)$ surface.

Extensive research has previously been done into the adsorption of CO onto various Pd single crystal surfaces [2-9]. CO is an ideal infrared probe which will tell us about the adsorption sites present on the Pd clusters. However, until this time no studies have been carried out to observe the effect of Pd clusters on the adsorption of CO on $CeO_{2-x}/Pt(111)$ surfaces. Mixed powder samples of CeO_2/Pt and CeO_2/Pd have been studied previously using FT-IR, and measurements have been made at high temperatures and high pressures of CO [10-14]. In these cases a wide variety of infrared bands were observed that would not be expected to be seen in room temperature studies, such as the one carried out here. CO adsorption onto reduced CeO_2 thin films on Pt(111) has also been studied using RAIRS [15]. In this study it was found that the ceria formed islands, leaving uncoated Pt sites onto which the CO adsorbed.

More in-depth studies have been carried out on other metal/oxide surfaces, and a number of reviews have been written on the subject [16-20]. Extensive research of CO adsorption on Pd clusters grown on Al_2O_3 thin films has been carried out [2, 3, 16, 17, 21-27]. STM studies [21] have shown that palladium particles grown on $Al_2O_3/NiAl(110)$ at room temperature are cubo-octahedral in shape with a flat (111) top, and (111) and (100) lateral facets. RAIRS experiments have shown good agreement with these observations, as peaks which can be assigned to CO-Pd(111) and (100) stretching frequencies have been observed.

Within the large number of studies that have employed vibrational spectroscopic techniques to observe the CO interaction with the Pd/Al_2O_3 surface, a wide variety of methods have been employed to grow the Pd clusters. This enables the effects of different temperature conditions on the structure of Pd clusters to be observed, and CO has been used as a probe in order to learn about the surface structure [23, 24]. Studies have shown that the size of the Pd clusters has a significant effect on the types and intensities of vibrational modes observed [3, 23-25, 27]. The effects of elevated temperatures and high pressure CO exposure on the Pd/Al_2O_3 surface have also been studied [2, 3, 25, 27], as this mimics the operating conditions of a catalytic converter more closely than low temperature and pressure experiments. However, room temperature studies are still thought to be of relevance to catalytic converter design, due to the fact that current three-way catalytic converters are least effective at low temperatures before the car engine has reached its normal operating temperature.

A number of RAIRS studies have also been carried out on Pd particles grown on SiO_2/Mo(112) [3, 28, 29]. These studies have suggested that the Pd particles, when grown at room temperature, form islands with both (111) and (100) facets. These conclusions have been reached by comparison of CO-Pd RAIRS peaks on the Pd/SiO_2/Mo(112) surface with CO adsorption on Pd single crystals. These experiments are in good agreement with experiments on CO adsorption on alumina supported Pd clusters however, it has been shown that the Pd particles grown on the SiO_2 thin films are more disordered than those observed on alumina surfaces [29].

Despite recent intensive research into ceria and its role as an automobile exhaust catalyst when in combination with noble metals, such as Pd, Pt and Rh, relatively few vibrational spectroscopic studies have been carried out to investigate the interaction of species such as CO with the ceria/noble metal surface. In this study the CO interaction with Pd clusters deposited on reduced CeO_2 thin films, grown on a Pt(111) crystal, has been studied using FT-RAIRS. The observed CO stretching frequencies have been used to deduce structural information about

the surface, and about the Pd clusters deposited on the surface. Experiments have been performed on surfaces with varying amounts of Pd deposited on the CeO_{2-x}/Pt(111) surface. CO adsorption and desorption experiments have been carried out.

Experimental

The experiments were performed in a UHV chamber with a base pressure of at least 2×10^{-10} mbar. The system contained all facilities necessary for sample preparation (Ar^+ sputtering and annealing) and characterisation (Low Energy Electron Diffraction (LEED) and Auger Electron Spectroscopy (AES)). Further details of the FT-RAIRS system are included in chapter 3. All RAIR spectra shown are the result of the coaddition of 512 scans and are taken at a resolution of 8 cm^{-1}, unless otherwise stated.

CO was dosed onto the surface at room temperature via a high precision leak valve. The ion gauge sensitivity was not corrected for CO. All exposures are measured in Langmuir (L), where 1 L is equivalent to a dose of 1.32×10^{-6} mbar for 1 second. The sample was resistively heated via Tungsten-Rhenium wire that was attached directly to the back of the sample and held in place by a layer of Mo foil. The sample temperature was measured by an N-type thermocouple, which was also spot welded directly to the rear of the sample. CO desorption experiments were carried out by heating the sample to a predetermined temperature, and then maintaining this temperature for 3 minutes whilst RAIR spectra were taken.

Cerium was deposited from an electron beam evaporator and CeO_{2-x} thin films were grown using the method described in chapter 4. The CeO_{2-x} thin films used for all the experiments in this chapter are thought to consist of approximately 17.5% Ce^{3+}, as calculated previously using Ce3d XPS (chapter 4). The number of monolayers of CeO_{2-x} on the Pt(111) sample was calculated by comparing LEED spot intensities to those taken in the XPS chamber, where the film thickness was calculated using XPS peak intensities (chapter 4). The ratio of

spot intensities of Pt 1 × 1 compared to CeO_{2-x} 1.4 × 1.4 was calculated at the same beam energies in all cases. It was found that the intensity of the CeO_{2-x} 1.4 × 1.4 spots was 50% of the intensity of the Pt 1 × 1 spots taken at a beam energy of 45 eV for a 3 MLE CeO_{2-x} thin film. The same CeO_{2-x} thin film could not be used for multiple experiments due to CO contamination. Hence, before each set of experiments the sample was cleaned and a new CeO_{2-x} thin film was grown. An identical growth process was used in each case, and each set of RAIRS data was repeated to ensure consistency of results.

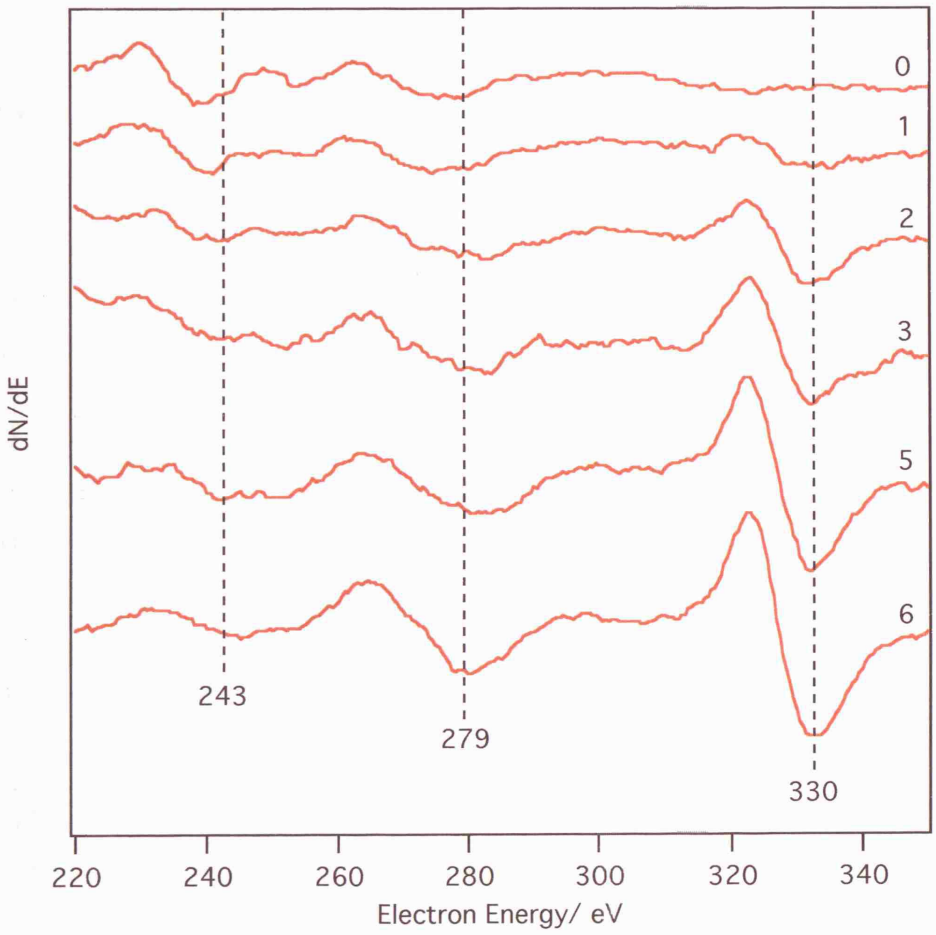

Figure 5.1 AES spectra showing the Pd(MNN) peaks and how they develop as the time spent dosing Pd increases. The spectra are labelled 0-6, indicating the Pd deposition time in minutes.

Palladium was evaporated onto the sample at room temperature from a piece of wire, using an electron beam evaporator, see chapter 3. The palladium doser was

calibrated by dosing Pd onto the clean Pt(111) surface for known periods of time and monitoring the Pd peak-to-peak heights using AES (Figure 5.1). Palladium grows on Pt(111) according to a layer-by-layer growth model [30], hence the Pd AES signal will increase linearly with time until the first monolayer of Pd has been deposited. After the 1 ML Pd coverage has been achieved the signal will continue to increase linearly with time, but the gradient will be different to before. This is shown in Figure 5.2, where 1 ML Pd coverage was reached after dosing for 3 minutes 50 seconds. Palladium does not grow in a layer-by-layer mode on $CeO_{2-x}(111)$, so palladium coverage will be expressed in monolayer equivalents (MLE), where 1 MLE is the equivalent amount of palladium that would be required to completely cover the surface with one layer of palladium atoms.

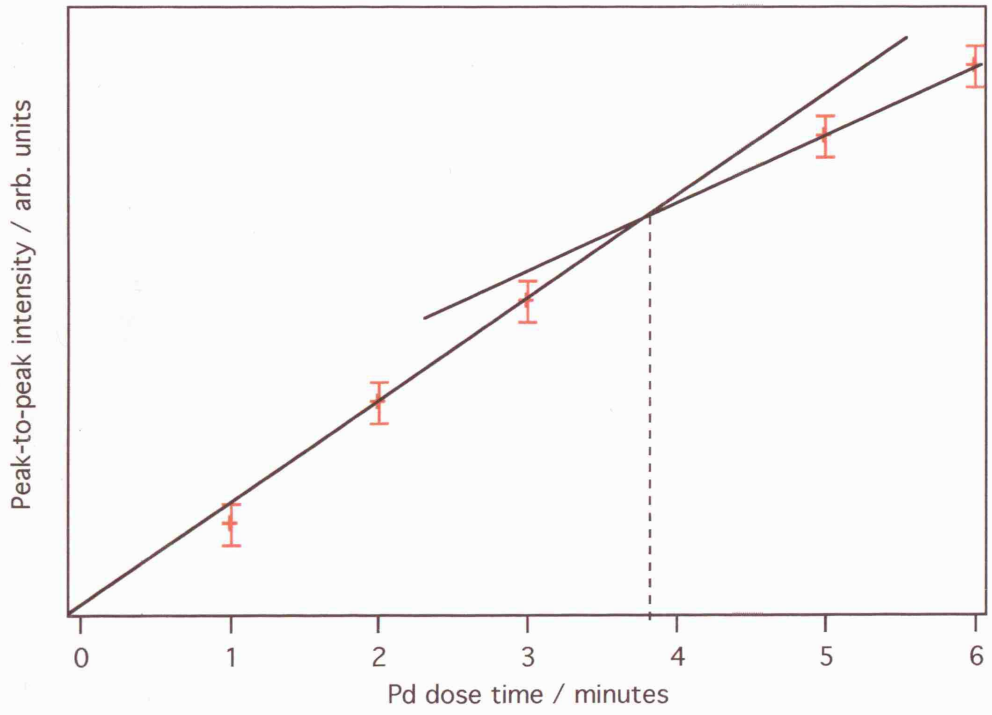

Figure 5.2 Pd(MNN) AES peak-to-peak intensity plotted against the Pd deposition time.

Results and discussion

CO adsorption

CO adsorption on CeO_{2-x}(111)/Pt(111)

RAIR spectra taken after a number of CO doses onto the CeO_{2-x}/Pt(111) surface (Figure 5.3) show both CO-Pt(111) atop and bridge stretching frequencies [4, 31].

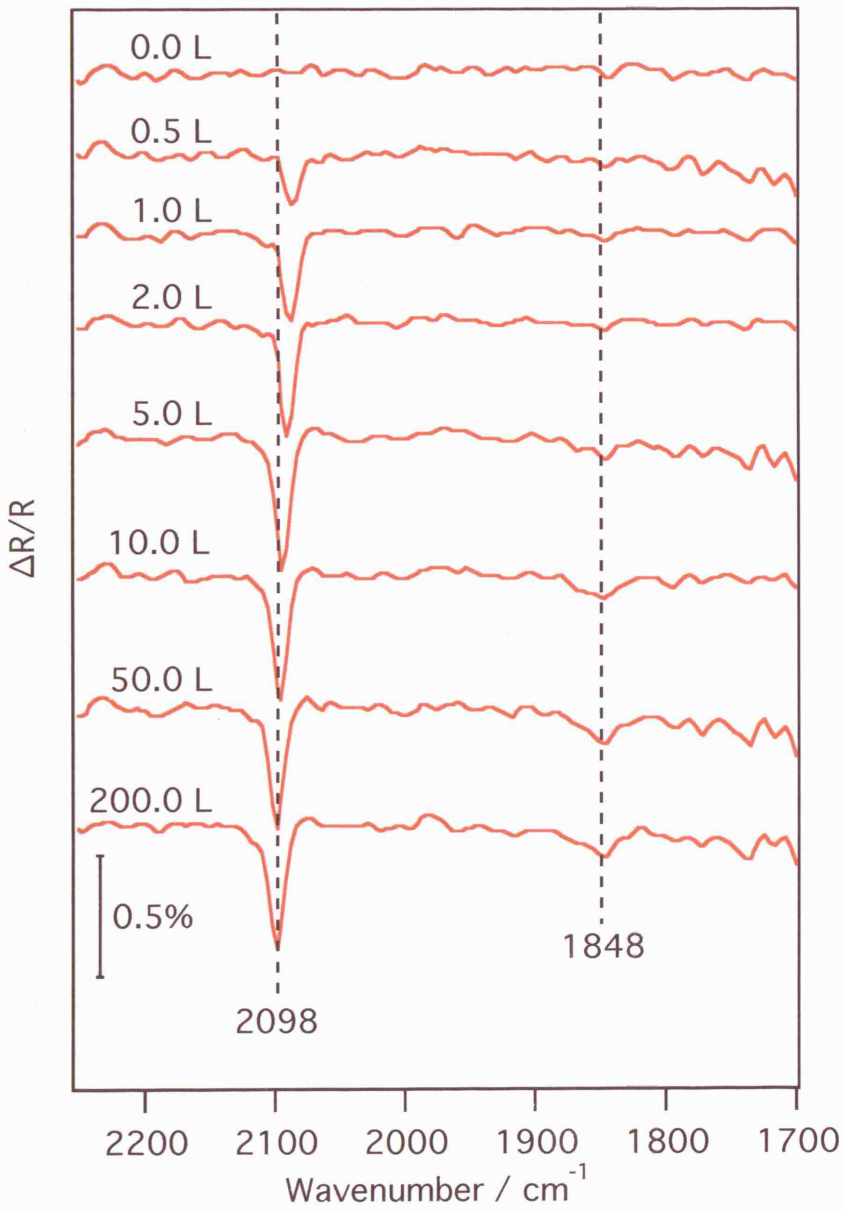

Figure 5.3 RAIR spectra of CO adsorbed on CeO_{2-x}/ Pt(111) at 300 K.

The initial 0.5 L dose of CO onto the CeO_{2-x}(111)/Pt(111) surface gives rise to a peak attributed to the CO-Pt(111) atop stretch mode [31], at a frequency of 2087 cm^{-1} (Figure 5.3). As increasing amounts of CO are dosed onto the sample the peak position shifts to higher frequencies, due to dipole coupling, and the area under the peak increases, as shown in Figure 5.4 and Figure 5.5. After 20 L of CO has been dosed onto the surface the frequency of the peak remains at 2098 cm^{-1} and the area under the peak also remains constant, suggesting that the amount of CO on the surface has saturated at this point. A second peak, attributed to the CO-Pt(111) bridge mode, appears after 1 L of CO has been dosed (Figure 5.3). The frequency of this peak remains constant at 1848 cm^{-1}, independent of the amount of CO dosed. The area under this peak increases at a similar rate to the area under the atop peak (Figure 5.5), and reaches a maximum before plateauing at 20 L. This confirms the previous suggestion that the amount of CO on the surface saturates after a dose of 20 L.

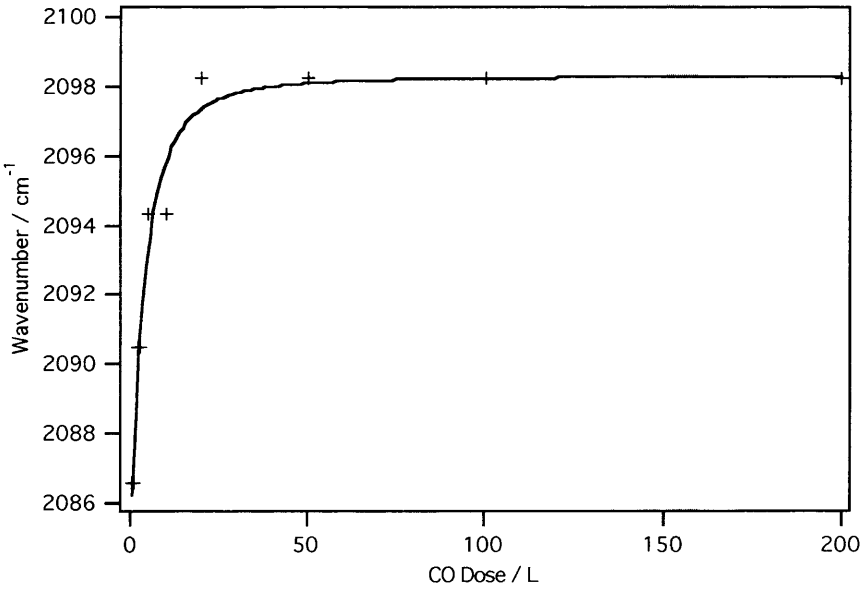

Figure 5.4 Frequency of the CO-Pt atop peak seen in Figure 5.3, as increasing amounts of CO were dosed onto the surface at 300 K.

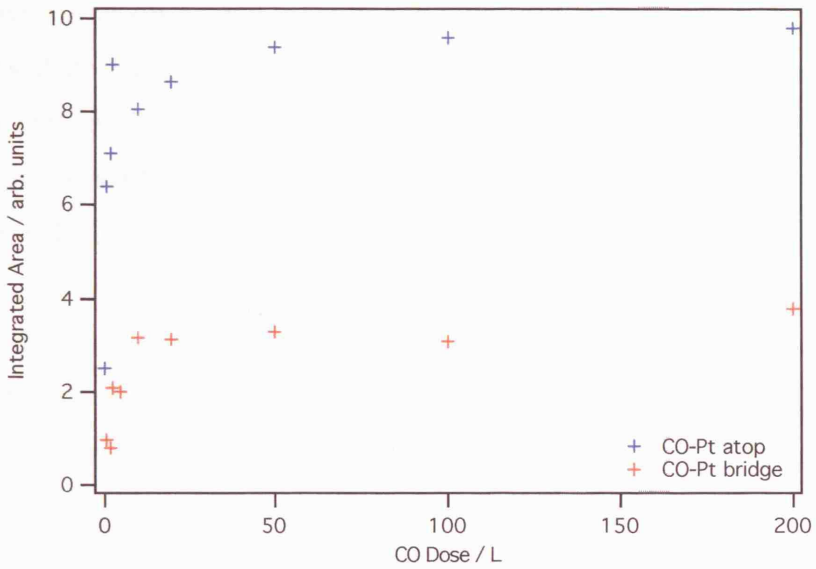

Figure 5.5 Integrated area of the two CO-Pt peaks seen in the RAIR spectra, shown in Figure 5.3, as increasing amounts of CO were dosed onto the sample surface at 300 K.

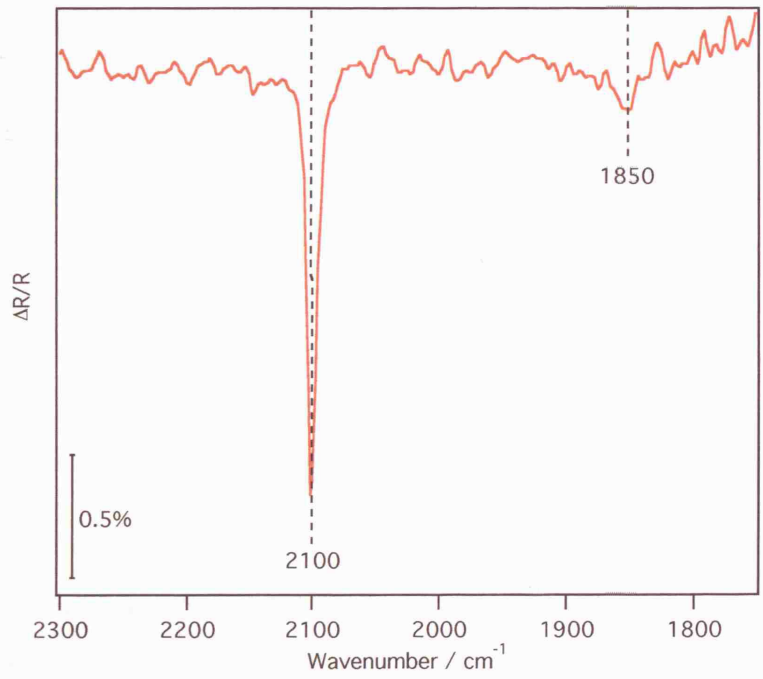

Figure 5.6 RAIR spectra following a 50 L CO exposure onto Pt(111) at 300 K. This spectrum is the result of 256 scans, taken at a resolution of 4 cm^{-1}.

The frequencies observed for the CO-Pt peaks on the CeO_{2-x}/Pt(111) surface only vary by 2 cm^{-1} from those observed for CO adsorption on the clean Pt(111) surface (Figure 5.6). The CO/Pt(111) system has been studied extensively in the past using RAIRS [4, 31-33], and the reported CO-Pt(111) stretch frequencies are in good agreement with those observed in this study.

Comparison of the area under the CO-Pt(111) atop peak for RAIR spectra of CO saturation on clean Pt(111) (Figure 5.6) and on CeO_{2-x}/Pt(111) (not shown) shows that the sample with the ceria overlayer has 17 ± 2% of its surface as bare Pt(111) sites. This is deduced from the fact that the CO peak on the CeO_{2-x}/Pt(111) surface is 17% of the size of the CO peak on the clean Pt(111) surface, and assumes that the presence of the CeO_{2-x} on the surface does not affect the CO-Pt vibrations. Note that the data used for this calculation is taken from spectra which consisted of 256 scans at a resolution of 4 cm^{-1}, as shown in Figure 5.6. The CO absorption spectra for the CeO_{2-x}/Pt(111) surface, shown in Figure 5.3, taken at a resolution of 8 cm^{-1}, could not be used to compare with the CO/Pt(111) data (Figure 5.6) as the two sets of spectra were taken at different resolutions.

CO adsorption onto CeO_{2-x}/Pt(111) samples has been previously studied using RAIRS [15]. In this previous study, CeO_{2-x} films were formed on a clean Pt(111) surface, and it was found that the ceria formed islands leaving uncoated Pt sites to which the CO adsorbed. A strong vibrational band for the CO stretch mode was observed at 2084 cm^{-1}. This is in good agreement with the observations made here, and confirms the assignments given above.

CO adsorption on 1 MLE Pd/CeO_{2-x}(111)/Pt(111)

Figure 5.7 shows RAIR spectra of the 1 MLE Pd/CeO_{2-x}(111)/Pt(111) sample after a succession of CO doses at room temperature. No vibrational bands were observed until 2 L of CO had been dosed, when three bands were seen. The peak attributed to the CO-Pt(111) atop band, as seen for CO adsorption on the CeO_{2-x}/Pt(111) surface, is observed at 2087 cm^{-1}, after the 2 L CO dose. As increasing amounts of CO are dosed onto the surface this peak shifts to higher

frequencies, reaching a maximum intensity, and frequency of 2098 cm^{-1}, after 20 L CO has been dosed. The growth pattern of the CO-Pt(111) atop peak on this surface is very similar to that observed on the CeO_{2-x}/Pt(111) surface. This suggests that the presence of the palladium has had no significant effect on the adsorption of CO onto Pt(111) sites. However, the CO-Pt(111) atop peak intensity at CO saturation on the 1 MLE Pd/CeO_{2-x}/Pt(111) surface (Figure 5.7) is 48 ± 3% smaller than that observed in Figure 5.3 for CO saturation on the CeO_{2-x}/Pt(111) surface. This suggests that the deposited Pd has formed on top of the previously bare Pt(111) sites, hence reducing the amount of Pt atoms available for CO bonding by approximately 48%. It has previously been shown that Pd exhibits a layer-by-layer growth pattern when deposited on Pt(111) [30], hence if the Pd was only present on top of the Pt no CO-Pt(111) peaks would be observed, as there would be no bare Pt surface sites remaining. It has already been shown that only 17 ± 2% of the CeO_{2-x}/Pt(111) surface is bare Pt, and hence the 48% reduction in the CO-Pt(111) atop peak suggests that there will now only be 9 ± 1% bare Pt surface sites present on the surface. This observation also implies that a maximum of 9 ± 1% of the Pd has been deposited onto the bare Pt sites, assuming that the Pd is growing on the Pt(111) according to the layer-by-layer growth model [30]. Therefore, it can be deduced that approximately 90% of the Pd is deposited on top of the CeO_{2-x}.

The peak attributed to the CO-Pt(111) bridge species is present at 1848 cm^{-1} (Figure 5.7) and remains at this frequency as increasing amounts of CO are dosed into the chamber. Unlike the atop peak, the bridge peak does not reach a maximum intensity after 20 L of CO have been dosed. This could suggest that CO saturation is not reached until a larger amount of CO has been dosed. However this peak does appear to overlap slightly with the third vibrational band (1921 cm^{-1}) observed for higher CO doses, which could be contributing to the area under the bridge peak.

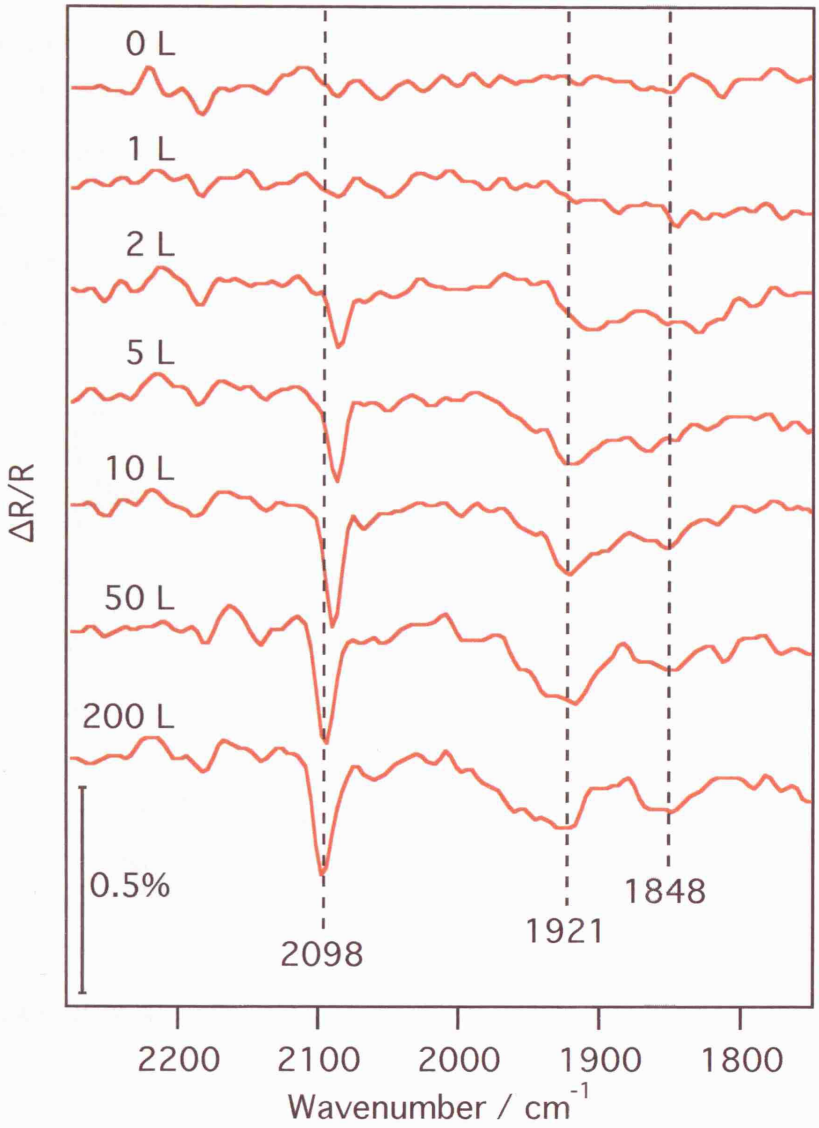

Figure 5.7 RAIR spectra of 1 MLE Pd / CeO_{2-x}/Pt(111) as CO was dosed onto the sample at 300 K.

The third vibrational band, which was not present in the RAIR spectra of CO on the CeO_{2-x}/Pt(111) surface (Figure 5.3), appears at a frequency of 1905 cm^{-1}, after 2 L CO has been dosed. It shifts up in frequency to 1921 cm^{-1} and develops a higher frequency shoulder after 5 L CO has been dosed. As increasing amounts of CO are dosed onto the surface, the peak broadens significantly in the high frequency direction and becomes asymmetric in shape. This suggests that more than one species is contributing to this band. Due to the absence of this vibrational band in RAIR spectra of CO on the CeO_{2-x}/Pt(111) surface it can be

deduced that it is due to the adsorption of CO on the Pd. Possible adsorption sites of CO on Pd are shown in Figure 5.8. It has previously been shown that CO-Pd(111) threefold hollow and CO-Pd(100) bridge species give rise to bands in this frequency region [34, 35]. However, as only a single broad CO-Pd peak is observed it is impossible to tell from RAIRS data alone whether Pd(111) and/or (100) faces are present, or if a defect rich or polycrystalline Pd surface is present.

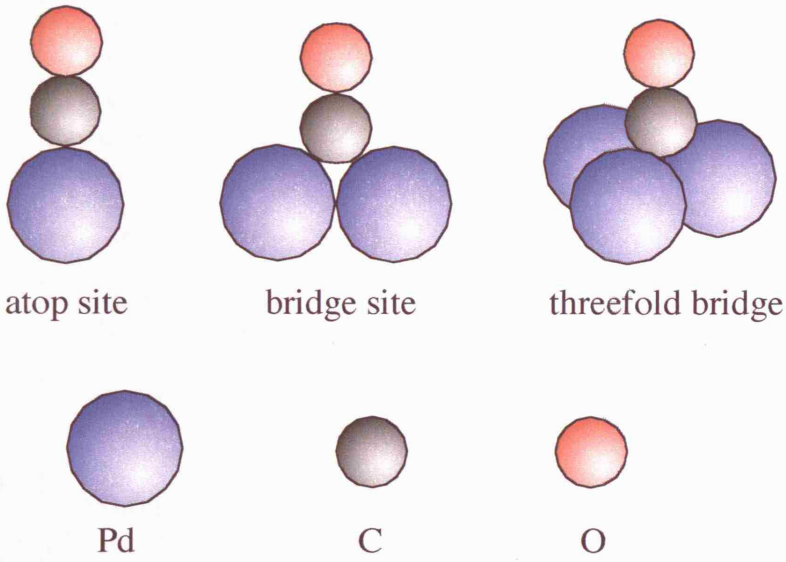

Figure 5.8 Different adsorption sites of CO on Pd.

CO adsorption on 5 MLE Pd/CeO_{2-x}(111)/Pt(111)

After 0.5 L of CO has been dosed into the chamber two vibrational bands are visible in the RAIR spectra at 1817 cm^{-1} and 1890 cm^{-1} (Figure 5.9). The 1817 cm^{-1} band initially increases in intensity and frequency as increasing amounts of CO are dosed onto the surface. However, after 1 L of CO has been dosed the peak broadens and a possible second peak can be observed at 1844 cm^{-1}. After 3 L of CO has been dosed this peak is observed at a frequency of 1848 cm^{-1} and overlaps with the band that was originally observed at 1890 cm^{-1}. By the time 5 L of CO has been dosed the two peaks have merged to form a very broad band. After the 10 L CO dose the lower frequency band is no longer observed, and only a single band remains at 1925 cm^{-1}. After 50 L of CO has been dosed the frequency of this band is 1932 cm^{-1} and a second peak has

developed at 1967 cm^{-1}, overlapping the initial band. This peak also increases in intensity as the amount of CO dosed is increased, and is observed at 1979 cm^{-1} after 200 L CO has been dosed. This spectrum also shows a small band at 2087 cm^{-1}, which has previously been attributed to the CO/Pt(111) atop stretching frequency, and will be discussed in more detail later.

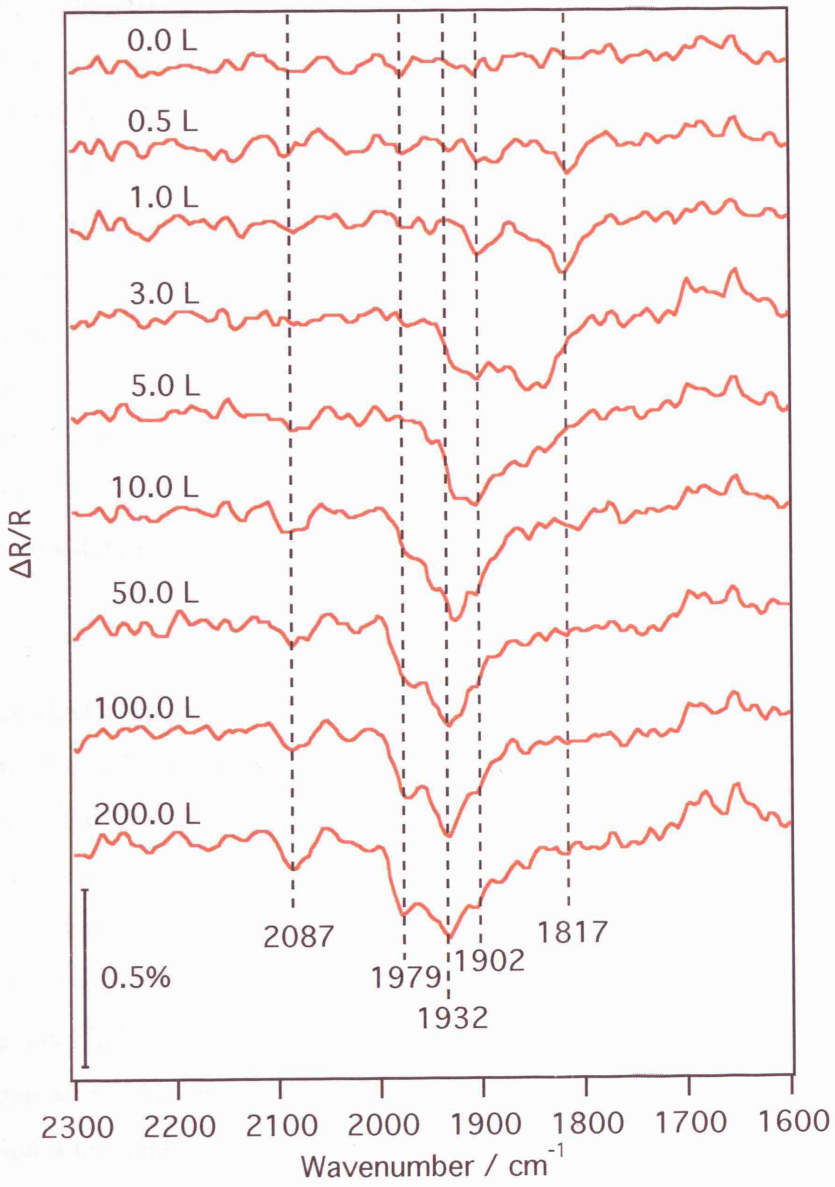

Figure 5.9 RAIR spectra of 5 MLE $Pd/CeO_{2-x}/Pd(111)$ as CO is dosed into the chamber at 300 K.

In order to assign the observed vibrational bands, previous studies of the adsorption of CO on Pd single crystal surfaces have been considered in addition to studies of the adsorption of CO on Pd cluster/metal-oxide systems. It might be expected that ceria affects the reactivity of Pd, hence leading to the observation of different vibrational frequencies for CO adsorption on Pd/CeO_{2-x} compared to CO adsorbed on Pd single crystal surfaces. Indeed, ceria has been shown to alter the catalytic reactivity of dispersed Au through stabilisation of $Au^{\delta+}$ [36, 37]. However, as yet there has been no evidence to suggest that any electronic effects are observed for CO in the $Pd/CeO_{2-x}/Pt(111)$ system. Hence, given the lack of previous data for this system, we have assigned the observed vibrational modes for CO adsorption on $Pd/CeO_{2-x}/Pt(111)$ by comparison with CO frequencies observed on single crystals. Note that vibrational frequencies can only be used as a guide to site assignments as previous studies have shown [35] that assignments based on vibrational frequencies alone are not always correct. Indeed, as discussed later, this has been shown to be the case for the CO/Pd(111) system [34]. Keeping this in mind, the CO/Pd(111)and CO/Pd(100) systems will now be considered in more detail in order to assign the peaks observed in Figure 5.9.

Previous RAIR spectra of CO/Pd(111) [8, 9] show a vibrational band at 1823 cm^{-1} for a CO coverage of 0.08 ML, which develops a higher frequency shoulder as the CO coverage increases. Both bands saturate at 0.33 ML, before disappearing at higher CO coverages. On further increase of the CO coverage a sharper, higher frequency, band starts to develop and reaches a frequency of 1936 cm^{-1} at a coverage of 0.5 ML. Bradshaw *et al.* [8] have used LEED and sticking coefficient calculations in order to assign their observed peaks to adsorption sites. The initial low frequency band has been assigned to threefold adsorption sites, and the higher frequency band, at 1936 cm^{-1}, has been assigned to twofold bridge sites. They speculated that threefold hollow sites are favoured at lower exposures but at higher CO coverages, only twofold bridge sites are occupied due to a higher density of CO molecules on the surface. At very high CO coverages, where RAIR spectra were taken with a CO over-pressure of 1×10^{-6} mbar, an additional peak was observed at 2092 cm^{-1}, which has been

assigned to the CO-Pd(111) atop stretch [8]. The situation on the Pd(100) single crystal surface is considerably less complicated. The CO-Pd(100) bridge stretching frequency is 1895 cm^{-1} at very low CO coverages, and increases in frequency at a constant rate to 1997 cm^{-1} at high coverages [8, 9].

More recently photoelectron diffraction (PED) studies have been carried out which have disagreed with the previous site assignments made using vibrational spectroscopy [35]. Gießel et al. [34] used PED to show that at a CO coverage of 0.5 ML, corresponding to a c(4×2) surface structure, CO is bonded in threefold hollow sites, not in bridge sites as originally assigned by Bradshaw *et al.* [8]. PED studies have also shown that a frequency change of tens of wavenumbers does not always indicate a change in adsorption site, but that this frequency shift can be due to increased dipole coupling or due to chemical effects [35]. Hence the 1936 cm^{-1} band observed by Bradshaw *et al.* [8] for CO adsorbed on Pd(111) must now be assigned as a CO-Pd(111) threefold band. The peak assignments for lower frequency bands, assigned to CO adsorbed on Pd(111) threefold hollow sites, and higher frequency bands, which were assigned to CO adsorbed on Pd(111) atop sites, remain.

The observations of Bradshaw *et al.* [8] are in agreement with the spectra shown in Figure 5.9 and, combined with PED studies [34], can be used to assign peaks observed in this study. Hence, the 1817-1844 cm^{-1} and the 1932 cm^{-1} bands are assigned to CO adsorbed on Pd(111) threefold hollow sites. A further band is observed in Figure 5.9 at 1979 cm^{-1}, which can be assigned to the adsorption of CO in Pd(100) bridge sites [8, 9]. This suggests that the Pd grown on the CeO_{2-x}/Pt(111) forms in islands, predominantly of Pd(111) character, with Pd(100) facets also present in smaller amounts. Similar observations were made for CO adsorption on $Pd/Al_2O_3/NiAl(110)$ [23, 24]. RAIR spectra taken following CO dosing at 90 K showed two species at 1930-1970 cm^{-1} and 1970-2000 cm^{-1} [23, 24], however these peaks were assigned to CO-Pd(111) bridge bonded species on terraces (1930-1970 cm^{-1}), and bridge bonded species on the edges of Pd aggregates (1970-2000 cm^{-1}).

Ozensoy and Goodman [3] also observed a band at 1970-2000 cm^{-1} in experiments on $Pd/Al_2O_3/Ta(110)$. They associated this band with CO-Pd(100) bridge species. This view is consistent with STM studies of the $Pd/Al_2O_3/NiAl(110)$ surface, which confirm that Pd clusters grown at 300 K form with a cubo-octahedral symmetry with both (111) and (100) facets [21]. The (100) sites are found on the sides of the Pd islands, with the top surface having a (111) arrangement. If the Pd islands in this study grow as observed in the STM study [21], then this would explain the relatively small intensity of the CO-Pd(100) bridge band observed in Figure 5.9 as the RAIRS peak intensity would be expected to be smaller than for a perpendicularly orientated species. In the Pd/Al_2O_3 studies [3, 23, 24] a CO-Pd(111) atop peak at 2100 cm^{-1} has also been observed for high coverages of CO, however this species desorbs between 300-350 K and so may not be observed in the study described here.

A further, very small, vibrational band is also observed on the 5 MLE $Pd/CeO_{2-x}/Pt(111)$ surface, as shown in Figure 5.9. This band is not present until 5 L of CO has been dosed and is observed at a frequency of 2079 cm^{-1}. This band increases in frequency and intensity until 10 L CO has been dosed, and then remains at 2087 cm^{-1}, and of constant area, as more CO is dosed into the chamber. This peak could be attributed to the CO-Pt(111) atop band, as previously observed on the $CeO_{2-x}/Pt(111)$ and 1 MLE $Pd/CeO_{2-x}/Pt(111)$ surfaces. However, the peak is also within the appropriate frequency range to be attributed to the CO-Pd(111) or (100) atop bands [9, 31]. This peak is assigned to a CO-Pt(111) atop band. This peak assignment is possible as CO-Pt and CO-Pd atop species have different desorption temperatures, thus allowing a definitive peak identification. This is discussed in detail later.

CO adsorption on 10 MLE $Pd/CeO_{2-x}(111)/Pt(111)$

The sequential dosing of CO onto the 10 MLE $Pd/CeO_{2-x}(111)/Pt(111)$ surface is shown in Figure 5.10.

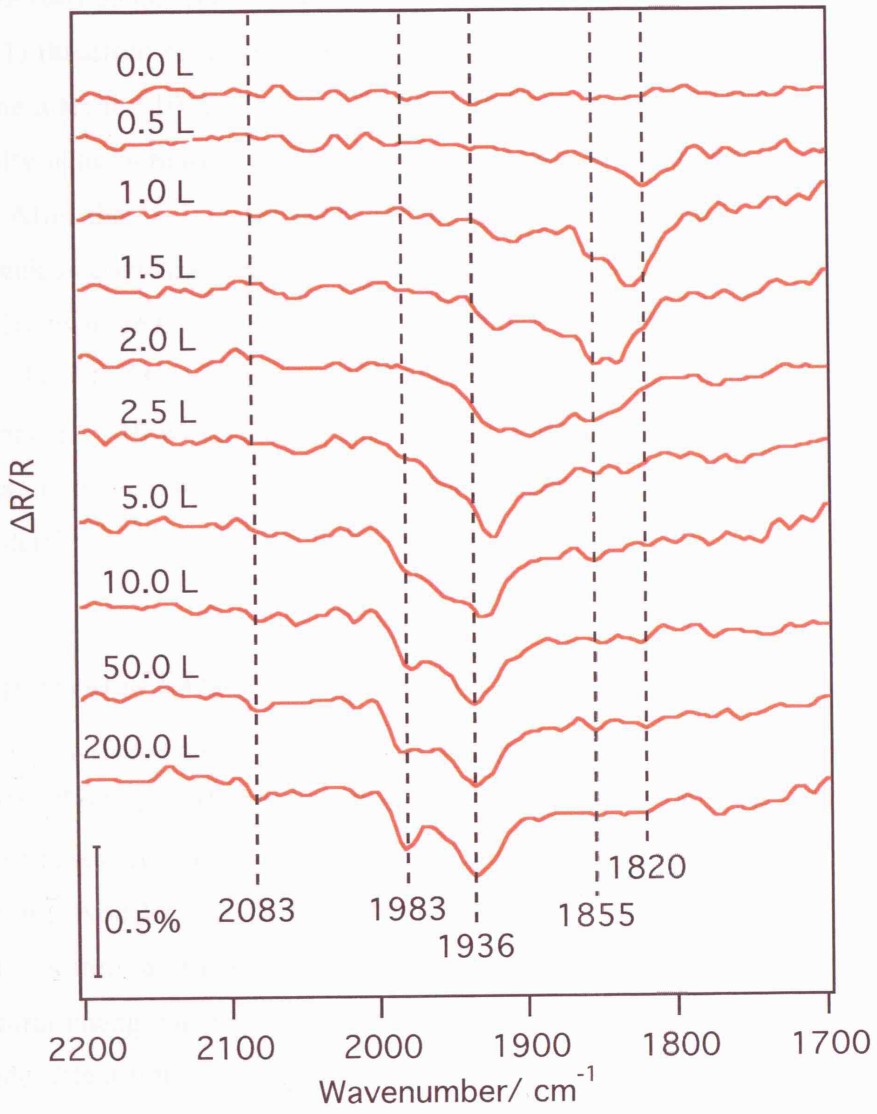

Figure 5.10 RAIR spectra of 10 MLE Pd /CeO_{2-x}/Pd(111) as CO is dosed into the chamber at 300 K.

The first vibrational band to appear in Figure 5.10 is the CO-Pd(111) threefold stretch at 1820 cm^{-1}, which is observed after 0.5 L CO had been dosed into the chamber. After 1 L CO had been dosed the threefold peak increases in intensity and frequency, and a high frequency shoulder appears at 1855 cm^{-1}. A further CO-Pd(111) threefold hollow band is also now present at 1909 cm^{-1}. After the 2 L dose the three peaks originally observed have now formed one very broad peak. After 2.5 L CO has been dosed the lower frequency bands are no longer present, and a sharper, high frequency, CO-Pd(111) threefold peak remains, now with a slight broadening to higher frequencies, suggesting the presence of the

CO-Pd(100) band. As increasing amounts of CO are dosed the remaining CO-Pd(111) threefold band increases in frequency to 1936 cm^{-1}, where it appears to saturate after the 10 L CO dose. The CO-Pd(100) bridge band also increases in intensity with increasing CO dose, with its frequency remaining constant at 1983 cm^{-1}. After the 10 L CO dose a band is present at 2083 cm^{-1}. The intensity of this peak is comparatively very small and appears not to alter in frequency or intensity as more CO is dosed into the chamber. This peak could be assigned to either the CO-Pt(111) atop or CO-Pd(111) atop bands, as they have similar frequencies. However, these bands have significantly different desorption temperatures, which can be used for peak assignment. This will be discussed in more detail later.

Comparison of CO saturated Pd/CeO_{2-x}/Pt(111) surfaces

Figure 5.11 shows a comparison of RAIR spectra for CO saturation on surfaces of CeO_{2-x}/Pt(111) with varying amounts of Pd dosed on top. The RAIR spectra for CO adsorbed on the 5 MLE Pd/CeO_{2-x}/Pt(111) surface are very similar to those observed for the 10 MLE Pd surface, suggesting that the structure of Pd islands is similar in both cases. However, there is a much more dramatic structural change occurring between the 1 and 5 MLE Pd coverage as there is a considerable difference in the CO-Pd peak shape, as shown in Figure 5.11.

It can clearly be seen that the main difference between the CO saturated 5 and 10 MLE Pd surfaces is the intensity of the peak attributed to the CO-Pt(111) atop band, at 2087-2098 cm^{-1}. By studying the CO-Pt(111) atop peak in more detail, additional information can be learnt about the overall morphology of the surface. The frequency of the CO-Pt(111) atop band decreases by 11 cm^{-1} for the 5 ML Pd coverage, compared to the 0 and 1 MLE Pd coverages (Figure 5.11). This decrease in frequency can be ascribed to smaller amounts of CO on the Pt sites, which is confirmed by the decrease in intensity of the peak. The decreased amount of CO on the Pt sites can in turn be explained by the increased amount of Pd on the surface, a small amount of which bonds to the Pt sites. However, as described earlier, it is thought that the majority of the Pd dosed is deposited on the CeO_{2-x} surface. This observation is reinforced by the fact that between the 1

and 5 MLE coverages of Pd the area under the CO-Pt(111) atop peak decreases by approximately 50%, whereas the area under the CO-Pd peaks increases by over 300%. The area under the CO-Pd peaks is hence increasing at a faster rate than the CO-Pt peak is decreasing, suggesting that the majority of the Pd is adsorbing onto the CeO_{2-x} surface.

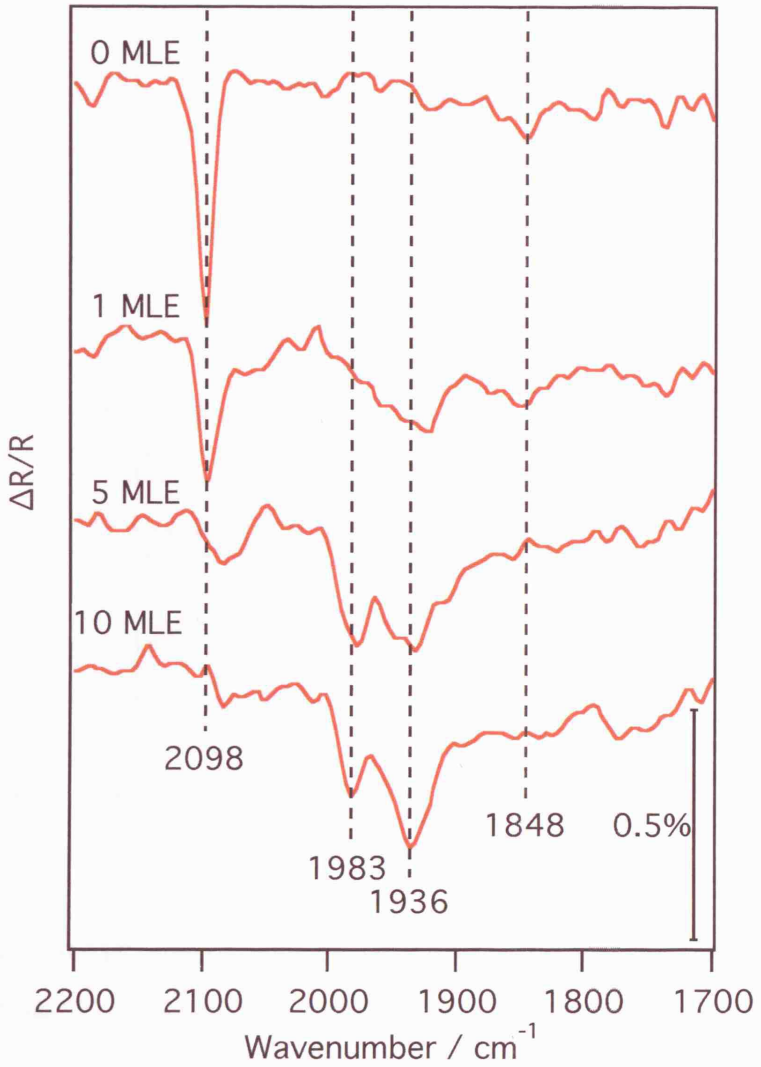

Figure 5.11 RAIR spectra of CO saturated surfaces of CeO_{2-x}/Pt(111) with increasing amounts of Pd dosed onto them. All spectra were taken at room temperature.

CO desorption

CO desorption from CeO_{2-x}(111)/Pt(111)

RAIR spectra taken after CO saturation of the CeO_{2-x}/Pt(111) surface, at increasing temperatures, are shown in Figure 5.12.

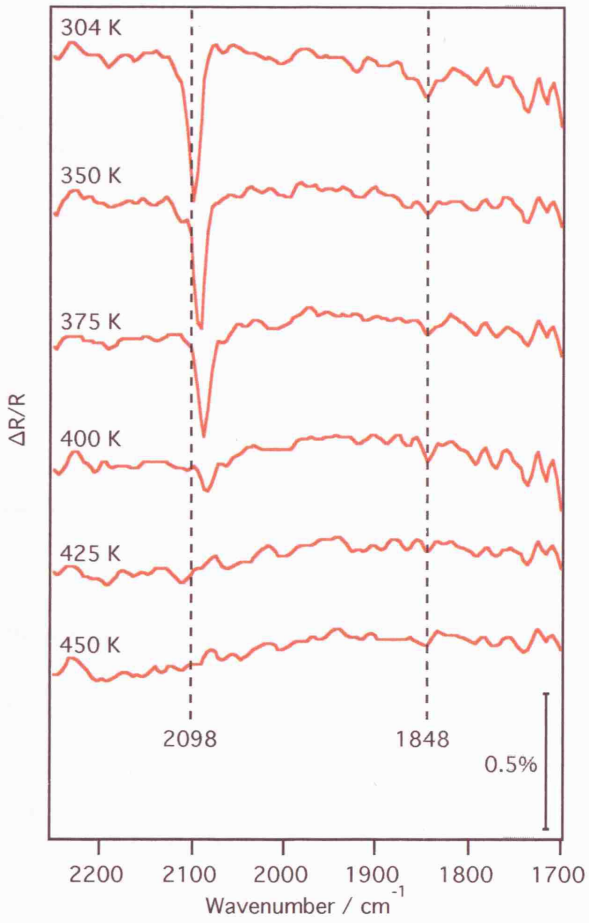

Figure 5.12 RAIR spectra of CO desorbing from a CeO_{2-x}/Pt(111) surface during heating.

RAIR spectra taken whilst the sample was heated show that both the CO-Pt(111) atop and bridge peaks disappear between 400-425 K (Figure 5.12). The frequency of the CO-Pt(111) atop peak decreases linearly from 2098 cm^{-1}, at room temperature, to 2083 cm^{-1} at 400 K, as shown in Figure 5.13. This reduction in frequency occurs due to the reduced dipole coupling that occurs as the CO desorbs. As expected, the area under both peaks decreases as the sample is heated indicating that the CO is desorbing. The desorption temperature of CO

on Pt(111) has previously been determined to be between 420-470 K, depending on the CO coverage, with a heating rate of 15 K/sec [38]. Allowing for the difference in heating rate between the two experiments this is in good agreement with the desorption temperature found in this study, and hence shows that the presence of the CeO_{2-x} has had no significant effect on the desorption temperature of CO adsorbed on Pt(111).

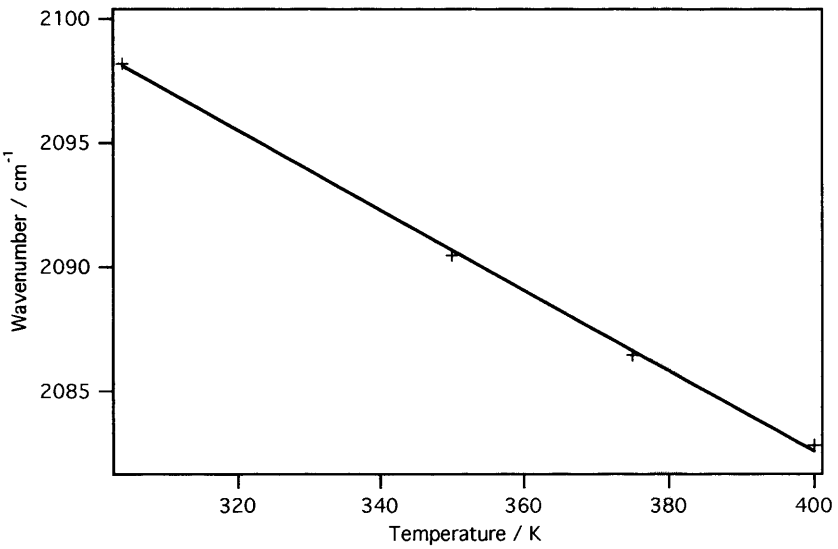

Figure 5.13 Frequency of the Pt-CO atop peak as the CeO_{2-x}/Pt(111) sample was heated.

CO desorption from 1 MLE Pd/CeO_{2-x}(111)/Pt(111)

RAIR spectra taken whilst the sample was heated show that all peaks disappear between 400-425 K (Figure 5.14). The frequency of the CO-Pt(111) atop peak decreases linearly from 2098 cm^{-1} at room temperature to 2083 cm^{-1} at 400 K. The desorption of the CO-Pt(111) atop peak exhibits identical behaviour to that observed for the CeO_{2-x}/Pt(111) system, which shows that the presence of Pd particles on the surface has not affected the CO-Pt(111) desorption temperature. The frequency of the CO-Pd peak decreases from 1929 cm^{-1} at room temperature to 1905 cm^{-1} at 400 K. The high frequency shoulder which is present initially has disappeared by 375 K, before the main bulk of the peak. The CO-Pd peak disappears from the spectrum by 425 K, which is slightly lower than the desorption temperature of CO on bulk Pd(111) found by TPD experiments [39].

The desorption temperature in these TPD experiments was found to be between 450-500 K, when the CO was adsorbed onto the surface at 200 K, with a heating rate of 2 K/s.

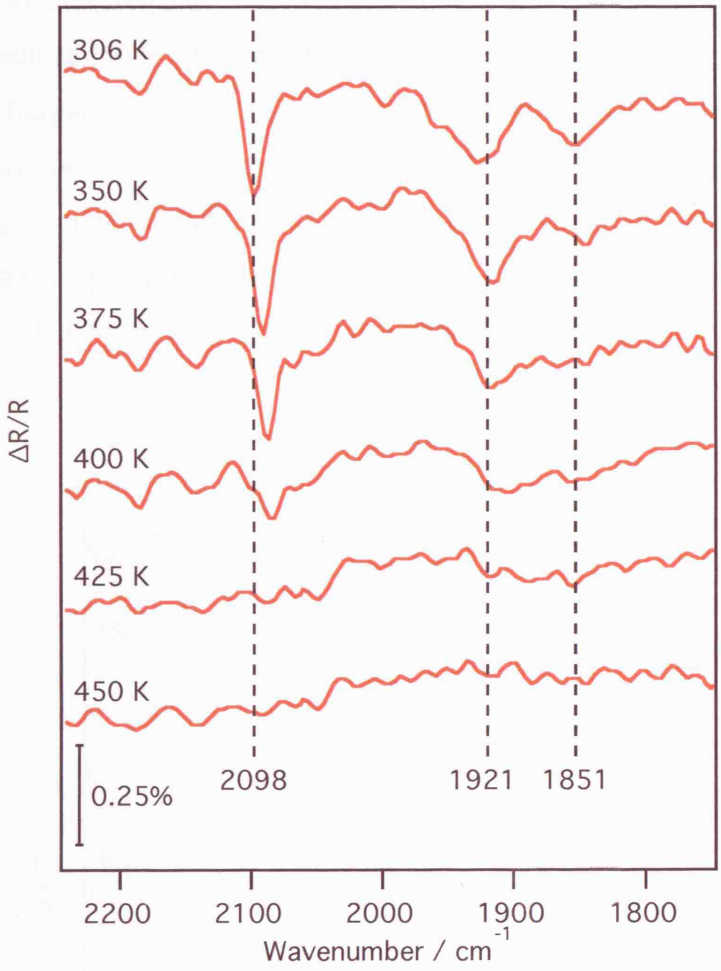

Figure 5.14 RAIR spectra of CO desorbing from a 1 MLE $Pd/CeO_{2-x}/Pt(111)$ surface during heating.

CO desorption from 5 MLE $Pd/CeO_{2-x}(111)/Pt(111)$

RAIR spectra taken whilst the sample was being heated (Figure 5.15) show that the first species to desorb is the 1971 cm^{-1} band, assigned to the CO-Pd(100) bridge species. The majority of this species has desorbed by 350 K, leaving a peak of relatively small intensity, which has completely desorbed by 400 K. This low desorption temperature suggests that the CO-Pd(100) is weakly bonded compared to the CO-Pd(111). The 1932 cm^{-1} CO-Pd(111) threefold hollow band

decreases in intensity and frequency as the sample is heated, shifting in frequency by 42 cm^{-1} before desorbing completely between 425-450 K. At 375 K a low frequency shoulder can be seen developing on this band. As the sample is heated this shoulder moves to lower frequencies, until it appears as a separate peak at a frequency of 1817 cm^{-1} at 425 K. The vibrational band is no longer present at 450 K. This band is appearing in the same range of frequencies as the low frequency CO-Pd(111) threefold band in the adsorption study on the same surface for low CO coverages (Figure 5.9). The presence of this threefold band at higher temperatures could be due to lower coverages of CO on the Pd [8]. Alternatively heating the sample may have led to changes in the surface morphology that has in turn led to the re-introduction of this threefold band.

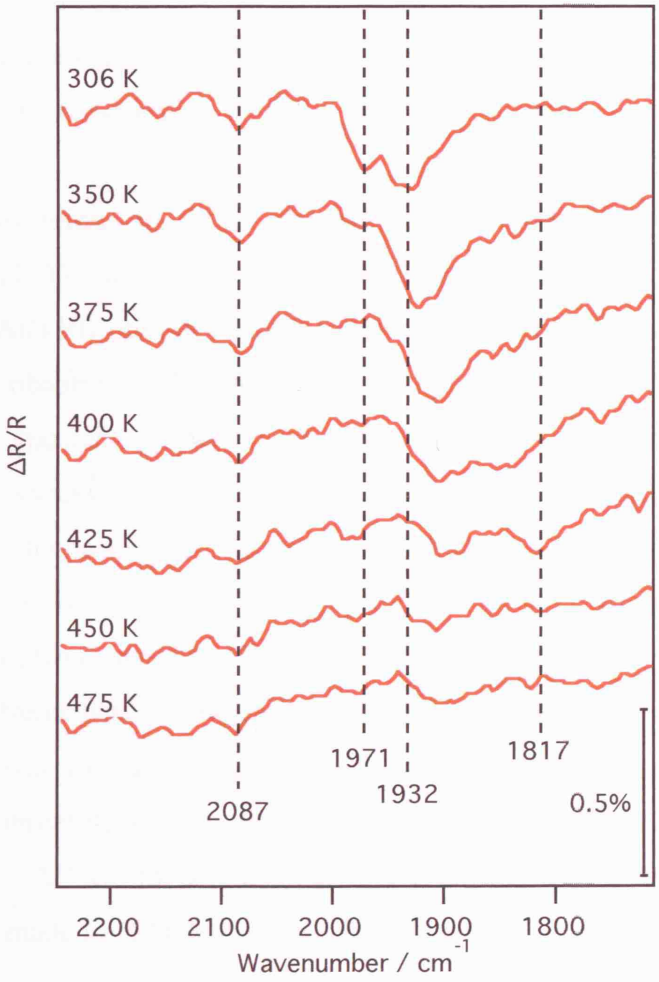

Figure 5.15 RAIR spectra showing the desorption of CO from the 5 MLE $Pd/CeO_{2-x}/Pt(111)$ surface as it was heated.

The 2087 cm^{-1} band remains at a constant frequency during heating and has desorbed by 425 K. This peak could be attributed to the CO-Pt(111) atop band, as previously observed on the CeO_{2-x}/Pt(111) and 1 MLE Pd/CeO_{2-x}/Pt(111) surfaces. However, the peak is also within the correct frequency range to be attributed to the CO-Pd(111) or (100) atop band [8, 9, 34], allowing for a shift in frequency due to reduced dipole coupling. The CO-Pt and CO-Pd atop species have different desorption temperatures, so this information has been used to give a definitive peak identification. The 2087 cm^{-1} band has the same desorption temperature as observed for the CO-Pt(111) atop species on the 0 MLE and 1 MLE Pd/CeO_{2-x}/Pt(111) surface, which also agrees with TPD studies of CO on Pt(111) [38]. This band has hence been assigned as a CO-Pt(111) atop species. Therefore, even though there are very few Pt sites remaining on the surface, the CO-Pt desorption characteristics have not been altered by the presence of large quantities of other species.

Similar observations to those seen when desorbing CO from the 5 MLE Pd/CeO_{2-x}/Pt(111) surface, have been made by Wolter *et al.* when heating a Pd/Al_2O_3/NiAl(110) sample which had been dosed with CO at 300 K [24]. At 300 K they observed a broad peak at 1948 cm^{-1}, which was assigned to a CO-Pd(111) species. However, it was noted that some contribution from CO-Pd(100) species could also be present making this peak broader than expected. As the sample was heated this peak shifted to lower frequencies and it's width decreased, due to the desorption of CO-Pd(100) species. A slight shoulder was also observed to lower frequencies on the 1948 cm^{-1} peak, which decreases in frequency and increases in intensity as the sample is heated. At 445 K, this peak was seen at a frequency of 1830 cm^{-1}, and has been assigned to the CO-Pd(111) threefold stretch. Both the CO-Pd(111) peaks disappeared between 445-480 K. All of these observations are in good agreement with the observations made for CO desorption from the 5 MLE Pd/CeO_{2-x}/Pt(111) surface (Figure 5.15).

CO desorption from 10 MLE $Pd/CeO_{2-x}(111)/Pt(111)$

The CO desorption sequence from the 10 MLE $Pd/CeO_{2-x}/Pd(111)$ surface is shown in Figure 5.16. On first comparison there appear to be very few differences between this and the CO desorption from the 5 MLE $Pd/CeO_{2-x}/Pd(111)$ surface (Figure 5.15). RAIR spectra taken whilst the 10 MLE $Pd/CeO_{2-x}/Pt(111)$ sample was being heated show that the first species to desorb are those that give rise to the 2083 cm^{-1} and 1983 cm^{-1} bands, which have disappeared by 350 K. By solely considering peak frequencies, the 2083 cm^{-1} band could be attributed to either CO-Pt or CO-Pd atop species. However due to the difference in desorption temperatures for the two species accurate peak assignment can be made, as seen for CO desorption from the 5 MLE $Pd/CeO_{2-x}/Pd(111)$ surface. The highest temperature at which Ozensoy and Goodman [3] have observed CO-Pd(111) atop species, using RAIRS, is 350 K. However, TPD experiments have shown that the desorption temperature of CO from Pt(111) is between 420-470 K, depending on CO coverage, with a heating rate of 15 K/s [38]. This suggests that the 1983 cm^{-1} band on the 10 MLE $Pd/CeO_{2-x}/Pt(111)$ surface is a CO-Pd(111) atop species, which in turn would indicate that there are no longer any bare Pt sites on the surface. In contrast, the 1983 cm^{-1} band on the 5 MLE $Pd/CeO_{2-x}/Pt(111)$ surface disappears between 425-450 K, which suggests that it is a CO-Pt(111) atop band.

The CO-Pd(100) bridge stretch at 1983 cm^{-1} has also disappeared by 350 K on the 10 MLE $Pd/CeO_{2-x}/Pt(111)$ surface (Figure 5.16), as observed on the 5 MLE $Pd/CeO_{2-x}/Pd(111)$ surface. The CO-Pd(111) threefold band decreases in intensity as the sample temperature is increased and starts to form a low frequency shoulder at 350 K. As the temperature is increased further, the lower frequency component increases in intensity as the higher frequency component decreases. At 400 K there is a broad peak from 1836-1905 cm^{-1}. This peak has decreased in intensity by 425 K, and has completely disappeared by 450 K. TPD experiments have given a CO-Pd(111) desorption temperature of 450-500 K, when the CO was adsorbed onto the surface at 200 K, with a heating rate of 2 K/s [39]. This is in strong agreement with the temperatures observed here, when

the difference in heating rate is taken into account. Therefore, the Pd(111) facets of the Pd islands are exhibiting behaviour very similar to that of bulk Pd(111).

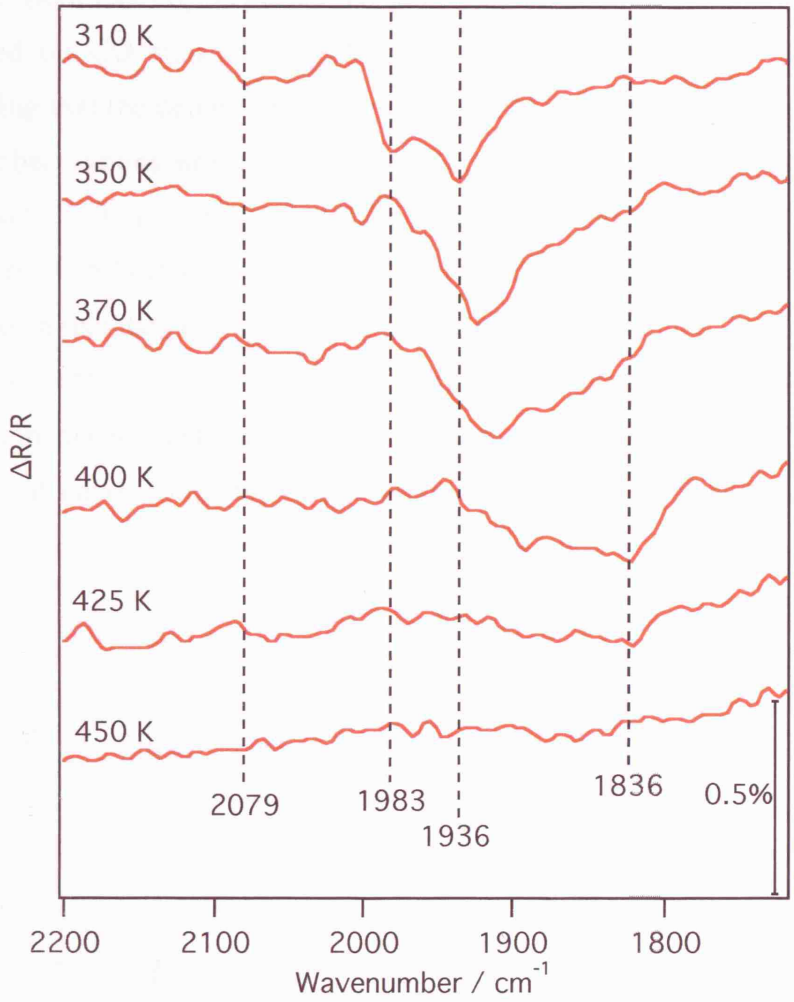

Figure 5.16 RAIR spectra showing the desorption of CO from the 10 MLE $Pd/CeO_{2-x}/Pt(111)$ surface as it was heated.

Conclusion

RAIRS studies of CO adsorbed on $Pd/CeO_{2-x}/Pt(111)$ have been carried out and successfully employed to provide information about the morphology of the surface. Experiments have shown that, following the growth of a 3 MLE $CeO_{2-x}(111)$ overlayer on a Pt(111) single crystal, bare Pt sites remain, suggesting that the CeO_{2-x} has formed in islands. However, when Pd is deposited onto the CeO_{2-x} surface most of the Pd grows directly on top of the CeO_{2-x}, as

opposed to on bare Pt sites. CO adsorption experiments on the 1 MLE $Pd/CeO_{2-x}/Pt(111)$ surface show peaks inconsistent with single crystal Pd formation, suggesting that polycrystalline or defect rich Pd structures have formed. Both CO-Pd(111) threefold hollow and CO-Pd(100) bridge species are observed on CO saturation of 5 and 10 MLE $Pd/CeO_{2-x}/Pt(111)$ surfaces, suggesting that the deposited Pd forms islands, with both (111) and (100) faces. These observations are in agreement with STM studies of Pd deposited on $Al_2O_3/NiAl(110)$ at 300 K, where Pd clusters are observed with cubo-octahedral symmetry with both (111) and (100) facets [21]. CO desorption experiments have shown that the presence of both CeO_{2-x} and Pd on the Pt(111) surface has no significant effect on the binding energy of CO adsorbed on Pt(111). CO desorption experiments also allow definitive assignment of the CO-Pd atop vibrational band, following CO adsorption on a 10 MLE $Pd/CeO_{2-x}/Pt(111)$ surface.

References

1. Heck, R. and Farrauto, R., *Catalytic Air Pollution Control - Commercial Technology*. 1995, New York: Van Nostrand Reinhold.
2. Unterhalt, H., Galletto, P., Morkel, M., Rupprechter, G., and Freund, H.J., *Sum frequency generation study of CO adsorption on palladium model catalysts*. Physica Status Solidi A-Applied Research, 2001. **188**(4): p. 1495.
3. Ozensoy, E. and Goodman, D.W., *Vibrational spectroscopic studies on CO adsorption, NO adsorption CO plus NO reaction on Pd model catalysts*. Phys. Chem. Chem. Phys., 2004. **6**(14): p. 3765.
4. Sheppard, N. and Nguyen, T.T., *Carbon monoxide chemisorbed on the surface of metal catalysts*, in *Advances in Infrared and Raman Spectroscopy*, R.J.H. Clark and R.E. Hester, Editors. 1978, John Wiley and Sons.
5. Bourguignon, B., Carrez, S., Dragnea, B., and Dubost, H., *Vibrational spectroscopy of imperfect CO/Pd(111) surfaces obtained by adsorption between 150 and 230 K*. Surf. Sci., 1998. **418**(1): p. 171.
6. Cook, J.C., Clowes, S.K., and McCash, E.M., *Reflection absorption IR studies of vibrational energy transfer processes and adsorption energetics*. J. Chem. Soc. Faraday Trans., 1997. **93**(13): p. 2315.
7. Fukui, K., Miyauchi, H., and Iwasawa, Y., *CO adsorption and oxidation on Pd(110)-c(2x4)-O by reflection-absorption infrared spectroscopy*. J. Phys. Chem., 1996. **100**(48): p. 18795.
8. Bradshaw, A.M. and Hoffmann, F.M., *Chemisorption of carbon-monoxide on palladium single-crystal surfaces - IR spectroscopic evidence for localized site adsorption*. Surf. Sci., 1978. **72**(3): p. 513.
9. Hoffmann, F.M., *Infrared reflection-absorption spectroscopy of adsorbed molecules*. Surf. Sci. Rep., 1983. **3**(2/3): p. 107.
10. Bozon-Verduraz, F. and Bensalem, A., *IR studies of cerium dioxide: influence of impurities and defects*. J. Chem. Soc. Faraday Trans., 1994. **90**(4): p. 653.

11. Holmgren, A., Bengt, A., and Duprez, D., *Interactions of CO with Pt/ceria catalysis*. App. Catal. B, 1999. **22**: p. 215.
12. Jin, T., Zhou, Y., Mains, G.J., and White, J.M., *Infrared and x-ray photoelectron-spectroscopy study of CO and CO_2 on Pt/CeO_2*. J. Phys. Chem., 1987. **91**(23): p. 5931.
13. Badri, A., Binet, C., and Lavalley, J.C., *Metal-support interaction in Pd/CeO_2 catalysts .2. Ceria textural effects*. J. Chem. Soc. Faraday Trans., 1996. **92**(9): p. 1603.
14. Binet, C., Jadi, A., Lavalley, J.C., and Boutonnetkizling, M., *Metal support interaction in Pd/CeO_2 Catalysts - Fourier-transform infrared studies of the effects of the reduction temperature and metal loading .1. Catalysts prepared by the microemulsion technique*. J. Chem. Soc. Faraday Trans., 1992. **88**(14): p. 2079.
15. Berner, U., Schierbaum, K.-D., Jones, G., Wincott, P., Haq, S., and Thornton, G., *Ultrathin ordered CeO_2 overlayers on Pt(111): interaction with NO_2, NO, H_2O and CO*. Surf. Sci., 2000. **467**: p. 201.
16. Rainer, D.R. and Goodman, D.W., *Metal clusters on ultrathin oxide films: model catalysts for surface science studies*. J. Mol. Catal. A, 1998. **131**(1-3): p. 259.
17. Rainer, D.R., Xu, C., and Goodman, D.W., *Characterization and catalysis studies of small metal particles on planar model oxide supports*. J. Mol. Catal. A, 1997. **119**(1-3): p. 307.
18. Baumer, M. and Freund, H.J., *Metal deposits on well-ordered oxide films*. Prog. Surf. Sci., 1999. **61**(7-8): p. 127.
19. Henry, C.R., *Surface studies of supported model catalysts*. Surf. Sci. Rep., 1998. **31**(7-8): p. 235.
20. Campbell, C.T., *Ultrathin metal films and particles on oxide surfaces: Structural, electronic and chemisorptive properties*. Surf. Sci. Rep., 1997. **27**(1-3): p. 1.
21. Hansen, K.H., Worren, T., Stempel, S., Laegsgaard, E., Baumer, M., Freund, H.J., Besenbacher, F., and Stensgaard, I., *Palladium nanocrystals on Al_2O_3: Structure and adhesion energy*. Phys. Rev. Lett., 1999. **83**(20): p. 4120.

22. Rainer, D.R., Vesecky, S.M., Koranne, M., Oh, W.S., and Goodman, D.W., *The CO+NO reaction over Pd: A combined study using single-crystal, planar-model-supported, and high-surface-area Pd/Al_2O_3 catalysts*. J. Catal., 1997. **167**(1): p. 234.

23. Wolter, K., Seiferth, O., Libuda, J., Kuhlenbeck, H., Baumer, M., and Freund, H.J., *Infrared study of CO adsorption on alumina supported palladium particles*. Surf. Sci., 1998. **404**(1-3): p. 428.

24. Wolter, K., Seiferth, O., Kuhlenbeck, H., Baumer, M., and Freund, H.J., *Infrared spectroscopic investigation of CO adsorbed on Pd aggregates deposited on an alumina model support*. Surf. Sci., 1998. **399**(2-3): p. 190.

25. Unterhalt, H., Rupprechter, G., and Freund, H.J., *Vibrational sum frequency spectroscopy on Pd(111) and supported Pd nanoparticles: CO adsorption from ultrahigh vacuum to atmospheric pressure*. J. Phys. Chem. B, 2002. **106**(2): p. 356.

26. Holmblad, P.M., Rainer, D.R., and Goodman, D.W., *Particle size effects in the acetylene cyclotrimerization on planar model Al2O3 thin film supported Pd clusters*. J. Phys. Chem. B, 1997. **101**(44): p. 8883.

27. Rainer, D.R., Wu, M.C., Mahon, D.I., and Goodman, D.W., *Adsorption of CO on Pd/Al_2O_3/Ta(110) model catalysts*. J. Vac. Sci. Technol. A-Vac. Surf. Films, 1996. **14**(3): p. 1184.

28. Ozensoy, E., Min, B.K., Santra, A.K., and Goodman, D.W., *CO dissociation at elevated pressures on supported Pd nanoclusters*. J. Phys. Chem. B, 2004. **108**(14): p. 4351.

29. Giorgi, J.B., Schroeder, T., Baumer, M., and Freund, H.J., *Study of CO adsorption on crystalline-silica-supported palladium particles*. Surf. Sci., 2002. **498**(1-2): p. L71.

30. Han, M., Mrozek, P., and Wieckowski, A., *X-ray-photoelectron-spectroscopy and auger-electron-spectroscopy study of ultrathin palladium films on a Pt(111) substrate*. Phys. Rev. B, 1993. **48**(11): p. 8329.

31. Chabal, Y.J., *Surface Infrared-Spectroscopy*. Surf. Sci. Rep., 1988. **8**(5-7): p. 211.

32. Tushaus, M., Schweizer, E., Hollins, P., and Bradshaw, A.M., *Yet another vibrational study of the adsorption system Pt{111}-CO.* J. Electron Spectrosc. Relat. Phenom., 1987. **44**: p. 305.

33. Shigeishi, R.A. and King, D.A., *Chemisorption of carbon monoxide on platinum (111): Reflection-Absorption Infrared Spectroscopy.* Surf. Sci., 1976. **58**: p. 379.

34. Giessel, T., Schaff, O., Hirschmugl, C.J., Fernandez, V., Schindler, K.M., Theobald, A., Bao, S., Lindsay, R., Berndt, W., Bradshaw, A.M., Baddeley, C., Lee, A.F., Lambert, R.M., and Woodruff, D.P., *A photoelectron diffraction study of ordered structures in the chemisorption system Pd{111}-CO.* Surf. Sci., 1998. **406**(1-3): p. 90.

35. Sheppard, N. and De La Cruz, C., *The reliability of vibrational spectroscopy as a means of identification of the structures of chemisorbed species on metal surfaces: the cases of CO, NO and C-2 hydrocarbon surface species.* Catalysis Today, 2001. **70**(1-3): p. 3.

36. Fu, Q., Saltsburg, H., and Flytzani-Stephanopoulos, M., *Active nonmetallic Au and Pt species on ceria-based water-gas shift catalysts.* Science, 2003. **301**: p. 935.

37. Liu, Z.-P., Jenkins, S.J., and King, D.A., *Origin and activity of oxidized gold in water-gas-shift catalysis.* Phys. Rev. Lett., 2005. **94**(19): p. 196102.

38. Ertl, G., Neumann, M., and Streit, K.M., *Chemisorption of CO on Pt(111) surface.* Surf. Sci., 1977. **64**(2): p. 393.

39. Guo, X.C. and Yates, J.T., *Dependence of effective desorption kinetic-parameters on surface coverage and adsorption temperature - CO on Pd(111).* J. Chem. Phys., 1989. **90**(11): p. 6761.

Chapter 6 : XPS studies of CO adsorption on $Pd/CeO_{2-x}/Pt(111)$

Introduction

Further to RAIRS studies of CO adsorption on $Pd/CeO_{1.91}/Pt(111)$ (chapter 5) the same surface has also been studied using XPS, the results of which will be described in this chapter. The study of the interaction of model catalyst surfaces with small molecules, such as CO, is of interest in order to gain fundamental understanding of the catalytic process. Due to the ability of cerium dioxide to improve catalytic performance by its ability to store and release oxygen [1, 2], it is of interest to study the change in oxidation state of ceria caused by interaction with Pd and CO. There has been extensive research into the interaction of CO with Rh/CeO_x surfaces [3-8], however there has been very little in the area of Pd/CeO_x and Pt/CeO_x surfaces.

Pfau *et al.* [9] have studied the effects on the valence band structure of dosing Rh onto CeO_2 thin films. It was found that, as Rh is deposited onto the CeO_2 surface, the Ce^{3+} concentration increases. This was thought to be due to Rh-catalysed desorption of surface oxygen and the creation of positively charged oxygen anion vacancies at the surface. Alternatively the increase in Ce^{3+} concentration could also be due to charge transfer from the Rh to the oxide. However it has been argued that this option is unlikely, due to similar work functions of bulk Rh and CeO_2 [9].

A number of model-catalyst investigations into Pd clusters supported on various other metal oxides, such as TiO_2 [10, 11], Al_2O_3 [12, 13], SiO_2 [14], and ZnO [15], have also taken place. CO adsorption experiments on a $Pd/TiO_2(110)$ surface have shown that for Pd coverages above 10 ML, the Pd particles exhibit (111) facets parallel to the substrate. However, for lower Pd coverages, CO-Pd bridge species characteristic of CO adsorption on Pd(110) and (100) facets are observed [10]. For Pd particles supported on stoichiometric $TiO_2(110)$ [11] and polycrystalline ZnO [15] there has been no evidence of Pd oxidation, and it has

been found that stoichiometric $TiO_2(110)$ is not reduced when Pd is dosed onto the sample surface [11]. However, in an XPS and HREELS study of Al_2O_3-supported Pd it has been shown that reduced alumina surfaces induce a stronger electronic interaction with palladium than stoichiometric surfaces [12]. This is in agreement with studies of Pt on $TiO_2(110)$ [16], where it was found that there is no charge transfer between Pt and stoichiometric $TiO_2(110)$. However, a decrease in Ti^{3+} ions was observed when Pt was evaporated onto reduced $TiO_2(110)$.

A number of studies of the interaction of CO with the Rh/CeO_x surface have been conducted [3-8]. Mullins *et al.* [5, 6] studied CO adsorption on $Rh/CeO_x(111)/Ru(0001)$ using SXPS and TPD. C 1s spectra from their study showed that at low temperatures (below 200 K) two peaks are observed, indicating that there is CO adsorption on both the CeO_x and Rh surfaces. At 300 K there is only adsorption of CO on the metal particles and, as the temperature is increased above 400 K, CO dissociation is observed.

XPS studies of CO adsorbing on Pd(111) single crystal surfaces have also been conducted [17-19]. Surnev *et al.* studied CO adsorption onto clean Pd(111) using XPS and HREELS. They found, from C 1s XPS, that as the CO coverage is increased the bridge site contribution increases and the hollow site contribution decreases, in good agreement with previous RAIRS studies [20, 21]. Characterisation of the interaction of CO with single crystal Pd surfaces provides a useful comparison for identifying the exposed facets of oxide supported Pd particles in model catalysts.

Despite the high level of interest in oxide-supported palladium particles there have been no previous investigations into the Pd/CeO_{2-x} system and its interaction with CO using XPS. In this study the CO interaction with Pd clusters deposited on reduced CeO_2 thin films, grown on a Pt(111) crystal, has been studied using XPS. Ce 3d XP spectra have been used to deduce the oxidation state of the CeO_{2-x} thin film, and how this is modified by the presence of Pd on

the surface, and by the adsorption of CO. Experiments have been performed on surfaces with varying amounts of Pd deposited on the CeO_{2-x}/Pt(111) surface.

Experimental

The experiments were performed in a UHV chamber with a base pressure of $\leq 2 \times 10^{-10}$ mbar. The system contained all facilities necessary for sample preparation (Ar^+ sputtering and annealing) and characterisation (low energy electron diffraction (LEED) and X-ray photoelectron spectroscopy (XPS)). All data was recorded at room temperature, using unpolarised Mg Kα radiation (hν=1253.6 eV) as the photon source, and a VSW/Omicron EA125 analyser with a 5-channeltron detection system to detect the photoelectrons (see chapter 3). Binding energies are referred to the Pt $4f_{7/2}$ core level of the clean Pt(111) surface, at 71.2 eV.

CO was dosed onto the surface at room temperature via a high precision leak valve. The ion gauge sensitivity was not corrected for CO. All exposures are measured in Langmuir (L), where 1 L is equivalent to a dose of 1.32×10^{-6} mbar for 1 second. The sample was electron-beam heated and the sample temperature was measured by a K-type thermocouple, which was attached to the sample back plate.

Cerium was deposited from an electron beam evaporator and CeO_{2-x} thin films were grown using the method described in chapter 4. The number of monolayers of CeO_{2-x} on the Pt(111) sample was calculated using XPS peak intensities [22]. The same CeO_{2-x} thin film could not be used for multiple experiments due to CO contamination. Hence, before each set of experiments the sample was cleaned and a new CeO_{2-x} thin film was grown. An identical growth process was used in each case, and each set of XPS data was repeated to ensure consistency of results.

Palladium was evaporated onto the sample at room temperature from a piece of wire, using an electron beam evaporator, see chapter 3. The palladium doser was

calibrated by dosing Pd onto the clean Pt(111) surface for known periods of time and monitoring the Pd 3d peak heights using XPS. Palladium grows on Pt(111) according to a layer-by-layer growth model [23], hence the Pd XPS signal will increase linearly with time until the first monolayer of Pd has been deposited. After the 1 ML Pd coverage has been achieved the signal will continue to increase linearly with time, but the gradient will be different. This is shown in Figure 6.1, where 1 ML Pd coverage was reached after dosing for 90 seconds.

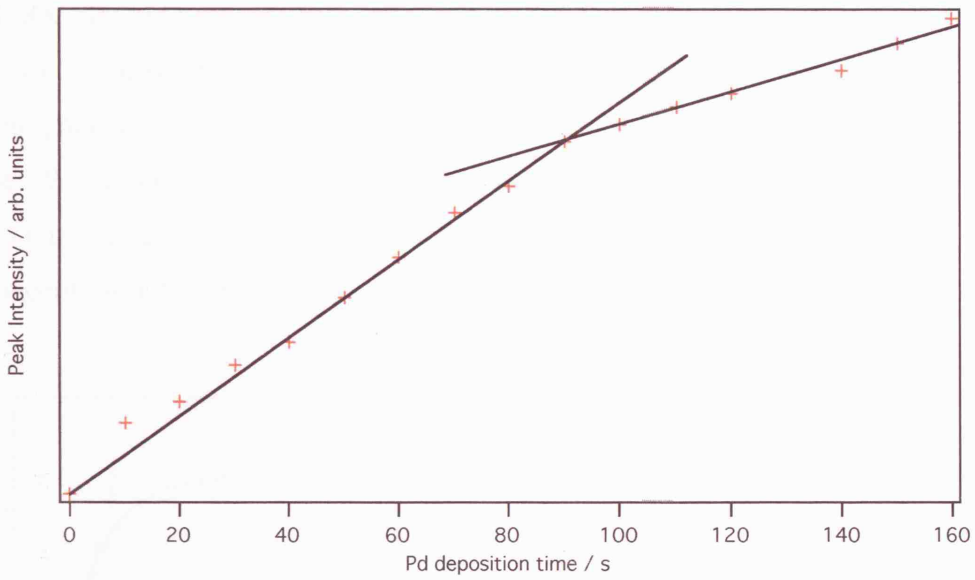

Figure 6.1 Pd $3d_{3/2}$ XPS peak intensity plotted against the Pd deposition time.

Results and discussion

Pd/CeO_{2-x}/Pt(111)

Two methods of CeO_{2-x} thin film production have been used, as described in detail in chapter 4, resulting in thin films with different Ce^{3+} concentrations. The effects of dosing Pd onto these two different CeO_{2-x} thin films will now be discussed.

The percentage contribution of Ce^{3+} has been calculated by deconvoluting the Ce 3d XP spectra into the ten Gaussian contributions, four of which are Ce^{3+} related, and six of which are Ce^{4+} contributions. By calculating the area under

these Gaussians the oxidation state can be calculated, as discussed previously in chapter 4.

The first method of growing CeO_{2-x} thin films resulted in an initial Ce^{3+} concentration of 17.5 ± 0.4%. It was found that the Ce^{3+} concentration increases to 25.5 ± 0.7% after 1 MLE of Pd is dosed onto the surface, as shown in Figure 6.2. The Ce^{3+} concentration remains constant at 25.5 ± 0.7% after 2 MLE of Pd has been dosed onto the surface. Figure 6.3 shows Ce 3d spectra for a clean 3 MLE CeO_{2-x}/Pt(111) sample before and after 10 MLE Pd has been dosed onto the surface. The positions of Ce^{3+} and Ce^{4+} related peaks have been marked on the figure, and it can be seen that the Ce^{3+} concentration has increased after the Pd dose. When these spectra were background subtracted and deconvoluted into the 10 Gaussian contributions it was found that there was an ~8% increase in Ce^{3+} concentration following Pd deposition from 17.5 ± 0.4% to 25.5 ± 0.7%.

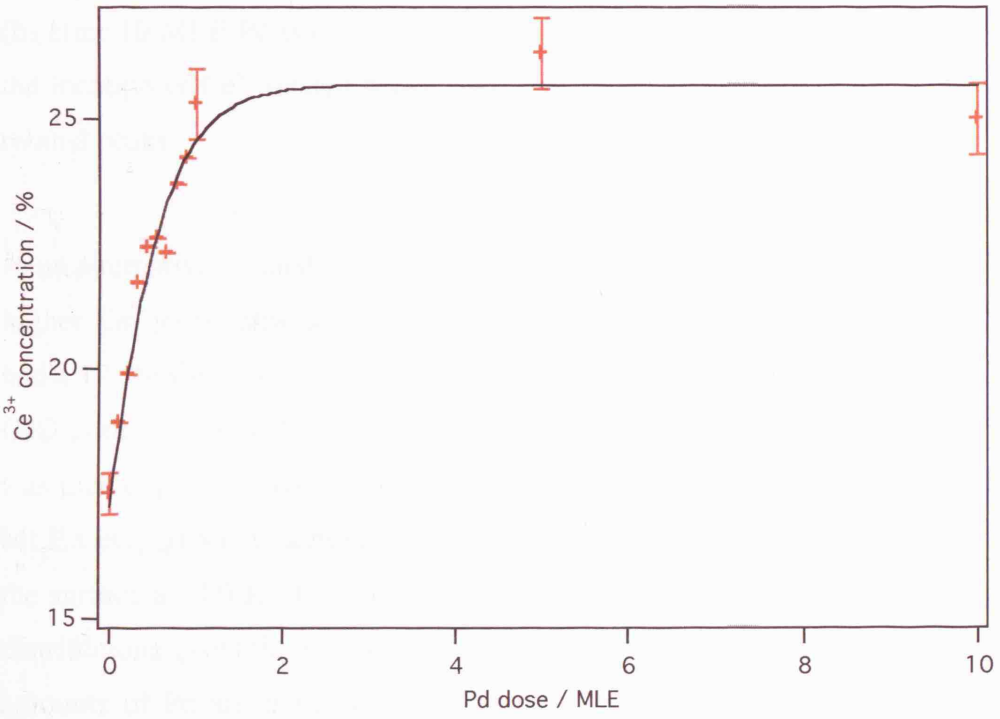

Figure 6.2 Graph showing the change in Ce^{3+} concentration of a 3 MLE $CeO_{1.91}$ thin film as Pd is dosed onto the $CeO_{1.91}$/Pt(111) surface. The percentage Ce^{3+} concentration has been calculated by deconvolution of Ce 3d XP spectra into the 10 Gaussian contributions.

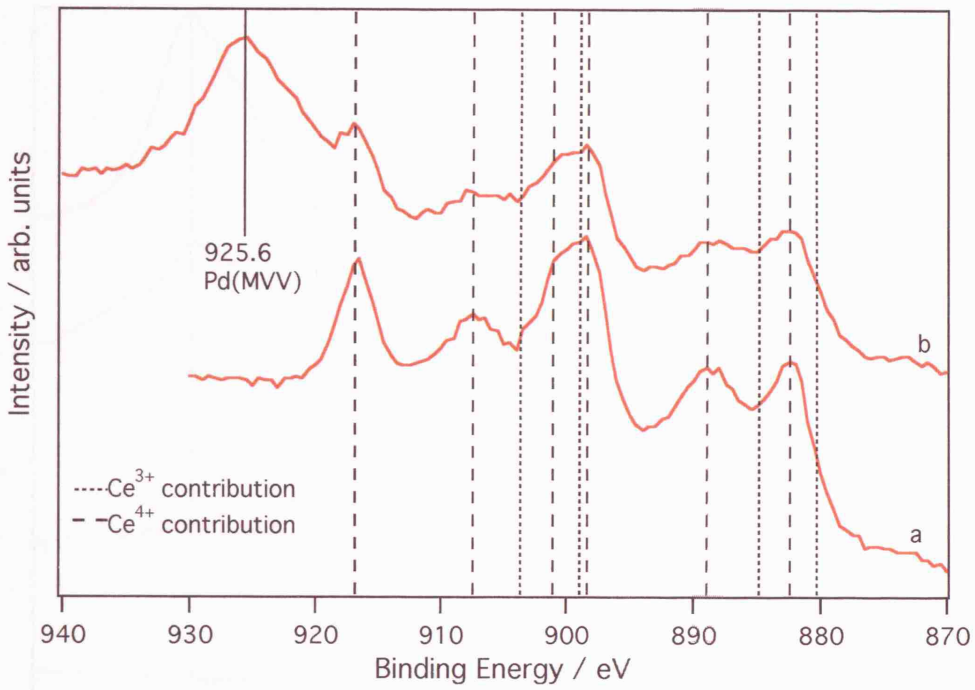

Figure 6.3 Ce 3d XP spectra of a 3 MLE $CeO_{1.91}$/Pt(111) sample (a) before, and (b) after 10 MLE Pd is dosed onto the surface at 300 K. Dashed lines indicate the location of Ce^{4+} related peaks, and dotted lines indicate the location of Ce^{3+} related peaks.

In an alternative method of CeO_{2-x} thin film production, CeO_{2-x} thin films with a higher Ce^{3+} concentration were produced by annealing the $CeO_{1.91}$ film, which had a 17.5% Ce^{3+} concentration, in UHV for 1 minute at 975 K. This resulted in $CeO_{1.84}$ thin films with approximately 32% Ce^{3+}, as discussed in chapter 4. Pd was then deposited onto this film. Figure 6.4 shows Ce 3d spectra for a clean 3 MLE $CeO_{1.84}$/Pt(111) sample as increasing amounts of Pd have been dosed onto the surface at 300 K. Deconvolution of the Ce 3d spectra into the 10 Gaussian distributions gives the Ce^{3+} concentration of the CeO_{2-x} thin film as increasing amounts of Pd are dosed onto the surface (Figure 6.5). Figure 6.5 shows a gradual increase in Ce^{3+} concentration as the amount of Pd present increases, and it appears that the Ce^{3+} concentration has not reached a maximum value even after 10 MLE Pd has been dosed. In contrast, the Ce^{3+} concentration of the $CeO_{1.91}$ thin film (Figure 6.2) reached a maximum after 2 MLE of Pd had been dosed onto the surface.

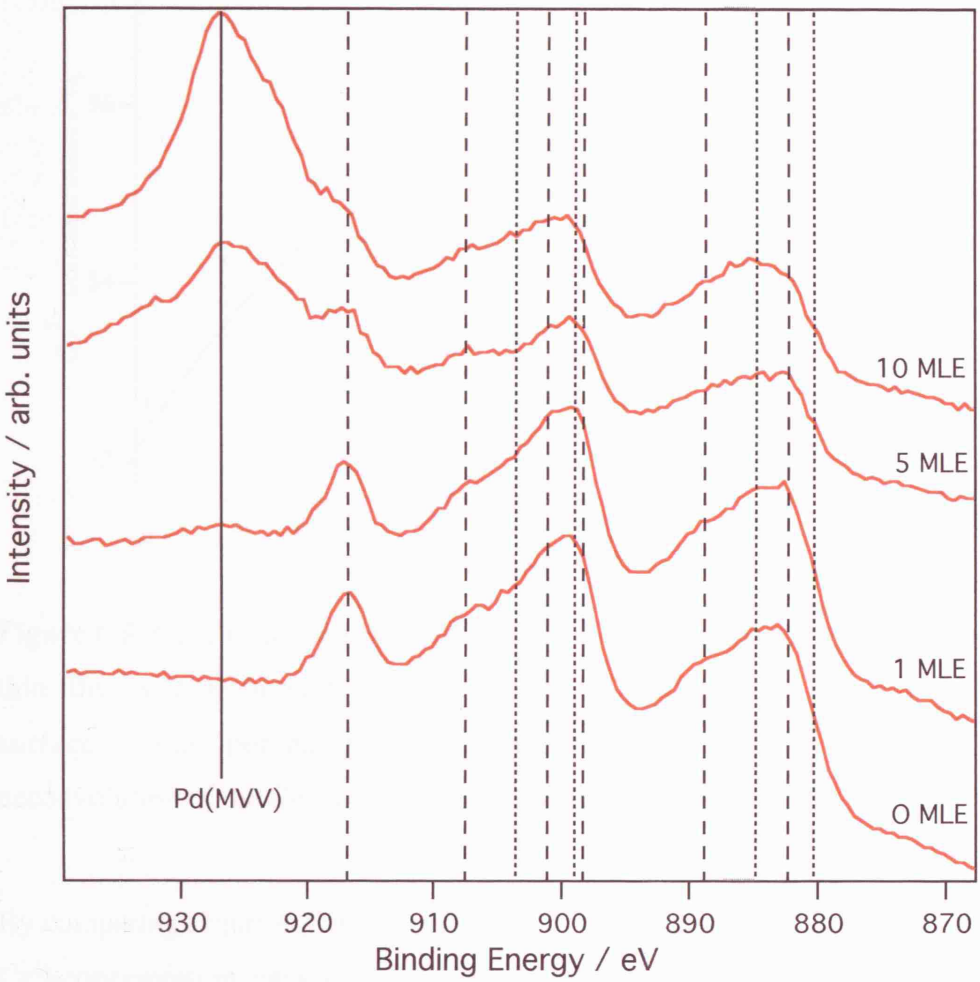

Figure 6.4 Ce 3d XP spectra of a 3 MLE $CeO_{1.84}$/Pt(111) sample with increasing amounts of Pd dosed onto the surface, as indicated on the graph. Dashed lines indicate the location of Ce^{4+} peaks, and dotted lines indicate the location of Ce^{3+} peaks.

The Ce^{3+} concentration of the $CeO_{1.84}$ thin film increases from 32.2 ± 0.5%, with no Pd on the surface, to 37.2 ± 0.5% with 10 MLE of Pd on the surface. Therefore, the introduction of 10 MLE Pd has lead to an increase in the Ce^{3+} concentration of approximately 5%, which is slightly lower than the ~8% increase observed after 10 MLE Pd was deposited on the $CeO_{1.91}$ thin film.

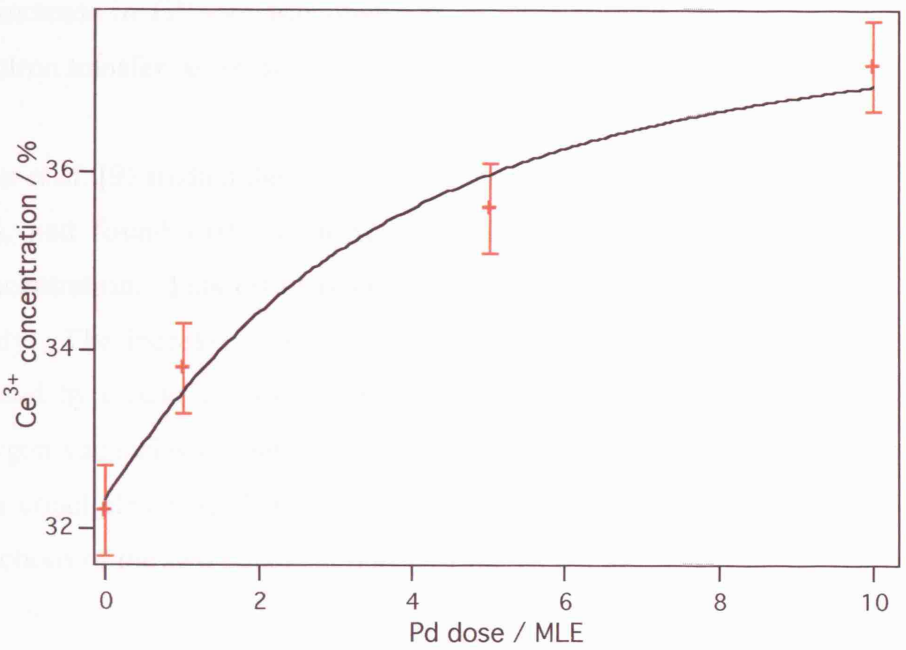

Figure 6.5 Graph showing the change in Ce^{3+} concentration of a 3 MLE $CeO_{1.84}$ thin film, with an initial Ce^{3+} concentration of 32.2%, as Pd is dosed onto the surface. The percentage Ce^{3+} concentration has been calculated by deconvolution of the Ce 3d XP spectra into the 10 Gaussian contributions.

By comparing Figure 6.2 and Figure 6.5 it can be seen that the rate of increase in Ce^{3+} concentration, caused by the presence of Pd on the surface, is considerably slower for the more highly reduced surface. The difference in the rate of increase in the Ce^{3+} concentration could be due to different growth modes of the Pd, caused by different CeO_{2-x}/Pt(111) surface morphologies.

In order to explain the increase in Ce^{3+} concentration when Pd is dosed onto the surface, other noble metal/oxide systems will now be discussed. A number of studies of noble metal nano-particles on TiO_2(110) surfaces have been carried out [11, 16, 24, 25]. Bredrow *et al.* [25] carried out DFT calculations on the interaction between Pd atoms and the TiO_2(110) surface. It was found that the Pd formed covalent bonds with the surface atoms, however there was no sign of significant charge transfer. Schierbaum *et al.* [16] carried out an experimental study of the interaction of Pt with TiO_2(110). For Pt on stoichiometric TiO_2(110) surfaces no charge transfer was observed, in agreement with results for the Pd/TiO_2(110) system. However when Pt was evaporated onto reduced TiO_2(110)

an increase in Ti^{3+} ions was observed, which was interpreted as an indication of electron transfer between the Ti^{3+} and the Pt atoms [16].

Pfau *et al.* [9] studied the effects of dosing Rh onto CeO_2 thin films grown on Pt foil, and found that the presence of Rh leads to an increase in the Ce^{3+} concentration. This result is in agreement with the observations made in this study. The increase in Ce^{3+} concentration observed by Pfau *et al.* could be caused by charge transfer from the Rh to the CeO_2, or by positively charged oxygen vacancies on the surface due to Rh-catalysed desorption of oxygen. It was concluded that charge transfer was the least likely scenario as the work functions of the two bulk materials (Rh and CeO_2) are almost the same [9].

The increase in Ce^{3+} concentration observed in this study could therefore be caused by charge transfer from the Pd to the CeO_2, or by the Pd-catalysed desorption of oxygen. The positions of Pd XPS peaks have been monitored, as a shift in binding energy of the Pd peak from values reported for bulk metallic Pd could indicate oxidation of the Pd, demonstrating that charge transfer has occurred. Also, the ratio of the areas under the O(KVV) Auger peak compared to the Ce 3d peak have been monitored, as any decrease in the amount of oxygen present would indicate that oxygen desorption from the surface had occurred. The oxygen Auger peak has been used here in preference to the O 1s peak as the binding energies of the O 1s and Pd $3p_{3/2}$ peaks are very close and difficult to reliably deconvolute.

It was found that the ratio of areas under the O(KVV) peak compared to that of the Ce 3d peak remained approximately constant, ruling out the possibility that the increase in Ce^{3+} concentration was caused by oxygen desorption from the surface. Figure 6.6 shows Pd 3d spectra for varying Pd coverages on the CeO_{2-x}/Pt(111) surface, where the initial Ce^{3+} concentration of the CeO_{2-x} thin film was approximately 17.5%. From Figure 6.6 it can be seen that the binding energies of the Pd 3d peaks remain constant at 340.3 eV and 335.0 eV as increasing amounts of Pd were dosed onto the 3 MLE CeO_{2-x}/Pt(111) surface. These values are consistent with those for bulk Pd [26], which suggests that there

has been no change in the oxidation state of the Pd. Exactly the same Pd 3d binding energies are observed when Pd was dosed onto $CeO_{1.84}$ thin films with an initial Ce^{3+} concentration of 32.2%.

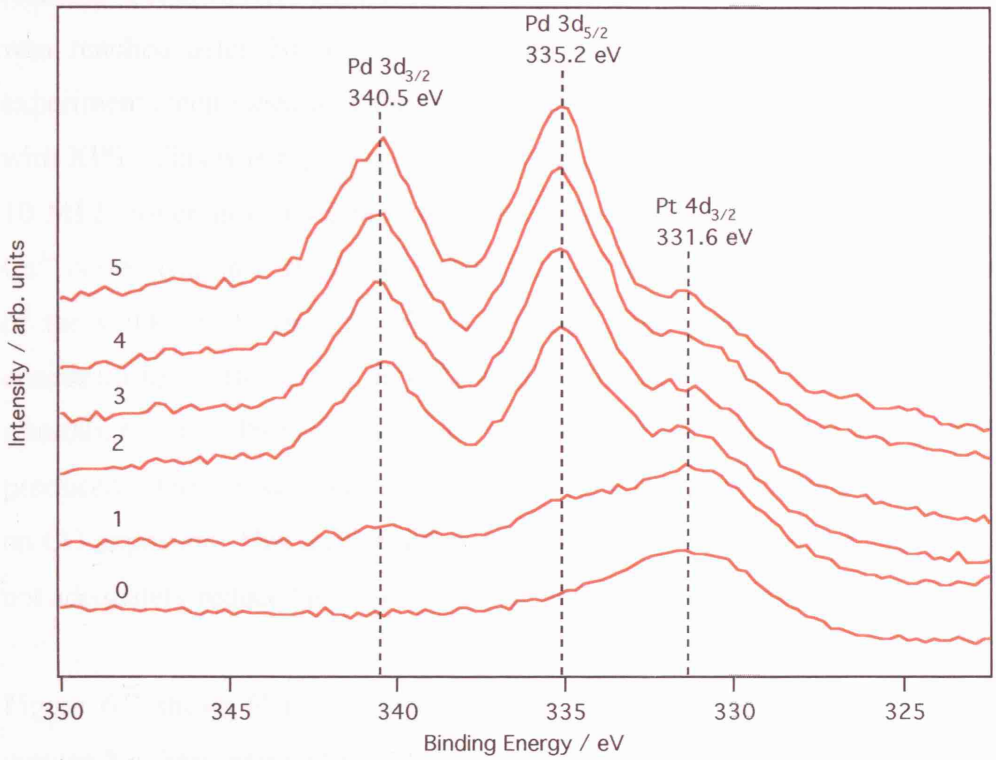

Figure 6.6 Pd $3d_{3/2}$ (340.5 eV), Pd $3d_{5/2}$ (335.2 eV) and Pt $4d_{3/2}$ (331.6 eV) XPS peaks for increasing Pd coverage on the 3 MLE $CeO_{1.91}$/Pt(111) surface at 300 K. Pd coverage is indicated on the figure in MLE.

In conclusion, it is thought that charge transfer from the Pd to the CeO_{2-x} is the most likely cause of the Ce^{3+} concentration increase upon evaporation of Pd onto the CeO_{2-x}/Pt(111) surface. The apparent lack of oxidation of the Pd atoms could be explained by only a small proportion of the Pd atoms present being in contact with the CeO_{2-x}, and hence being involved in the charge transfer. The previous observation of charge transfer between Pt and TiO_2 atoms when Pt is evaporated onto a reduced TiO_2(110) surface [16] is in agreement with the conclusions reached in this study. It has also been shown that the rate of increase of Ce^{3+} concentration due to the presence of Pd is different for the $CeO_{1.84}$ and $CeO_{1.91}$ thin films, which is thought to be due to different surface morphologies.

CO/Pd/CeO_{2-x}/Pt(111)

CO was dosed onto the sample surface to a level such that CO saturation was reached. From RAIRS experiments (chapter 5) it was found that CO saturation was reached after 20-50 L of CO was dosed into the chamber. For all experiments mentioned here the sample was exposed to 100 L CO and examined with XPS. This was repeated for 3 ML CeO_{2-x}/Pt(111) samples with 0, 1, 5, and 10 MLE coverages of Pd present and for CeO_{2-x} thin films with two different Ce^{3+} concentrations. In all cases there was no change in the Ce^{3+} concentration of the CeO_{2-x} thin film after CO adsorption, independent of the initial Ce^{3+} concentration. Berner *et al.* [27] studied the interaction of CO with CeO_2 ultrathin films on Pt(111), and found that only strongly reduced CeO_{2-x} samples, produced either by vacuum-annealing or H_2O interaction, were further reduced on CO exposure. This indicates that the CeO_{2-x} thin films used in this study were not adequately reduced to observe further reduction on CO exposure.

Figure 6.7 shows C 1s XP spectra of the Pd/$CeO_{1.91}$/Pt(111) sample after the surface has been exposed to 100 L CO. Before discussing the spectra from this study in any detail the adsorption of CO onto Pt(111) and Pd(111) surfaces will be considered in order to act as a comparison. The C 1s spectrum for CO adsorbed onto the clean Pt(111) crystal has also been included in Figure 6.7 for reference. This shows a very broad peak with a binding energy of approximately 286 eV. The width of the peak suggests that it consists of a number of different contributions. In XPS studies of CO adsorption on Pt(111) at 200 K [28] the C 1s spectrum consists of two Gaussian peaks at binding energies of 286.8 eV and 286.1 eV, due to CO adsorbed in atop and bridge sites respectively. The binding energy of the C 1s peak observed in this study (Figure 6.7) is consistent with those observed in the previous study, however the resolution in this study is not good enough to separate the spectrum into the two expected components.

Surnev *et al.* [19] have studied CO adsorption on a clean Pd(111) crystal using XPS. They found that the C 1s spectrum consists of two Gaussian contributions

at binding energies of 285.5 eV and 285.7 eV relating to CO adsorbed in threefold hollow and bridge sites respectively.

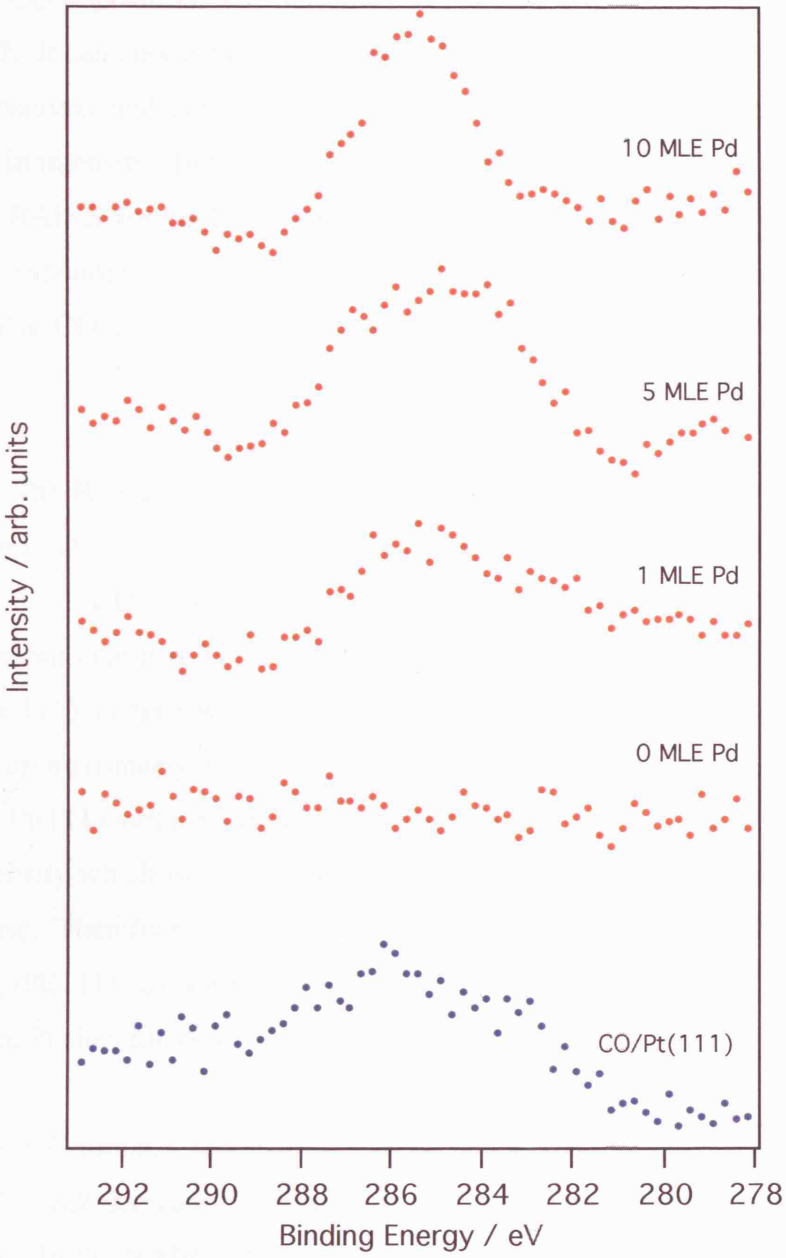

Figure 6.7 Red traces show C 1s XP difference spectra of $Pd/CeO_{1.91}/Pt(111)$ surfaces with varying amounts of Pd on the surface, after the surface has been exposed to 100 L CO at room temperature. The blue trace shows the C 1s spectra after 100 L CO has been dosed onto a clean Pt(111) sample at 300 K. In all cases C 1s spectra were taken before and after CO exposure, and the traces shown are the difference between these two sets of spectra.

In this study C 1s XP spectra of $Pd/CeO_{2-x}/Pt(111)$ surfaces were recorded before and after CO deposition, and the difference between these spectra is shown in Figure 6.7. It can clearly be seen that when there is no Pd on the surface no C 1s peak is observed, and as the amount of Pd on the surface increases the C 1s peak increases in intensity. In fact, the C uptake is proportional to the Pd coverage, in line with RAIRS results for $CO/Pd/CeO_{1.91}/Pt(111)$ [29] (chapter 5). There is also a corresponding increase in the O KVV Auger peak. This uptake behaviour suggests that CO may act as a surfactant for Pd, as proposed for Pt on $TiO_2(110)$ [30].

However, the RAIRS study also showed that there were bare Pt sites on the $CeO_{1.91}/Pt(111)$ surface, so it would be expected that a C 1s peak would be observed after CO was dosed onto the $CeO_{1.91}/Pt(111)$ surface, due to CO adsorption onto the bare Pt sites. The RAIRS study showed that 17 ± 2% of the $CeO_{1.91}/Pt(111)$ surface was bare Pt, which would indicate that the C 1s peak would be approximately 83% smaller on the $CeO_{1.91}/Pt(111)$ surface compared to the clean Pt(111) surface. Hence, this would result in a C 1s peak with a very small intensity which would not be large enough to be observed above the level of the noise. Therefore, in all of the C 1s spectra shown for CO adsorbed on the $Pd/CeO_{1.91}/Pt(111)$ surface the contribution of a C 1s peak due to CO adsorbed on the bare Pt sites can be assumed to be negligible.

As shown in Figure 6.7, as the amount of Pd on the surface is increased the width of the C 1s peak decreases, indicating the presence of more species at lower Pd coverages. In the RAIRS study of the 1 MLE $Pd/CeO_{1.91}/Pt(111)$ surface [29] only a single broad CO–Pd peak is observed on CO saturation making it difficult to tell from RAIRS data alone whether Pd(111) and/or (100) faces are present, or if a defect rich Pd surface is present. This suggests that for low Pd coverages a large number of contributions to the C 1s spectrum, due to the variety of CO-Pd bonding sites, would be expected. For CO saturation on the 10 MLE $Pd/CeO_{1.91}/Pt(111)$ surface RAIRS data showed that the deposited Pd forms

islands, with both (111) and (100) faces, which would result in less contributions to the C 1s spectrum, resulting in a narrower peak.

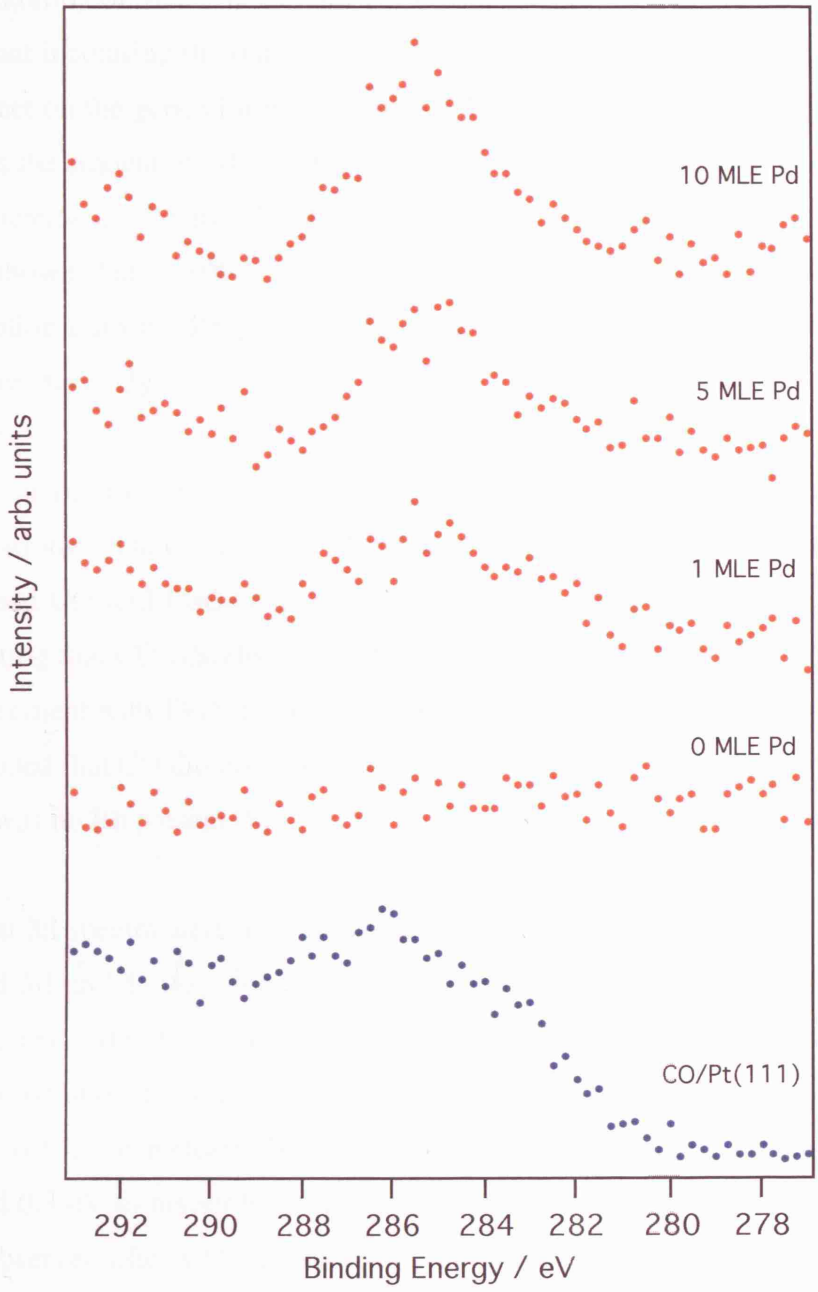

Figure 6.8 Red traces show C 1s XP difference spectra of $Pd/CeO_{1.84}/Pt(111)$ surfaces with varying amounts of Pd on the surface, after the surface has been exposed to 100 L CO at room temperature. The blue trace shows the C 1s spectrum after 100 L CO has been dosed onto a clean Pt(111) sample at 300 K. In all cases C 1s spectra were taken before and after CO exposure, and the traces shown are the difference between these two sets of data.

Figure 6.8 shows the C 1s XP spectra for $Pd/CeO_{1.84}/Pt(111)$ surfaces after 100 L of CO has been dosed into the chamber, for CeO_{2-x} thin films with an initial Ce^{3+} concentration of 32.2 ± 0.5%. By comparing Figure 6.7 and Figure 6.8 it can be seen that increasing the initial Ce^{3+} concentration of the CeO_{2-x} thin film has had no effect on the general trends observed. It can clearly be seen from Figure 6.8 that, as the amount of Pd present on the surface increases, the C 1s peak intensity also increases. Previous SXPS studies of CO adsorption onto Rh/CeO_x [5, 6] have shown that at 300 K only a single C 1s peak is observed indicating CO adsorption onto the Rh particles, which is in agreement with the observations made in this study.

Nolan *et al.* [31, 32] studied CO adsorption on ceria surfaces using DFT calculations. They found that there is only a very weak interaction between adsorbed CO and $CeO_2(111)$, which is consistent with results from this study indicating that CO adsorbs on the Pd nanoclusters and not on CeO_x. This is also in agreement with TPD studies of CO adsorption on $Rh/CeO_2(111)$, where it was concluded that CO did not adsorb on clean $CeO_2(111)$ at room temperature when there was no Rh present [8].

The Pd 3d spectra were also monitored during CO exposure. Figure 6.9 shows the Pd 3d and Pt $4d_{3/2}$ XP spectra for the 10 MLE $Pd/CeO_{1.91}/Pt(111)$ sample before and after CO exposure. Once these spectra have been background subtracted and deconvoluted into the three separate contributions, as shown in Figure 6.10, it can clearly be seen that after CO exposure the Pd 3d peaks have shifted 0.3 eV to higher binding energy. Exactly the same binding energy shift was observed after CO exposure to 1 and 5 MLE $Pd/CeO_{1.91}/Pt(111)$ samples, where all binding energies are referred to the Pt $4f_{7/2}$ core level peak. Exactly the same trend was also observed when CeO_{2-x} thin films of a higher Ce^{3+} concentration were used.

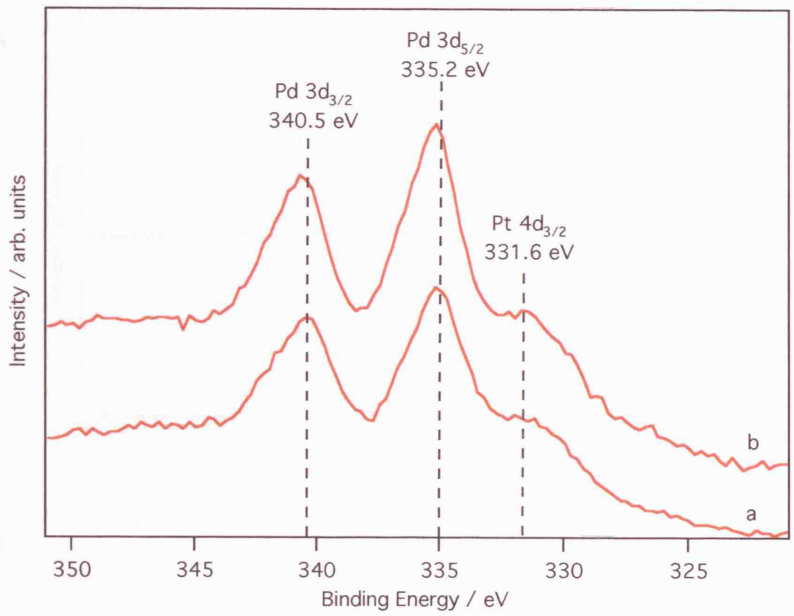

Figure 6.9 Pd 3d and Pt $4d_{3/2}$ spectra for a 10 MLE $Pd/CeO_{1.91}/Pt(111)$ sample (a) before and (b) after a 100 L CO exposure at 300 K. Before dosing CO the binding energies of the Pd $3d_{3/2}$, Pd $3d_{5/2}$, and Pt $4d_{3/2}$ peaks were 340.5 eV, 335.2 eV and 331.6 eV respectively.

This shift to higher binding energy could suggest that the Pd has been oxidised by the CO. When considered alongside the observation that there has been no change in the oxidation state of the CeO_{2-x} thin film, this suggests that the CO has adsorbed on the Pd and not on the CeO_{2-x}. This is in good agreement with the RAIRS study (Chapter 5). However, there is strong evidence from other metal/oxide studies that suggests that this may not be the cause of the binding energy shift. Mullins [33] has studied the effect of CO adsorption onto a Rh/CeO_x model catalyst using SXPS. In this study the Rh $3d_{5/2}$ peak was found to shift 0.2 eV to higher binding energy upon CO saturation of the surface at 300 K. This is in good agreement with observations made in the present study for the Pd/CeO_{2-x} model catalyst. However Mullins stated that this shift in binding energy is due to reduced final state screening in the small metal particles adsorbed on the oxide, and not due to the oxidation of the Rh. Similar shifts in Pd 3d binding energies have been observed when adsorbing CO onto Pd(111) [19], $Pd/TiO_2(110)$ [10] and $Pd/Al_2O_3/NiAl(110)$ [13] surfaces, as well as Pt/TiO_2 [30].

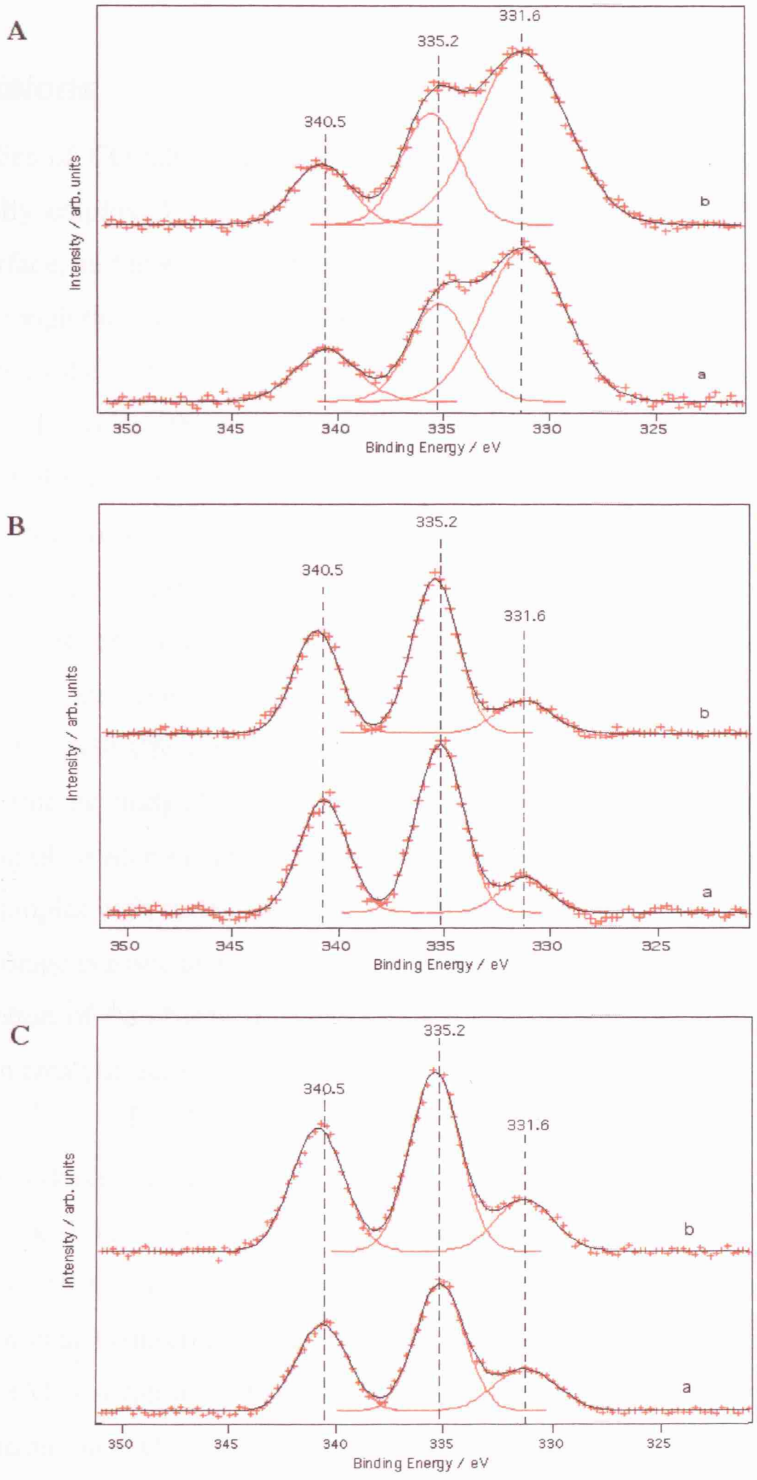

Figure 6.10 Background subtracted and deconvoluted Pd 3d and Pt $4d_{3/2}$ spectra for A) 1 MLE Pd, B) 5 MLE Pd and C) 10 MLE Pd/$CeO_{1.91}$/Pt(111) surfaces a) before and b) after CO exposure of 100 L at 300 K. Before dosing CO the binding energies of the Pd $3d_{3/2}$, Pd $3d_{5/2}$, and Pt $4d_{3/2}$ peaks were constant for all surfaces at 340.5 eV, 335.2 eV and 331.6 eV, respectively.

Conclusions

XPS studies of CO adsorbed on $Pd/CeO_{2-x}/Pt(111)$ have been carried out and successfully employed to provide information about the oxidation state of the CeO_{2-x} surface, and how it is modified by the presence of Pd and CO. It has been shown, through the use of Ce 3d XPS, that the Ce^{3+} concentration increases as Pd is dosed onto the $CeO_{2-x}/Pt(111)$ surface, due to charge transfer from the Pd to the CeO_{2-x}. However, the rate of increase in Ce^{3+} concentration, with respect to the amount of Pd on the surface, is dependent on the initial Ce^{3+} concentration of the CeO_{2-x} thin films. This is thought to be due to the difference in surface morphology, and a faster rate is observed for CeO_{2-x} thin films with a lower initial Ce^{3+} concentration. The role of ceria in automobile emissions-control catalysts is as an oxygen storage and release component, hence the oxidation state of CeO_{2-x} will affect its catalytic activity [34]. Yang *et al.* [35] have carried out a calorimetric study of oxygen storage in Pd/ceria, and it has been shown that the binding of oxygen in ceria is stronger in well crystallised solids compared to reduced samples with surface defects. This suggests that the oxygen involved in oxygen storage is associated with defects. The increase of the Ce^{3+} concentration on adsorption of Pd observed in these experiments would therefore lead to an increase in catalytic activity of the CeO_{2-x}.

When CO is dosed onto the $Pd/CeO_{2-x}/Pt(111)$ surface it has been shown that the C 1s XPS peak increases in intensity as the amount of Pd present increases, independent of the initial Ce^{3+} concentration. The binding energy of the C 1s peak also remains constant independent of Pd coverage, in agreement with SXPS studies of CO adsorption on Rh/CeO_x at 300 K [6]. There is no change in Ce^{3+} concentration on CO adsorption, but the O 1s/Ce 3d peak intensity ratio increases, suggesting that the CO is adsorbing on the Pd in preference to the CeO_{2-x}. This is in agreement with RAIRS studies of the same surface (chapter 5), and SXPS studies of CO adsorption on Rh/CeO_x [6]. A small shift in binding energy of the Pd 3d XPS peaks is also observed, probably due to reduced final state screening in the metal nanoparticles adsorbed on the oxide.

References

1. Trovarelli, A., *Catalysis by ceria and related materials*. Catalytic Science Series, ed. G. Hutchings. Vol. 2. 2000, London: Imperial College Press.
2. Diwell, A.F., Rajaram, R.R., Shaw, H.A., and Truex, T.J., *The role of Ceria in three-way catalysts*, in *Catalysis and Automotive Pollution Control II*, A. Crucq, Editor. 1991, Elsevier Science Publishers: Amsterdam. p. 139.
3. Bunluesin, T., Cordatos, H., and Gorte, R.J., *A study of CO oxidation kinetics on Rh/Ceria*. J. Catal., 1995. **157**: p. 222.
4. Bunluesin, T., Putna, E.S., and Gorte, R.J., *A comparison of CO oxidation on ceria-supported Pt, Pd, and Rh*. Catal. Lett., 1996. **41**: p. 1.
5. Kundakovic, L., Mullins, D.R., and Overbury, S.H., *Adsorption and reaction of H_2O and CO on oxidised and reduced Rh/CeO_x(111) surfaces*. Surf. Sci., 2000. **457**: p. 51.
6. Mullins, D.R., Kundakovic, L., and Overbury, S.H., *The interaction between NO and CO on Rh-loaded CeO_x(111)*. J. Catal., 2000. **195**: p. 169.
7. Mullins, D.R. and Overbury, S.H., *CO dissociation on Rh deposited on reduced cerium oxide thin films*. J. Catal., 1999. **188**: p. 340.
8. Stubenrauch, J. and Vohs, J.M., *Interaction of CO with Rh supported on stoichiometric and reduced CeO_2(111) and CeO_2(100) surfaces*. J. Catal., 1996. **159**: p. 50.
9. Pfau, A., Schierbaum, K.D., and Gopel, W., *The electronic structure of CeO_2 thin films: the influence of Rh surface dopants*. Surf. Sci., 1995. **331-333**: p. 1479.
10. Evans, J., Hayden, B.E., and Lu, G., *The adsorption of carbon monoxide on TiO_2(110) supported palladium*. Surf. Sci., 1996. **360**(1-3): p. 61.
11. Diebold, U., Pan, J.-M., and Madey, T.E., *Ultrathin metal film growth on TiO_2(110): an overview*. Surface Science: Proceedings of the 14th European Conference on Surface Science, 1995. **331-333**(Part 2): p. 845.

12. Ealet, B. and Gillet, E., *Palladium alumina interface: influence of the oxide stoichiometry studied by EELS and XPS.* Surf. Sci., 1993. **281**(1-2): p. 91.

13. Sandell, A., Libuda, J., Bruhwiler, P.A., Andersson, S., Maxwell, A.J., Baumer, M., Martensson, N., and Freund, H.J., *Interaction of CO with Pd clusters supported on a thin alumina film.* J. Vac. Sci. Technol. A-Vac. Surf. Films, 1996. **14**(3): p. 1546.

14. Zilm, K.W., Bonneviot, L., Haller, G.L., Han, O.H., and Kermarec, M., *C-13 NMR-spectra of CO-13 adsorbed on silica-supported palladium particles - particle-size dependence of the surface-diffusion rate and the C-13 Knight-shift.* J. Phys. Chem., 1990. **94**(23): p. 8495.

15. Leighton, C.A., Swift, A.J., and Vickerman, J.C., *Further characterisation of Pd deposited on an extensively oxidised Zn(001) support.* Surf. Sci., 1991. **253**(1-3): p. 220.

16. Schierbaum, K.D., Fischer, S., Torquemada, M.C., de Segovia, J.L., Roman, E., and Martin-Gago, J.A., *The interaction of Pt with TiO_2(110) surfaces: a comparative XPS, UPS, ISS, and ESD study.* Surf. Sci., 1996. **345**(3): p. 261.

17. Rupprechter, G., Kaichev, V.V., Unterhalt, H., Morkel, A., and Bukhtiyarov, V.I., *CO dissociation and CO hydrogenation on smooth and ion-bombarded Pd(111): SFG and XPS spectroscopy at mbar pressures.* Applied Surface Science, 2004. **235**(1-2): p. 26.

18. Kaichev, V.V., Prosvirin, I.P., Bukhtiyarov, V.I., Unterhalt, H., Rupprechter, G., and Freund, H.J., *High-pressure studies of CO adsorption on Pd(111) by X-ray photoelectron spectroscopy and sum-frequency generation.* J. Phys. Chem. B, 2003. **107**(15): p. 3522.

19. Surnev, S., Sock, M., Ramsey, M.G., Netzer, F.P., Wiklund, M., Borg, M., and Andersen, J.N., *CO adsorption on Pd(111): a high-resolution core level photoemission and electron energy loss spectroscopy study.* Surf. Sci., 2000. **470**(1-2): p. 171.

20. Hoffmann, F.M., *Infrared reflection-absorption spectroscopy of adsorbed molecules.* Surf. Sci. Rep., 1983. **3**(2/3): p. 107.

21. Bradshaw, A.M. and Hoffmann, F.M., *Chemisorption of carbon-monoxide on palladium single-crystal surfaces - IR spectroscopic evidence for localized site adsorption.* Surf. Sci., 1978. **72**(3): p. 513.

22. Seah, M.P., *Quantification of AES and XPS*, in *Practical Surface Analysis - Auger and X-ray Photoelectron Spectroscopy*, D. Briggs and M.P. Seah, Editors. 1983, Wiley. p. 201.

23. Han, M., Mrozek, P., and Wieckowski, A., *X-ray-photoelectron-spectroscopy and auger-electron-spectroscopy study of ultrathin palladium films on a Pt(111) substrate.* Phys. Rev. B, 1993. **48**(11): p. 8329.

24. Diebold, U., *The surface science of titanium dioxide.* Surf. Sci. Rep., 2003. **48**(5-8): p. 53.

25. Bredow, T. and Pacchioni, G., *A quantum-chemical study of Pd atoms and dimers supported on TiO_2(110) and their interaction with CO.* Surf. Sci., 1999. **426**(1): p. 106.

26. Thompson, A., Attwood, D., Gullikson, E., Howells, M., Kim, K., Kirz, J., Kortright, J., Lindau, I., Pianetta, P., Robinson, A., Scofield, J., Underwood, J., Vaughan, D., Williams, G., and Winick, H., *X-ray data booklet.* 2nd ed. 2001, California: Lawrence Berkeley National Laboratory.

27. Berner, U., Schierbaum, K.-D., Jones, G., Wincott, P., Haq, S., and Thornton, G., *Ultrathin ordered CeO_2 overlayers on Pt(111): interaction with NO_2, NO, H_2O and CO.* Surf. Sci., 2000. **467**: p. 201.

28. Kinne, M., Fuhrmann, T., Whelan, C.M., Zhu, J.F., Pantforder, J., Probst, M., Held, G., Denecke, R., and Steinruck, H.P., *Kinetic parameters of CO adsorbed on Pt(111) studied by in situ high resolution x-ray photoelectron spectroscopy.* J. Chem. Phys., 2002. **117**(23): p. 10852.

29. Wilson, E.L., Brown, W.A., and Thornton, G., *RAIRS studies of CO adsorption on Pd/CeO_{2-x}(111)/Pt(111).* Surf. Sci., 2006. **600**(12): p. 2555.

30. Steinruck, H.P., Pesty, F., Zhang, L., and Madey, T.E., *Ultrathin films of Pt on TiO_2(110) - Growth and chemisorption-induced surfactant effects.* Phys. Rev. B, 1995. **51**(4): p. 2427.

31. Nolan, M., Parker, S.C., and Watson, G.W., *Vibrational properties of CO on ceria surfaces*. Surf. Sci., 2006. **600**(14): p. 175.

32. Nolan, M. and Watson, G.W., *The surface dependence of CO adsorption on Ceria*. J. Phys. Chem. B, 2006. **110**: p. 16600.

33. Mullins, D.R., *Reactions on model emission control catalysts studied by soft X-ray photoemission*. J. Electron Spectrosc. Relat. Phenom., 2001. **114**: p. 333.

34. Shelef, M., Graham, G., and McCabe, R., *Ceria and other oxygen storage components in automotive catalysts*, in *Catalysis by Ceria and related materials*, A. Trovarelli, Editor. 2002, Imperial College Press: London. p. 343.

35. Yang, L., Kresnawahjuesa, O., and Gorte, R.J., *A calorimetric study of oxygen-storage in Pd/ceria and Pd/ceria-zirconia catalysts*. Catal. Lett., 2001. **72**(1 - 2): p. 33.

Chapter 7 : XPS studies of CO adsorption on $Pd/CeO_{2-x}/Rh(111)$

Introduction

The interaction of noble metals Pd and Rh with CeO_2 is of interest due the use of these components in automobile catalytic converters. The change in oxidation state of CeO_{2-x} on interaction with Pd and CO is of particular interest, as discussed previously in chapter 4. Experimental studies of CO adsorbed on $Pd/CeO_{2-x}/Pt(111)$ have already been presented in this thesis (see chapters 4, 5 and 6) and in this chapter XPS studies of CO adsorbed on $Pd/CeO_{2-x}/Rh(111)$ will be discussed. A comparison between the two allows determination of whether the substrate onto which the CeO_{2-x} thin films are grown affects the interactions of Pd and/or CO with the CeO_{2-x}. It has previously been shown that the substrate onto which CeO_{2-x} thin films are grown can act to improve the catalytic activity of the CeO_{2-x}, even when there are no bare substrate sites [1].

Previous studies of CeO_2 growth on Rh(111) have been carried out [2-5]. Belton *et al.* [5] evaporated Ce onto Rh(111) and then oxidised it by annealing to 475 K in 1 Torr O_2, which resulted in fully oxidised CeO_2. An alternative method was used by Eck *et al.* [2] who evaporated Ce in 2×10^{-7} mbar O_2 onto Rh(111) at 523 K. The surface structure of the CeO_2 film, as a function of film thickness, was monitored using LEED and STM. It was found that the Rh(111) surface was completely covered after the deposition of a two layer oxide. As the CeO_2 film thickness was further increased three dimensional islands of CeO_2 were observed, exhibiting some crystalline order within the island structures, and resulting in a 1.4×1.4 LEED pattern, relative to the Rh(111) 1×1 pattern [2].

In this study the interaction of CO and Pd with $CeO_{2-x}/Rh(111)$ is investigated, with particular interest in how these interactions alter the oxidation state of the CeO_{2-x} thin films. The method of CeO_{2-x} thin film production used is based on the work of Eck *et al.* [2].

Experimental

The experiments were performed in a UHV chamber with a base pressure of at least 2×10^{-10} mbar. The system contained all facilities necessary for sample preparation (Ar^+ sputtering and annealing) and characterisation (low energy electron diffraction (LEED) and X-ray photoelectron spectroscopy (XPS)). All data was recorded at room temperature, using unpolarised Mg Kα radiation (hν=1253.6 eV) as the photon source, and a VSW/Omicron EA125 analyser with a 5-channeltron detection system to detect the photoelectrons (see chapter 3). Binding energies are referred to the Rh $3d_{5/2}$ core level of the clean Rh(111) surface, at 307.2 eV.

The Rh(111) sample was cleaned by repeated cycles of Ar ion sputtering at 300 K, heating in O_2, and annealing in UHV at 1200 K. Sample cleanliness was confirmed if surface contamination was below the detectable limit of XPS, and if the expected LEED pattern for Rh(111) was observed.

CO was dosed onto the surface at room temperature via a high precision leak valve. The ion gauge sensitivity was not corrected for CO. All exposures are measured in Langmuir (L), where 1 L is equivalent to a dose of 1.32×10^{-6} mbar for 1 second. The sample was electron-beam heated and the sample temperature was measured by a K-type thermocouple, which was attached to the sample back plate.

Cerium was deposited from an electron beam evaporator and CeO_{2-x} thin films were grown using a similar method to that employed by Eck *et al.* [2]. Cerium was deposited onto the clean Rh(111) sample at 550 K in an oxygen pressure of 2×10^{-7} mbar. This resulted in a 1.4×1.4 LEED pattern, relative to the Rh 1×1 spots, as shown in Figure 7.1, indicating the presence of an ordered $CeO_2(111)$ layer.

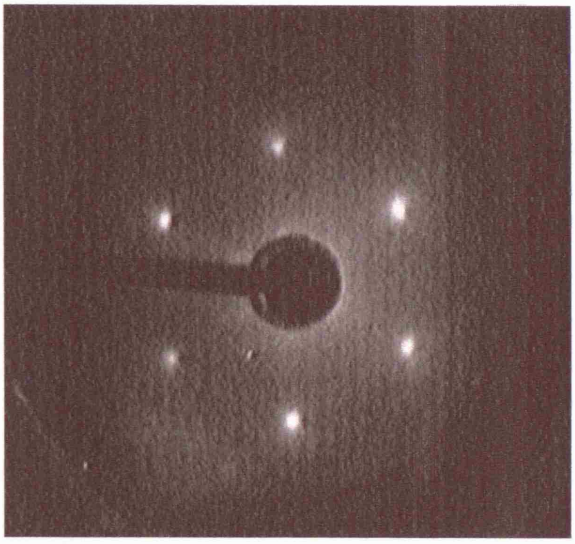

Figure 7.1 LEED pattern of the 3 MLE $CeO_{1.91}$/Rh(111) surface showing CeO_{2-x}(111) 1.4 × 1.4 spots, relative to the Rh(111) 1 × 1 LEED pattern, recorded at a beam energy of 48 eV.

The number of monolayers of CeO_{2-x} on the Rh(111) sample was calculated using XPS peak intensities [6] (the parameters used for these calculations are given in the Appendix). The same CeO_{2-x} thin film could not be used for multiple experiments due to CO contamination. Hence, before each set of experiments the sample was cleaned and a new CeO_{2-x} thin film was grown. An identical growth process was used in each case, and each set of XPS data was repeated to ensure consistency of results.

Palladium was evaporated onto the sample at room temperature from a piece of wire, using an electron beam evaporator, see chapter 3. The palladium doser was calibrated by dosing Pd onto the clean Rh(111) surface for known periods of time and monitoring the Pd 3d peak heights using XPS. Palladium grows on Rh(111) according to a layer-by-layer growth model [7], hence the Rh XPS signal will increase linearly with time until the first monolayer of Pd has been deposited. After the 1 ML Pd coverage has been achieved the signal will continue to increase linearly with time, but the gradient will be different. This is shown in Figure 7.2, where 1 ML Pd coverage was reached after dosing for 40 seconds.

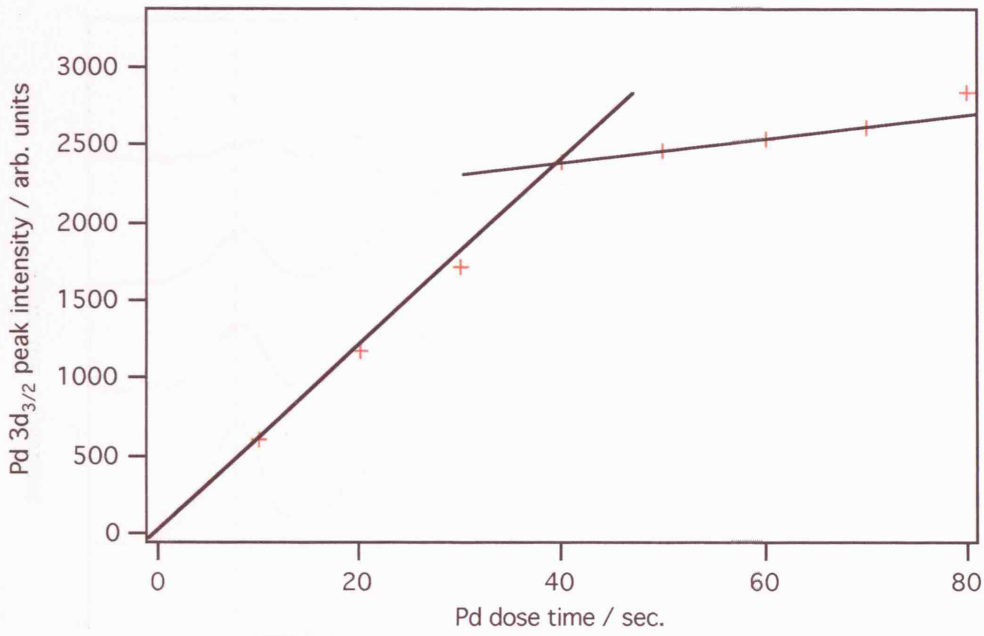

Figure 7.2 Pd $3d_{3/2}$ XPS peak intensity plotted against the Pd deposition time.

Results and discussion

Changing the oxidation state of CeO_{2-x} thin films

In chapter 4 the oxidation state of CeO_{2-x} thin films grown on Pt(111) was altered by annealing in UHV. This method was found to have very little effect on the Ce^{3+} concentration of CeO_{2-x}/Rh(111), and also led to a change in LEED pattern, which is undesirable. Hence, an alternative method was used whereby the oxygen pressure during Ce evaporation onto the Rh(111) crystal was altered. The time spent evaporating Ce and the sample temperature were kept constant. Figure 7.3 shows the Ce 3d spectra of a number of CeO_{2-x} thin films grown under different oxygen pressures. A clear difference in the Ce 3d spectra can be observed dependent on oxygen pressure. The Ce^{3+} concentration was then calculated by fitting the 10 Gaussian contributions given in Table 4.1, chapter 4. The calculated Ce^{3+} concentrations are shown in Table 7.1, and plotted as a function of oxygen pressure in Figure 7.4. Figure 7.4 clearly shows that as the oxygen pressure during Ce deposition is decreased the Ce^{3+} concentration increases.

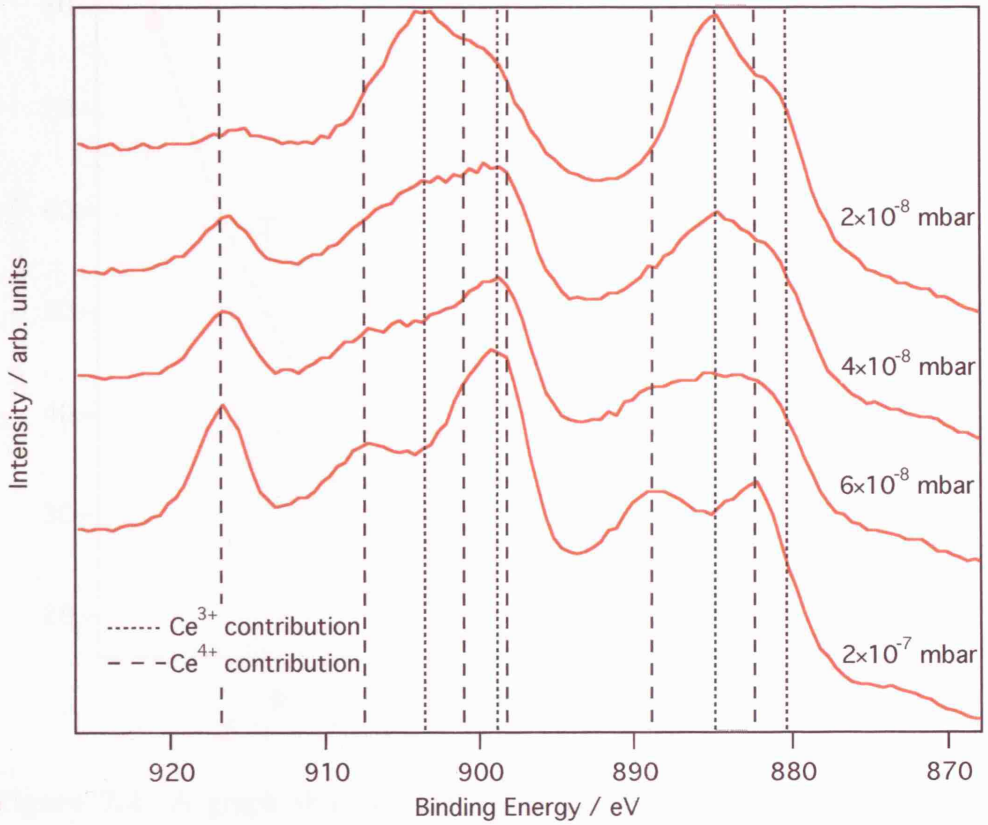

Figure 7.3 Ce 3d XPS spectra for CeO_{2-x} thin films grown on Rh(111) with different oxygen pressures used during Ce deposition. Oxygen pressures used are indicated on the figure. The positions of Ce^{3+} and Ce^{4+} contributions are indicated by dotted and dashed lines respectively.

Oxygen pressure / mbar	Ce^{3+} concentration / %	Error on Ce^{3+} concentration / %	CeO_{2-x}
2×10^{-7}	18.2	1.2	$CeO_{1.91}$
6×10^{-8}	32.0	1.4	$CeO_{1.84}$
4.5×10^{-8}	57.7	1.5	$CeO_{1.71}$
2×10^{-8}	78.6	0.6	$CeO_{1.61}$

Table 7.1 A table showing the change in Ce^{3+} concentration as the oxygen pressure during Ce deposition is altered.

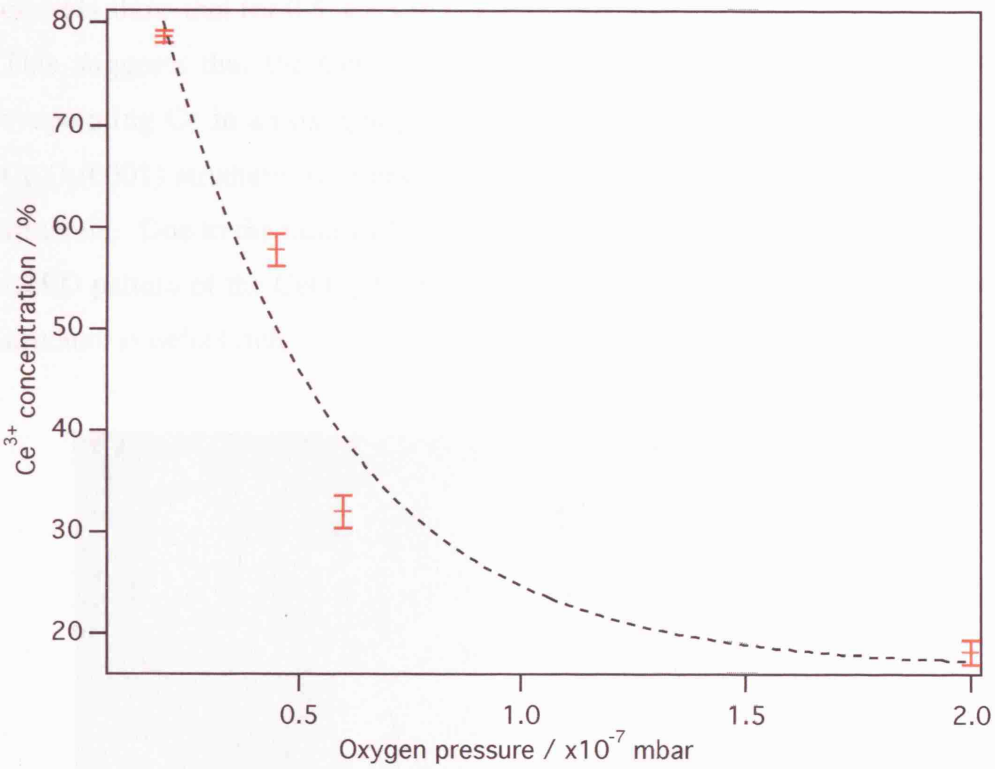

Figure 7.4 A graph showing the dependency of Ce^{3+} concentration on the oxygen pressure during Ce deposition for 6 minutes. The Ce^{3+} concentrations have been calculated using Ce 3d XPS.

The LEED patterns of CeO_{2-x} thin films grown using different oxygen pressures were also monitored, as shown in Figure 7.5, in order to determine the surface structure of the CeO_{2-x} films produced. For all films a 1.4 × 1.4 pattern of spots, relative to the Rh(111) 1 × 1 LEED pattern, was observed. However, as the oxygen pressure was decreased the LEED spots became more faint and less well defined, and the background appeared brighter. This is illustrated in Figure 7.6, where LEED spot intensities are given for the CeO_{2-x} thin films shown in Figure 7.5. It can clearly be seen that the spot intensities are brighter for the less reduced CeO_{2-x} thin films. This indicates that although there are areas of surface order present in all cases, there are fewer ordered areas in films made with lower oxygen pressures. For films with a high Ce^{3+} concentration it is also possible that a $Ce_2O_3(0001)$ thin film could have formed instead of $CeO_2(111)$, as they both have a hexagonal structure and have very similar lattice constants, hence exhibiting the same LEED pattern [8]. X-ray diffraction studies of CeO_{2-x}

crystals show that for $0.5 \leq x \leq 0.3$, a hexagonal Ce_2O_3 structure is observed [9]. This suggests that the $CeO_{1.61}$ (x = 0.39) thin film made in this study by evaporating Ce in an oxygen pressure of 2×10^{-8} mbar most likely exhibits a $Ce_2O_3(0001)$ structure, whereas all other films produced are of the $CeO_{2-x}(111)$ structure. Due to the faint LEED spots and brighter background observed in the LEED pattern of the $CeO_{1.61}$ film (Figure 7.5 a), it is also likely that this surface structure is defect rich.

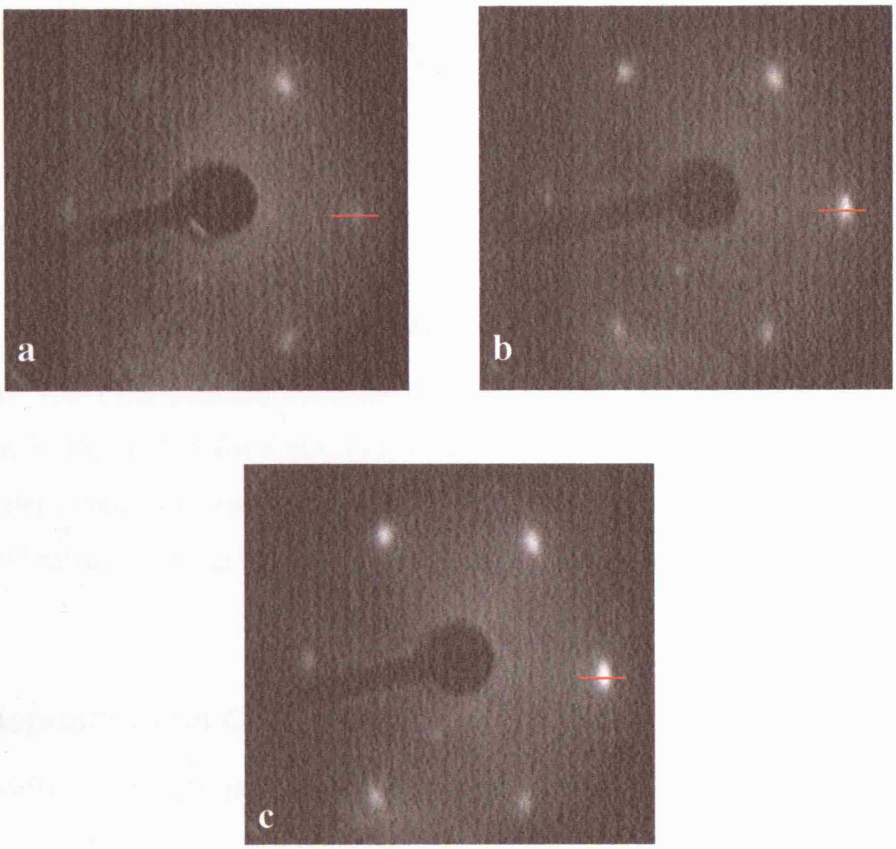

Figure 7.5 LEED pattern of 3 MLE CeO_{2-x}/Rh(111) surfaces for CeO_{2-x} thin films deposited in oxygen pressures of a) 2×10^{-8} mbar, b) 4.5×10^{-8} mbar, c) 6×10^{-8} mbar, resulting in $CeO_{1.61}$, $CeO_{1.71}$, $CeO_{1.84}$ thin films respectively. All LEED patterns were recorded at a beam energy of 33 eV. Red lines indicate the position of line profiles shown in Figure 7.6.

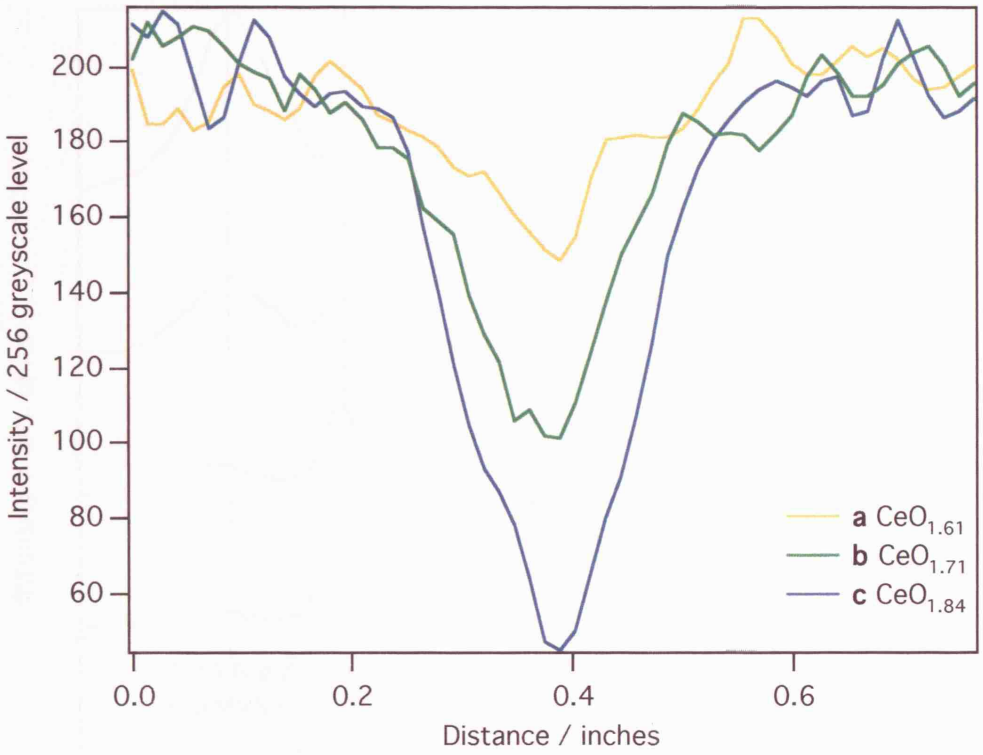

Figure 7.6 Line profiles showing the spot intensities for the LEED images shown in Figure 7.5 for CeO_{2-x}(111)/Rh(111) surfaces. The CeO_{2-x} thin films were deposited in oxygen pressures of a) 2×10^{-8} mbar, b) 4.5×10^{-8} mbar, c) 6×10^{-8} mbar, resulting in $CeO_{1.61}$, $CeO_{1.71}$, and $CeO_{1.84}$ thin films respectively.

Pd deposition on CeO_{2-x}/Rh(111)

Four different oxygen pressures have been used during Ce deposition to produce CeO_{2-x} thin films with different oxidation states. The effects of depositing Pd onto each of these films will now be discussed.

Pd/$CeO_{1.91}$/Rh(111)

Figure 7.7 shows Ce 3d XP spectra taken as increasing amounts of Pd were dosed onto the $CeO_{1.91}$/Rh(111) surface.

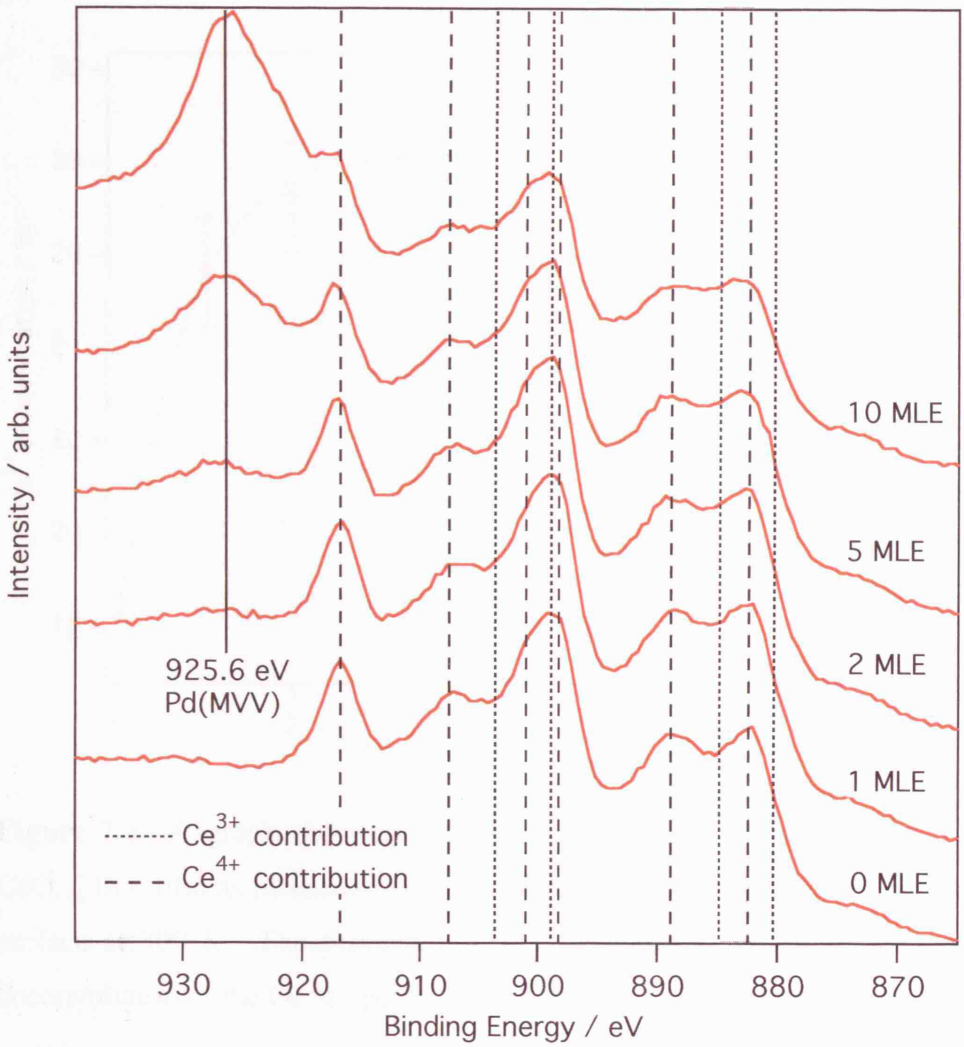

Figure 7.7 Ce 3d XP spectra of 3 MLE $CeO_{1.91}$/Rh(111) as increasing amounts of Pd are deposited onto the surface at 300 K. Pd coverage is indicated on the figure in MLE. Dashed lines indicate the location of Ce^{4+} related peaks, and dotted lines indicate Ce^{3+} related peaks.

The Ce^{3+} concentration was calculated by deconvoluting the Ce 3d XP spectra into the ten Gaussian contributions (shown in chapter 4) and calculating the percentage contribution of Ce^{3+} compared to Ce^{4+}. Figure 7.8 shows how the Ce^{3+} concentration of the $CeO_{1.91}$ thin film varies as Pd is deposited onto the surface. The initial Ce^{3+} concentration of the thin film is 18.2 ± 1.2%, which increases by approximately 7.5% to 25.7 ± 1.2% after deposition of 1 MLE Pd. The increase in Ce^{3+} concentration stops after the deposition of ~2 MLE Pd and levels out at 28.1 ± 1.2%.

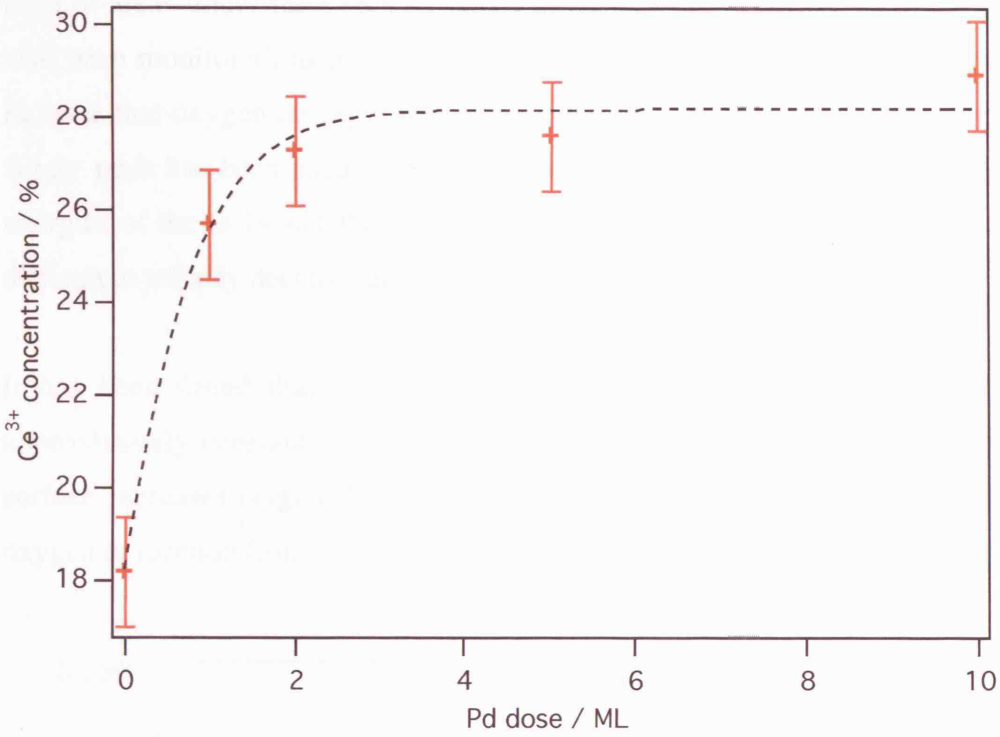

Figure 7.8 A graph showing the change in Ce^{3+} concentration of a 3 MLE $CeO_{1.91}$ thin film as increasing amounts of Pd are dosed onto the $CeO_{1.91}$/Rh(111) surface at 300 K. The percentage Ce^{3+} concentration has been calculated by deconvolution of the Ce 3d spectra into the 10 Gaussian contributions.

The total increase in Ce^{3+} concentration on depositing Pd onto the $CeO_{1.91}$/Rh(111) surface is ~10%, which is slightly larger than the ~8% increase observed when depositing Pd onto the $CeO_{1.91}$/Pt(111) surface (chapter 6). The general trend of the Ce^{3+} concentration with increasing Pd is very similar, with the Ce^{3+} concentration reaching a plateau after deposition of ~2 MLE Pd in both cases. This suggests that in both cases, the Pd is growing in the same way on the underlying CeO_{2-x} thin films.

As discussed in detail in chapter 6, the increase in Ce^{3+} concentration upon deposition of Pd onto the surface could be due to either charge transfer from the Pd to the CeO_{2-x}, or to Pd-catalysed desorption of oxygen. In order to determine the cause of the change in Ce^{3+} concentration, the binding energies of Pd 3d XPS peaks have been monitored, as an increase in binding energy could indicate

oxidation of the Pd, hence demonstrating the occurrence of charge transfer. The ratio of areas under the O(KVV) Auger peak relative to the Ce 3d peaks have also been monitored, as any decrease in the amount of oxygen present would indicate that oxygen desorption from the surface had taken place. The oxygen Auger peak has been used in preference to the O 1s XPS peak as the binding energies of the O 1s and Pd $3p_{3/2}$ peaks are very close in energy, making them difficult to reliably deconvolute.

It has been found that the O(KVV) Auger:Ce 3d XPS area ratios remain approximately constant as the amount of Pd deposited on the $CeO_{1.91}$/Rh(111) surface increases (Figure 7.9). This rules out the possibility of Pd-catalysed oxygen desorption from the surface.

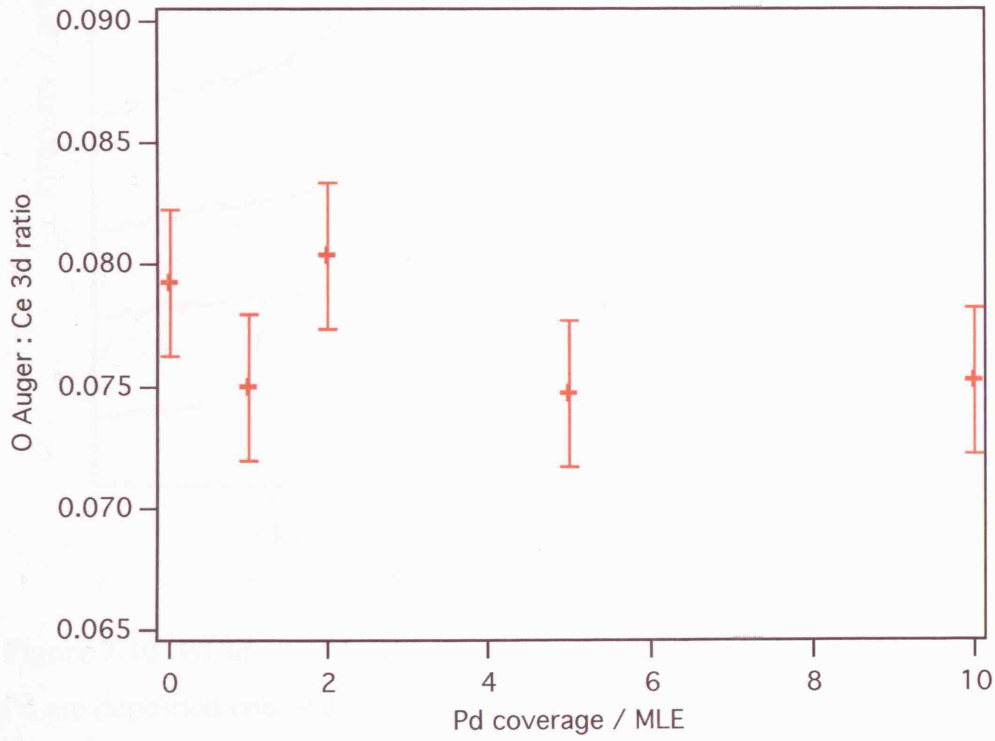

Figure 7.9 The ratio of O(KVV) Auger/Ce 3d XPS peak areas as a function of Pd coverage for Pd deposition onto a $CeO_{1.91}$/Rh(111) surface at 300 K.

Figure 7.10 shows the Pd 3d spectra for $CeO_{1.91}$/Rh(111) after increasing amounts of Pd have been dosed onto the surface. It can be seen that the binding energies for Pd $3d_{3/2, 5/2}$ remain constant at 340.5 eV and 335.2 eV respectively, as

increasing amounts of Pd are deposited onto the surface. These values are consistent with those for bulk Pd [10]. In the case of charge transfer a change in the Pd binding energies compared to the bulk might be expected, however this apparent discrepancy could arise due to the delocalisation of excess positive charge over the three dimensional Pd clusters.

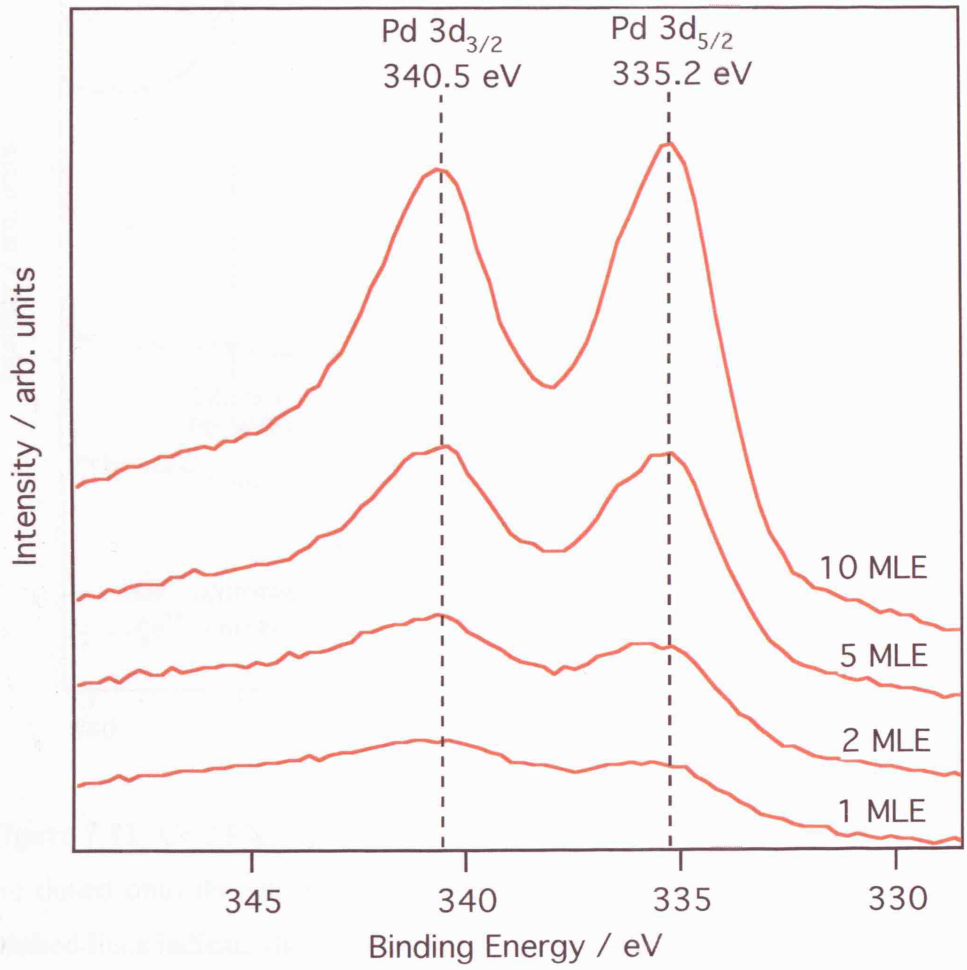

Figure 7.10 Pd $3d_{3/2, 5/2}$ XP spectra of $CeO_{1.91}$/Rh(111) as increasing amounts of Pd are deposited onto the surface at 300 K. Pd coverages are indicated on the graph in MLE.

Pd/$CeO_{1.84}$/Rh(111)

Thin films of $CeO_{1.84}$ on Rh(111), with a Ce^{3+} concentration of 32.0 ± 1.4%, were produced by evaporating Ce in an oxygen pressure of 6×10^{-8} mbar. Pd was then evaporated onto the surface, and the resulting Ce 3d spectra of the

$CeO_{1.84}$/Rh(111) surface with increasing coverages of Pd are shown in Figure 7.11.

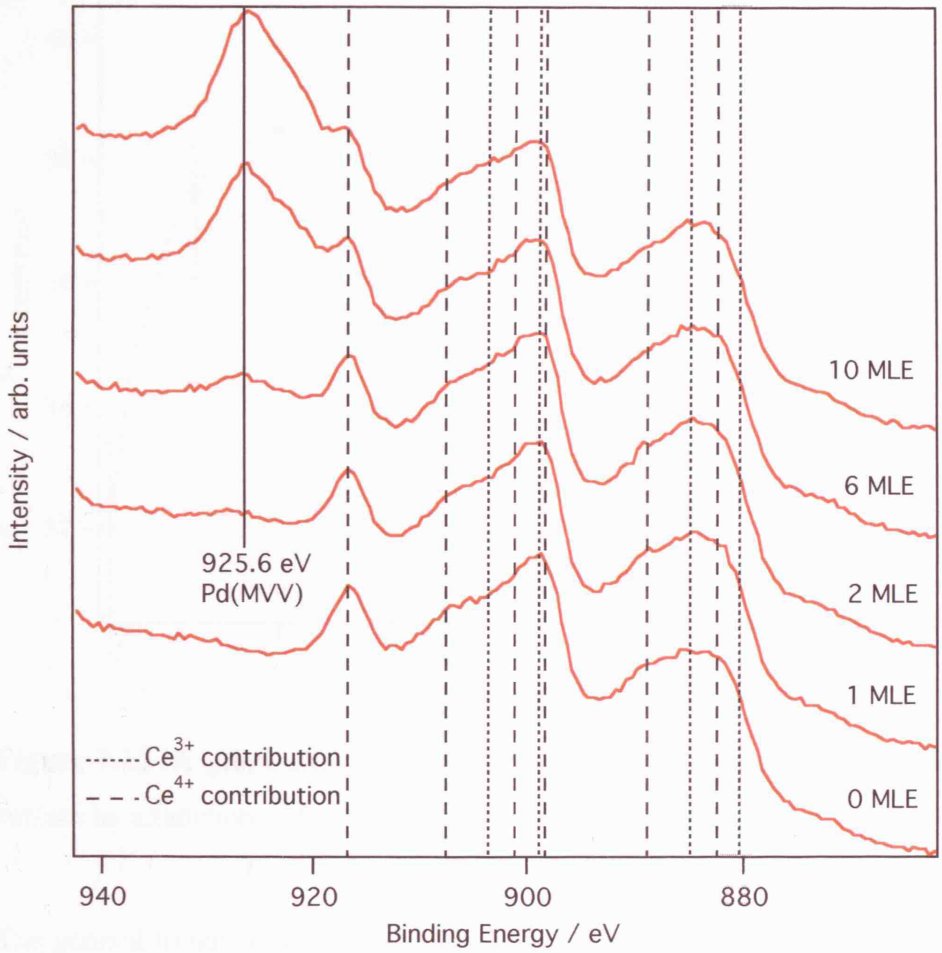

Figure 7.11 Ce 3d XP spectra of $CeO_{1.84}$/Rh(111), as increasing amounts of Pd are dosed onto the surface. Pd coverage in MLE is indicated on the figure. Dashed lines indicate the location of Ce^{4+} related peaks, and dotted lines indicate Ce^{3+} related peaks.

Deconvolution of the Ce 3d spectrum into the 10 Gaussian contributions allows determination of the Ce^{3+} concentration of the $CeO_{1.84}$ thin film. Figure 7.12 shows the change in Ce^{3+} concentration as a function of Pd coverage for $CeO_{1.84}$/Rh(111). The initial Ce^{3+} concentration of the $CeO_{1.84}$ thin film was 32.0 ± 1.4%, which increased by ~5.5% to 37.5 ± 1.4% after the deposition of 1 MLE Pd onto the surface. The Ce^{3+} concentration then appears to stabilise after

deposition of 2 MLE Pd and remains constant at 38.5 ± 1.4% as the Pd coverage is increased to a maximum of 10 MLE.

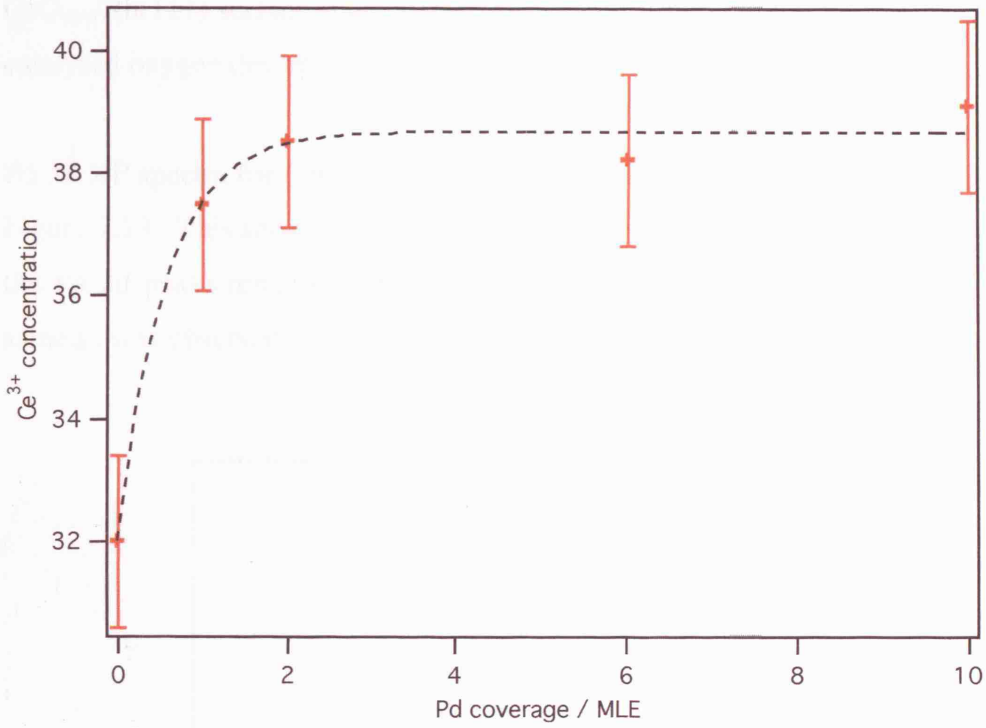

Figure 7.12 A graph showing the Ce^{3+} concentration of a Pd/$CeO_{1.84}$/Rh(111) surface as a function of Pd coverage.

The general trends observed in Figure 7.12 for Pd deposition on $CeO_{1.84}$/Rh(111) are very similar to those observed for Pd deposition on $CeO_{1.91}$/Rh(111) (Figure 7.8). In both cases the Ce^{3+} concentration increases rapidly upon deposition of 1 MLE Pd, and then levels out after 2 MLE Pd has been dosed onto the surface. The total increase in Ce^{3+} concentration is slightly different for the two surfaces, with a ~10% increase being observed for $CeO_{1.91}$/Rh(111), and only a ~6.5% increase being observed for $CeO_{1.84}$/Rh(111). This is in agreement with experiments involving Pd deposition on CeO_{2-x}/Pt(111) (chapter 6), where the increase in Ce^{3+} concentration upon Pd deposition was lower for $CeO_{1.84}$/Pt(111) than $CeO_{1.91}$/Pt(111).

In order to determine the cause of the Ce^{3+} increase on deposition of Pd, Pd 3d XPS and O(KVV) Auger peaks have also been monitored, as before. It was

found that the O(KVV) Auger:integrated Ce 3d XPS area ratios remain approximately constant as the amount of Pd deposited on the $CeO_{1.84}$/Rh(111) surface increases. This is in agreement with observations made for the $CeO_{1.91}$/Rh(111) surface (Figure 7.9), once again ruling out the possibility of Pd-catalysed oxygen desorption from the surface.

Pd 3d XP spectra for $CeO_{1.84}$/Rh(111) with increasing Pd coverage are shown in Figure 7.13. This shows that as the Pd coverage increases the binding energy of the Pd 3d peaks remains constant at values expected for bulk Pd. This is the same as was observed for the $CeO_{1.91}$/Rh(111) surface.

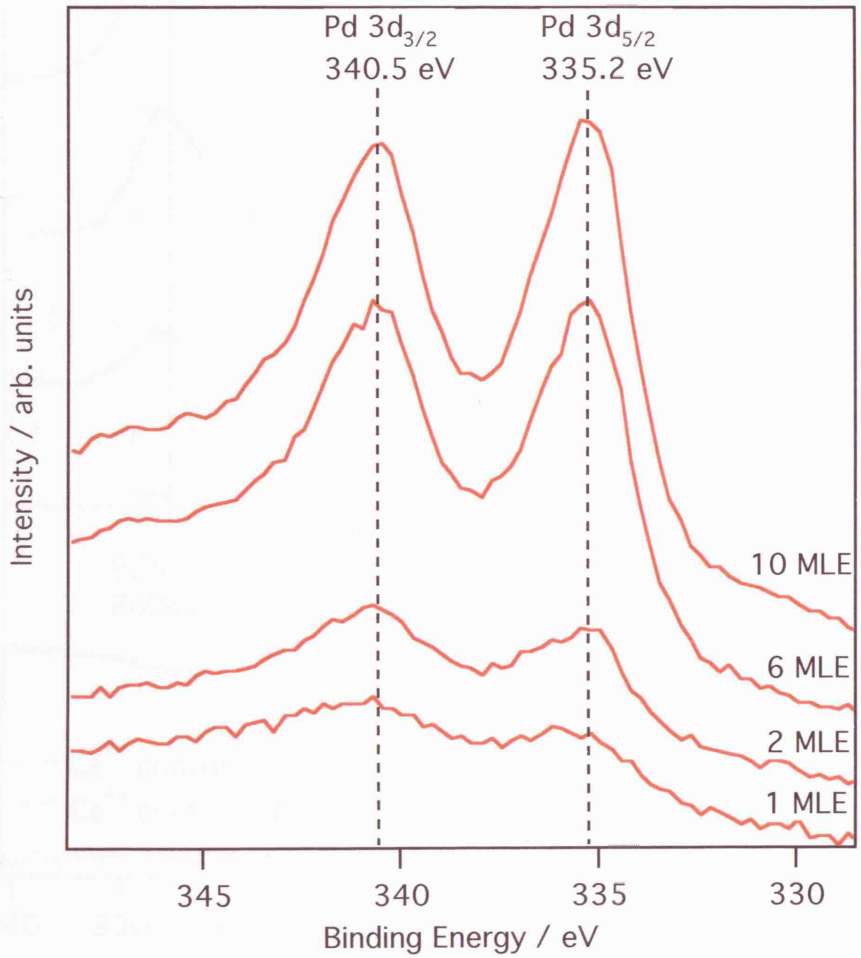

Figure 7.13 Pd 3d spectra of the $CeO_{1.84}$/Rh(111) surface as increasing amounts of Pd are deposited at 300 K. Pd coverage is indicated on the figure in MLE.

Pd/$CeO_{1.71}$/Rh(111)

$CeO_{1.71}$ thin films were grown on Rh(111), by evaporating Ce onto Rh(111) in an oxygen pressure of 4.5×10^{-8} mbar, resulting in a film with a Ce^{3+} concentration of 57.7 ± 1.5%, as calculated from Ce 3d XP spectra. The effects of depositing Pd onto the surface were then studied. The Ce 3d XP spectra for the $CeO_{1.71}$/Rh(111) surface as increasing amounts of Pd are deposited are shown in Figure 7.14.

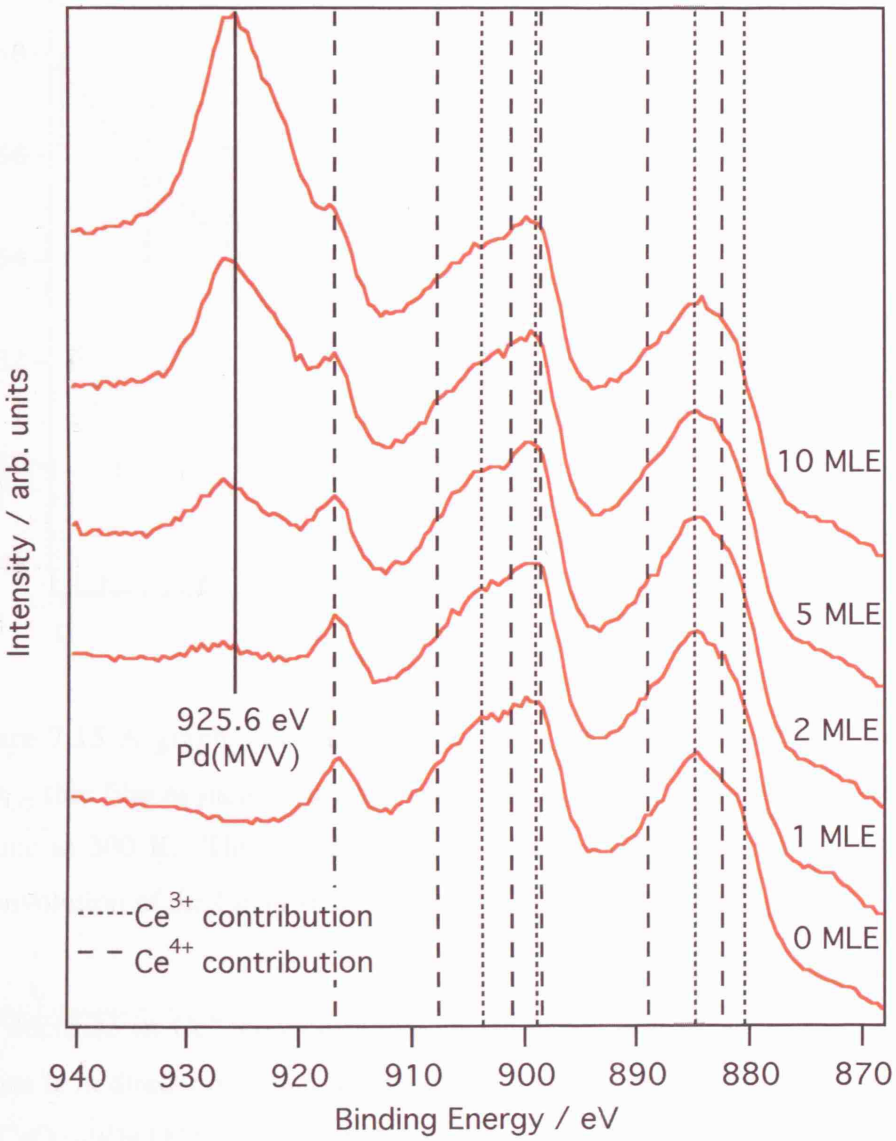

Figure 7.14 Ce 3d XP spectra of 3 MLE $CeO_{1.71}$/Rh(111) as increasing amounts of Pd are deposited onto the surface at 300 K.

By deconvoluting the Ce 3d spectra shown in Figure 7.14 the Ce^{3+} concentration of the $CeO_{1.71}$ thin film could then be calculated and plotted as a function of Pd coverage, as shown in Figure 7.15. It can clearly be seen from Figure 7.15 that the Ce^{3+} concentration of the $CeO_{1.71}$ thin film decreases as Pd coverage increases. The initial Ce^{3+} concentration of the thin film, before Pd deposition, was 57.7 ± 1.5%, and this decreases gradually with increasing Pd coverage, giving a Ce^{3+} concentration of 49.2 ± 1.5% following a 10 MLE Pd coverage.

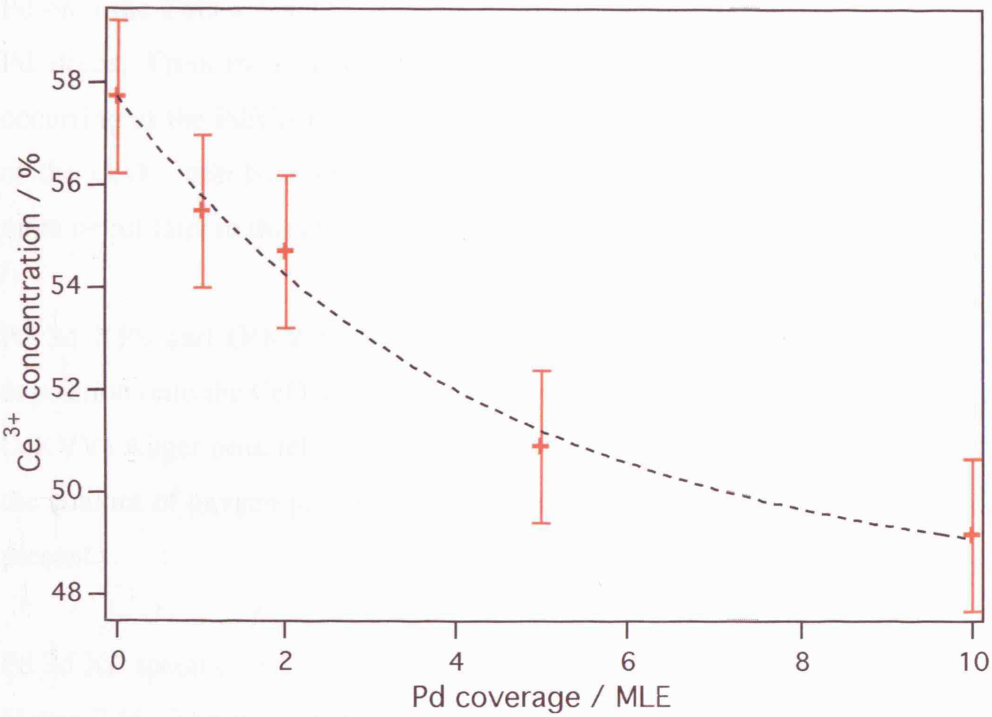

Figure 7.15 A graph showing the change in Ce^{3+} concentration of a 3 MLE $CeO_{1.71}$ thin film as increasing amounts of Pd are dosed onto the $CeO_{1.71}$/Rh(111) surface at 300 K. The percentage Ce^{3+} concentration has been calculated by deconvolution of the Ce 3d spectra into the 10 Gaussian contributions.

The decrease in Ce^{3+} concentration on Pd deposition on the $CeO_{1.71}$/Rh(111) surface is in direct contrast to observations made when depositing Pd on $CeO_{1.91}$ and $CeO_{1.84}$/Rh(111), where an increase in Ce^{3+} concentration was observed when Pd was evaporated onto the surface (Figure 7.8 and Figure 7.12). An increase in Ce^{3+} concentration was also observed in experiments by Pfau *et al.* [11], where Rh was deposited on stoichiometric CeO_2(111). The observations of Pfau *et al.*

are in agreement with those made in this study for Pd deposition on $CeO_{1.91}$/Rh(111) and $CeO_{1.84}$/Rh(111) surfaces. Consideration of other metal/oxide surfaces reveals that a decrease in Ti^{3+} concentration has been observed in experiments where Pt was deposited onto highly reduced, defect rich TiO_2(110) [12]. This was interpreted as an indication of electron transfer from localised Ti states to Pt atoms. This is in agreement with observations made when depositing Pd onto $CeO_{1.71}$/Rh(111) surfaces. Hence it is likely that the decrease in Ce^{3+} concentration observed when depositing increasing amounts of Pd onto the $CeO_{1.71}$/Rh(111) surface, is due to charge transfer from Ce^{3+} ions to Pd atoms. From the evidence presented thus far it appears that the mechanisms occurring at the Pd/CeO_{2-x} interface are highly dependent on the oxidation state of the CeO_{2-x} thin film and the presence of defects. This will be discussed in more detail later in this chapter.

Pd 3d XPS and O(KVV) Auger peaks have also been monitored during Pd deposition onto the $CeO_{1.71}$/Rh(111) surface. When the ratio of peak areas for the O(KVV) Auger peak relative to the Ce 3d XPS peak is calculated it is found that the amount of oxygen present remains constant independent of the amount of Pd present.

Pd 3d XP spectra for $CeO_{1.84}$/Rh(111) with increasing Pd coverage are shown in Figure 7.16. The Pd 3d binding energies remain constant, independent of the Pd coverage, at energies expected for bulk Pd.

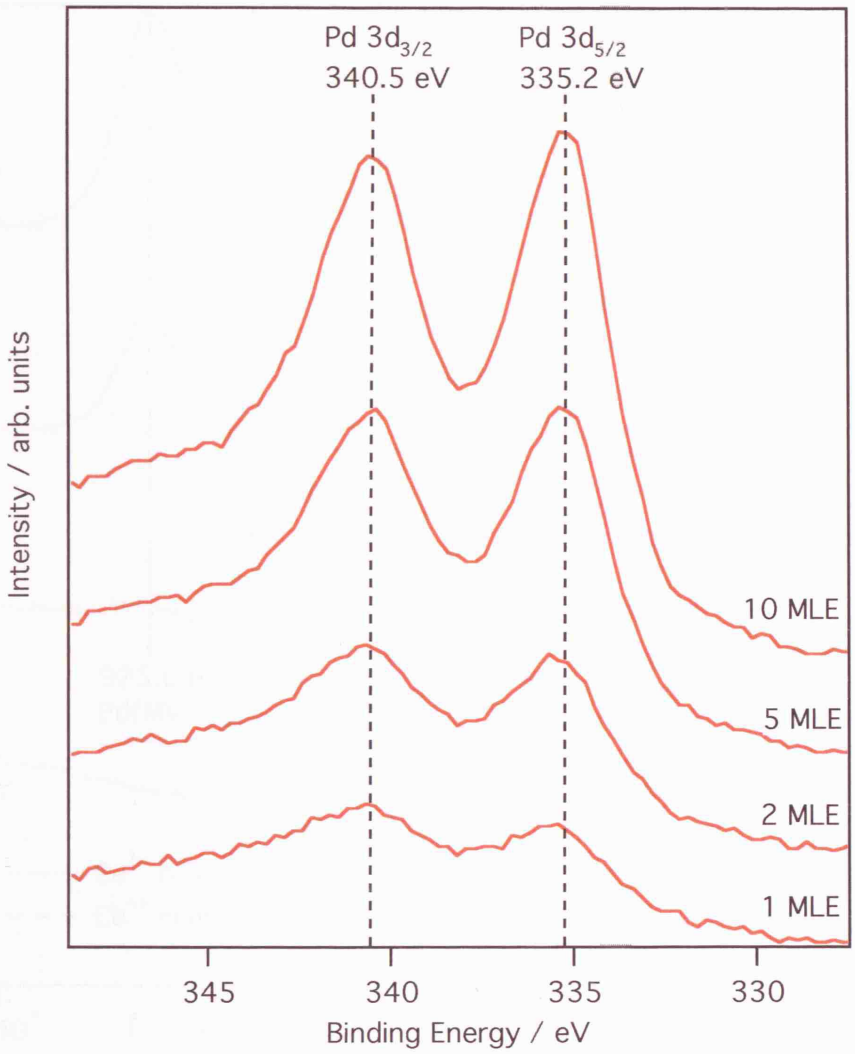

Figure 7.16 Pd $3d_{3/2,\ 5/2}$ XP spectra of $CeO_{1.71}$/Rh(111) as increasing amounts of Pd are deposited onto the surface at 300 K. Pd coverages are indicated on the graph in MLE.

Pd/$CeO_{1.61}$/Rh(111)

Figure 7.17 shows Ce 3d XP spectra for $CeO_{1.61}$/Rh(111) as increasing amounts of Pd are dosed onto the surface. A clear change in the Ce 3d peak shape can be observed as the Pd coverage is increased.

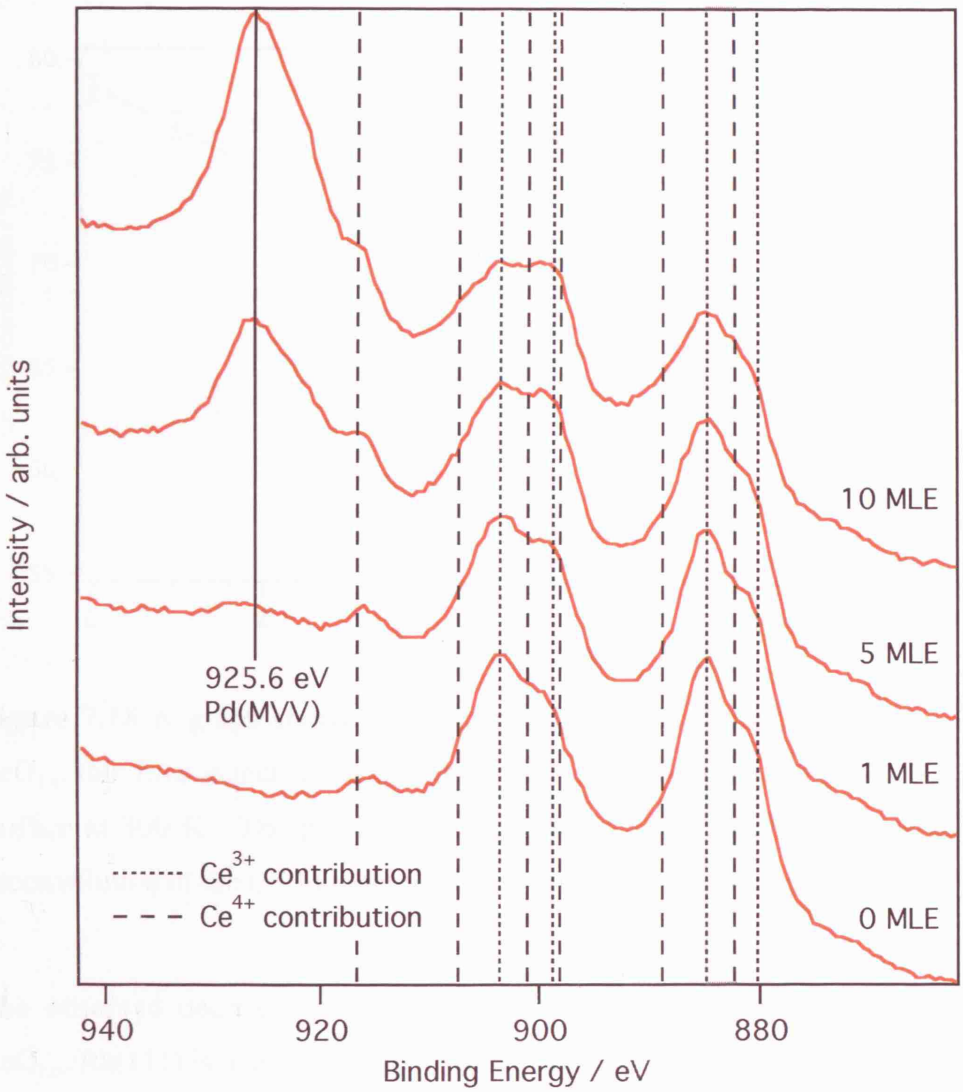

Figure 7.17 Ce 3d XP spectra of 3 MLE $CeO_{1.61}$/Rh(111) as increasing amounts of Pd are deposited onto the surface at 300 K. Pd coverage is indicated on the figure in MLE. Dashed lines indicate the location of Ce^{4+} related peaks, and dotted lines indicate Ce^{3+} related peaks.

The Ce^{3+} concentration of the CeO_{2-x} thin films was calculated by deconvoluting the Ce 3d spectra, shown in Figure 7.17, into the 10 Gaussian contributions. Figure 7.18 shows the change in Ce^{3+} concentration as a function of Pd coverage. It can clearly be seen that the Ce^{3+} concentration decreases linearly as the Pd coverage increases. The initial Ce^{3+} concentration of the $CeO_{1.61}$ thin film is 78.6 ± 0.6%, and this decreases by 20.6% to a value of 58.0 ± 0.6% after the deposition of 10 MLE Pd.

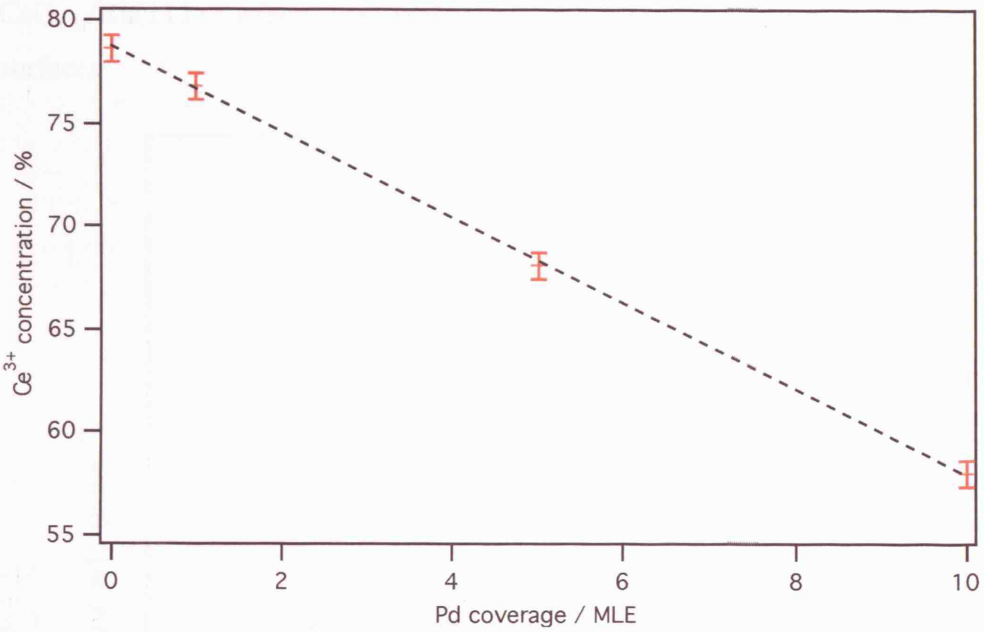

Figure 7.18 A graph showing the change in Ce^{3+} concentration of a 3 MLE $CeO_{1.61}$ thin film as increasing amounts of Pd are dosed onto the $CeO_{1.61}$/Rh(111) surface at 300 K. The percentage Ce^{3+} concentration has been calculated by deconvolution of the Ce 3d spectra into the 10 Gaussian contributions.

The observed decrease in Ce^{3+} concentration upon Pd deposition onto the $CeO_{1.61}$/Rh(111) is in agreement with observations made for the $CeO_{1.71}$ thin film. However the rate of decrease in Ce^{3+} concentration is different for the two surfaces. The total decrease in Ce^{3+} concentration is also notably larger for the $CeO_{1.61}$ thin film, where the Ce^{3+} concentration decreases by 20.6% on deposition of 10 MLE Pd, compared to an 8.5% decrease observed under the same conditions for $CeO_{1.71}$.

The Pd 3d XPS spectra were also monitored. Figure 7.19 shows Pd 3d spectra of the $CeO_{1.61}$/Rh(111) surface as a function of changing Pd coverage. The Pd 3d binding energies have been plotted as a function of Pd coverage in Figure 7.20 and it can clearly be seen that as the Pd coverage is increased the binding energies of both Pd 3d peaks decrease closer to values expected for bulk Pd [10]. This is in contrast to observations made for Pd deposition on less reduced CeO_{2-x} surfaces (Figure 7.10, Figure 7.13, and Figure 7.16). This is thought to be due to

the deposited Pd being more dispersed at lower Pd coverages on the $CeO_{1.61}$/Rh(111) surface, compared to the more highly oxidised CeO_{2-x}/Rh(111) surfaces.

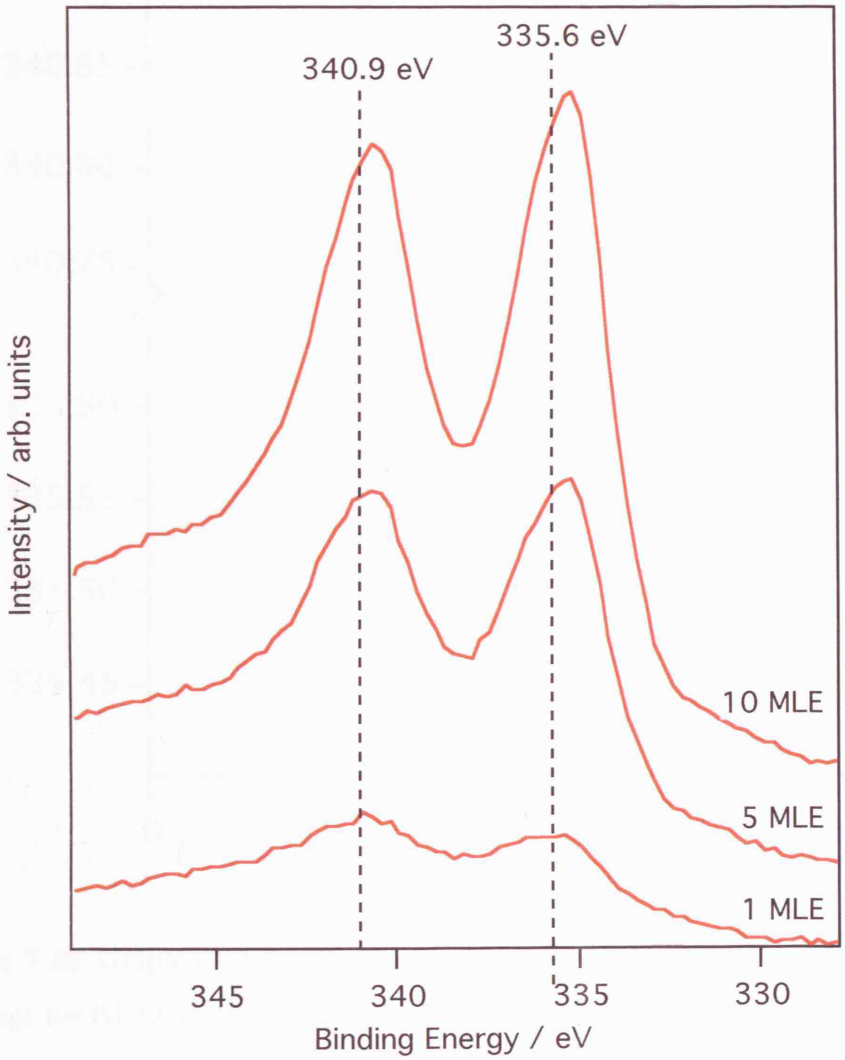

Figure 7.19 Pd $3d_{3/2, 5/2}$ XP spectra of $CeO_{1.61}$/Rh(111) as increasing amounts of Pd are deposited onto the surface at 300 K. Pd coverages are indicated on the graph in MLE.

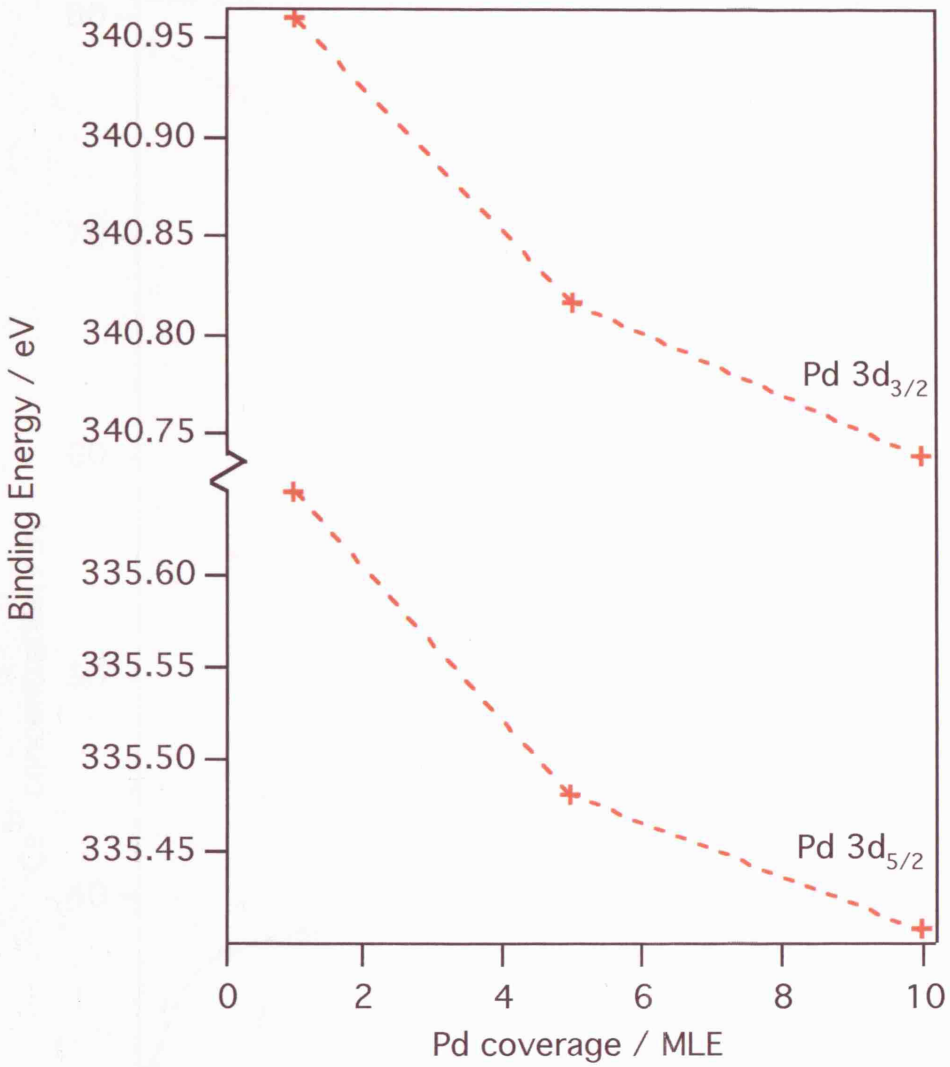

Figure 7.20 Graph showing the change in binding energy with increasing Pd coverage for Pd $3d_{3/2}$ and Pd $3d_{5/2}$ XPS peaks.

Summary

To summarise, the effect of dosing Pd onto CeO_{2-x}/Rh(111) is highly dependent on the initial oxidation state of the CeO_{2-x} thin films. For both $CeO_{1.91}$ and $CeO_{1.84}$ thin films an increase in Ce^{3+} concentration was observed, whereas for $CeO_{1.71}$ and $CeO_{1.61}$ thin films a decrease in Ce^{3+} concentration was observed as the Pd coverage was increased. This is shown in Figure 7.21, where the Ce^{3+} concentration is plotted as a function of Pd coverage for all 4 surfaces studied.

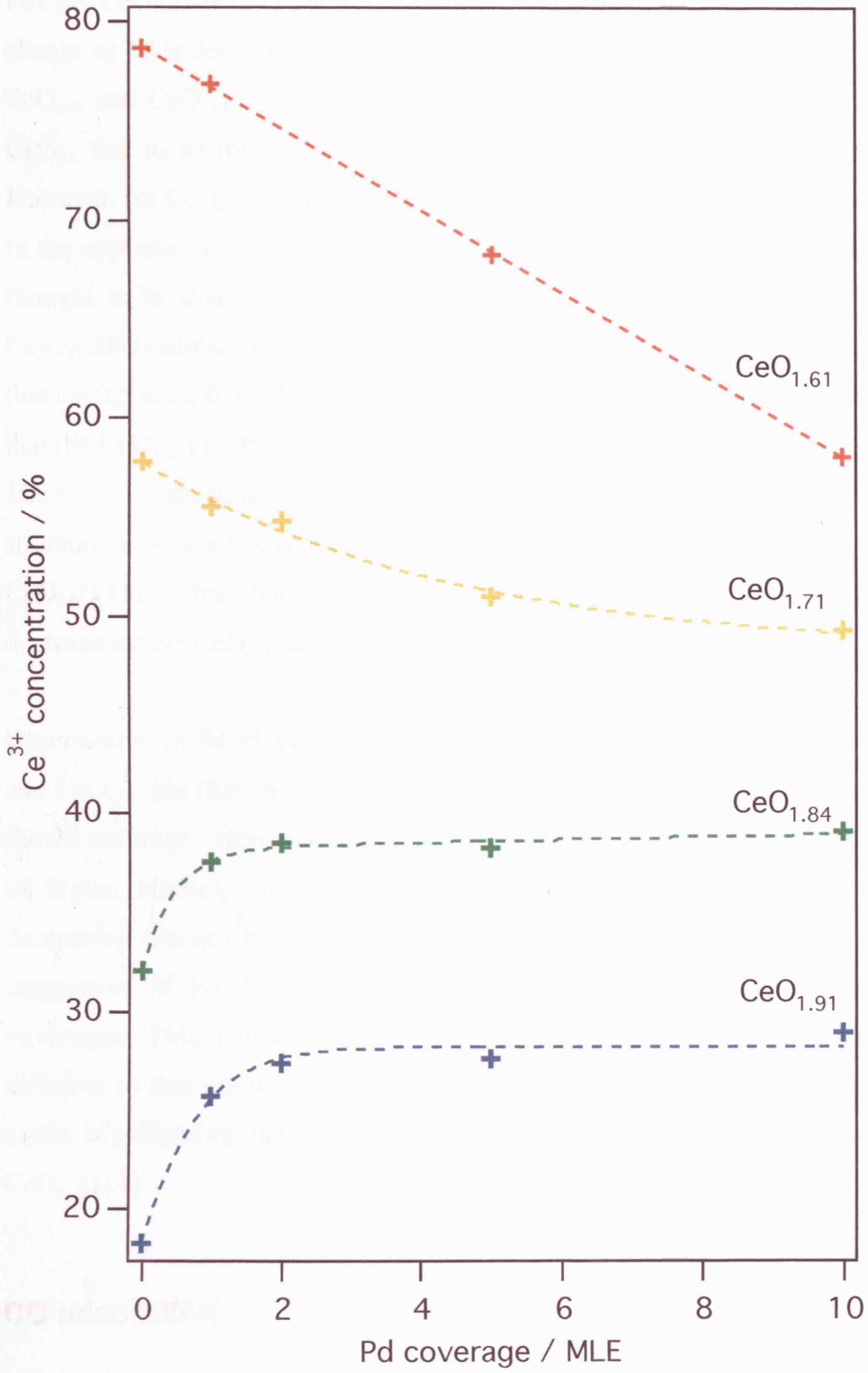

Figure 7.21 A graph comparing the effect of Pd coverage on the Ce^{3+} concentration of CeO_{2-x} thin films grown on Rh(111), for CeO_{2-x} films with different oxidation states.

For all CeO_{2-x}/Rh(111) surfaces studied, it is thought that the cause of Ce^{3+} change as Pd is deposited is charge transfer between the CeO_{2-x} and the Pd. For $CeO_{1.91}$ and $CeO_{1.84}$ thin films the charge transfer would be from the Pd to the CeO_{2-x} due to an increase in Ce^{3+} concentration with increasing Pd coverage. However, for $CeO_{1.71}$ and $CeO_{1.61}$ thin films the charge transfer would have to be in the opposite direction. The cause for this obvious difference in behaviour is thought to be that the $CeO_{1.71}$ and $CeO_{1.61}$ thin films are exhibiting areas of $Ce_2O_3(0001)$ surface structure. X-ray diffraction studies of CeO_{2-x} crystals show that for $0.5 \leq x \leq 0.3$, a hexagonal Ce_2O_3 structure is observed [9]. This suggests that the $CeO_{1.61}$ ($x = 0.39$) thin film most likely exhibits a $Ce_2O_3(0001)$ structure. The $CeO_{1.71}$ thin film ($x = 0.29$) could also exhibit some areas of $Ce_2O_3(0001)$ structure, however it is possible that some areas of the ceria surface could also be $CeO_{2-x}(111)$. This could explain the difference in rate of Ce^{3+} concentration decrease for the $CeO_{1.71}$ and $CeO_{1.61}$ thin films on Pd deposition.

Observations of Pd 3d XPS have shown that Pd deposited on the $CeO_{1.91}$, $CeO_{1.84}$ and $CeO_{1.71}$ thin films has binding energies expected for bulk Pd, independent of the Pd coverage. However Pd 3d XPS of Pd/$CeO_{1.61}$/Rh(111) show Pd 3d peaks of higher binding energies at low Pd coverage, with the binding energy decreasing towards bulk Pd values as the Pd coverage is increased. This is suggestive of Pd dispersal over the $CeO_{1.61}$/Rh(111) surface for low Pd coverages. This indicates that the Pd growth mode on the $CeO_{1.61}$ thin film is different to that observed on the $CeO_{1.91}$, $CeO_{1.84}$ and $CeO_{1.71}$ thin films, once again highlighting the different behaviour of $Ce_2O_3(0001)$, compared to $CeO_{2-x}(111)$.

CO adsorption

CO/Pd/$CeO_{1.91}$/Rh(111)

CO was dosed to a saturation exposure of 100 L, as determined by C 1s XPS, onto $CeO_{1.91}$/Rh(111) surfaces with 0, 1, 5, and 10 MLE Pd coverages. Analysis of the Ce 3d spectra of these surfaces before and after CO exposure has shown that there was no change in the Ce^{3+} concentration on CO adsorption.

C 1s XP spectra of CO saturation of $CeO_{1.91}$/Rh(111) surfaces with 0, 1, 5, and 10 MLE Pd coverages are shown in Figure 7.22. It can be seen that there is no C 1s peak when there is no Pd present, and then after deposition of 1 MLE Pd a small, single C 1s peak appears, which increases in intensity as the Pd coverage is increased. The lack of C 1s peak when there is no Pd present indicates that CO is not adsorbing on the $CeO_{1.91}$ sites. This is in agreement with theoretical investigations carried out by Nolan *et al.* [13, 14] who studied CO adsorption on ceria surfaces using DFT calculations. They concluded that there is only a very weak interaction between adsorbed CO and CeO_2(111), which is consistent with results from the present study.

The C 1s spectrum for CO adsorbed onto the clean Rh(111) crystal has also been included in Figure 7.22 for reference. There appears to be a single peak with a binding energy of approximately 286 eV. In XPS studies of CO adsorption on Rh(111) at 300 K [15] the C 1s spectrum consists of two Gaussian peaks at binding energies of 286.0 eV and 285.4 eV due to CO adsorbed in atop and threefold hollow sites respectively. The binding energy of the C 1s peak observed in this study is consistent with those observed in the previous study. However, in the present study the resolution of the XP spectrum is not sufficient to identify two separate peaks, and after Shirley background subtraction the spectrum can be satisfactorily fitted with a single Gaussian.

From XPS studies alone it is impossible to tell whether the CeO_{2-x} has formed in a wetting layer on the Rh(111), or whether islands have formed leaving bare Rh(111) sites. The expected C 1s peaks due to CO adsorption on Pd and Rh are also too close in binding energy to be able to differentiate between them using the C 1s spectra shown in Figure 7.22. However, previous STM studies of CeO_{2-x}/Rh(111) [2] using the same CeO_{2-x} growth method have shown that the Rh surface was completely covered after the deposition of a two layer oxide. As the CeO_2 film thickness was increased, three dimensional islands of CeO_2 were observed, exhibiting some crystalline order within the island structures [2]. This suggests that for the three layer oxides used in this study there should be no bare

Rh sites remaining, and therefore all C 1s peaks observed (Figure 7.22) are due to CO adsorption on the deposited Pd clusters.

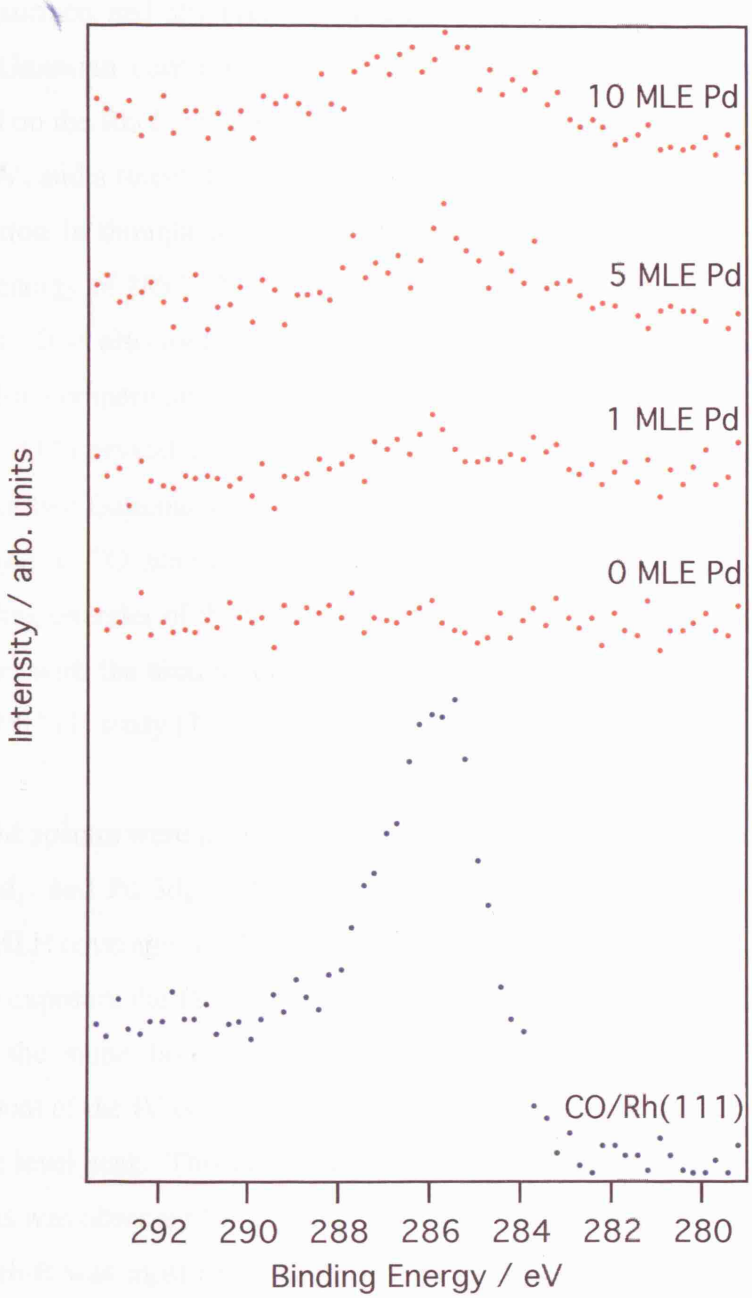

Figure 7.22 C 1s XPS difference spectra (CO-dosed – undosed) of $Pd/CeO_{1.91}/Rh(111)$ surfaces as a function of Pd coverage, after the surface has been exposed to 100 L CO at room temperature. The bottom C 1s difference spectrum is of Rh(111) after 100 L CO exposure at room temperature. All spectra have been taken under identical conditions and are offset for clarity.

Beutler *et al.* [7] have studied the interaction of CO with a 0.5 ML Pd/Rh(111) surface. They recorded C 1s spectra as increasing amounts of CO were dosed onto the surface, and observed broad peaks which can be deconvoluted into three distinct Gaussian contributions. Two of the Gaussian peaks are due to CO adsorbed on the Rh(111) surface, with an atop component at a binding energy of 286.07 eV, and a threefold hollow component at 285.35 eV. The third Gaussian contribution is thought to be due to CO adsorbed on Pd, and has an initial binding energy of 285.7 eV, which increases slightly as the amount of CO dosed increases. It is also useful to consider studies of CO adsorbed onto a Pd(111) surface for comparison. Surnev *et al.* [16] have studied CO adsorption on a clean Pd(111) crystal using XPS. They have found that the C 1s spectrum consists of two Gaussian contributions at binding energies of 285.5 eV and 285.7 eV relating to CO adsorbed in threefold hollow and bridge sites respectively. The binding energies of the C 1s peaks found in the CO/Pd(111) study [16] are in agreement with the binding energy found for the Pd-related peak in the CO/0.5 ML Pd/Rh(111) study [7].

The Pd 3d spectra were also monitored during CO exposure. Figure 7.23 shows the Pd $3d_{3/2}$ and Pd $3d_{5/2}$ XP spectra for the $CeO_{1.91}$/Rh(111) sample, with 1, 5, and 10 MLE coverages of Pd, before and after CO exposure. It can be seen that after CO exposure the Pd 3d peaks have shifted 0.3 eV to higher binding energy. Exactly the same binding energy shift was observed after CO exposure independent of the Pd coverage, where all binding energies are referred to the Rh $3d_{5/2}$ core level peak. This is exactly the same CO induced shift in Pd 3d binding energy, as was observed for Pd/$CeO_{1.91}$/Pt(111) (chapter 6), where it was deduced that the shift was most likely due to reduced final state screening in the metal nanoparticles on the oxide.

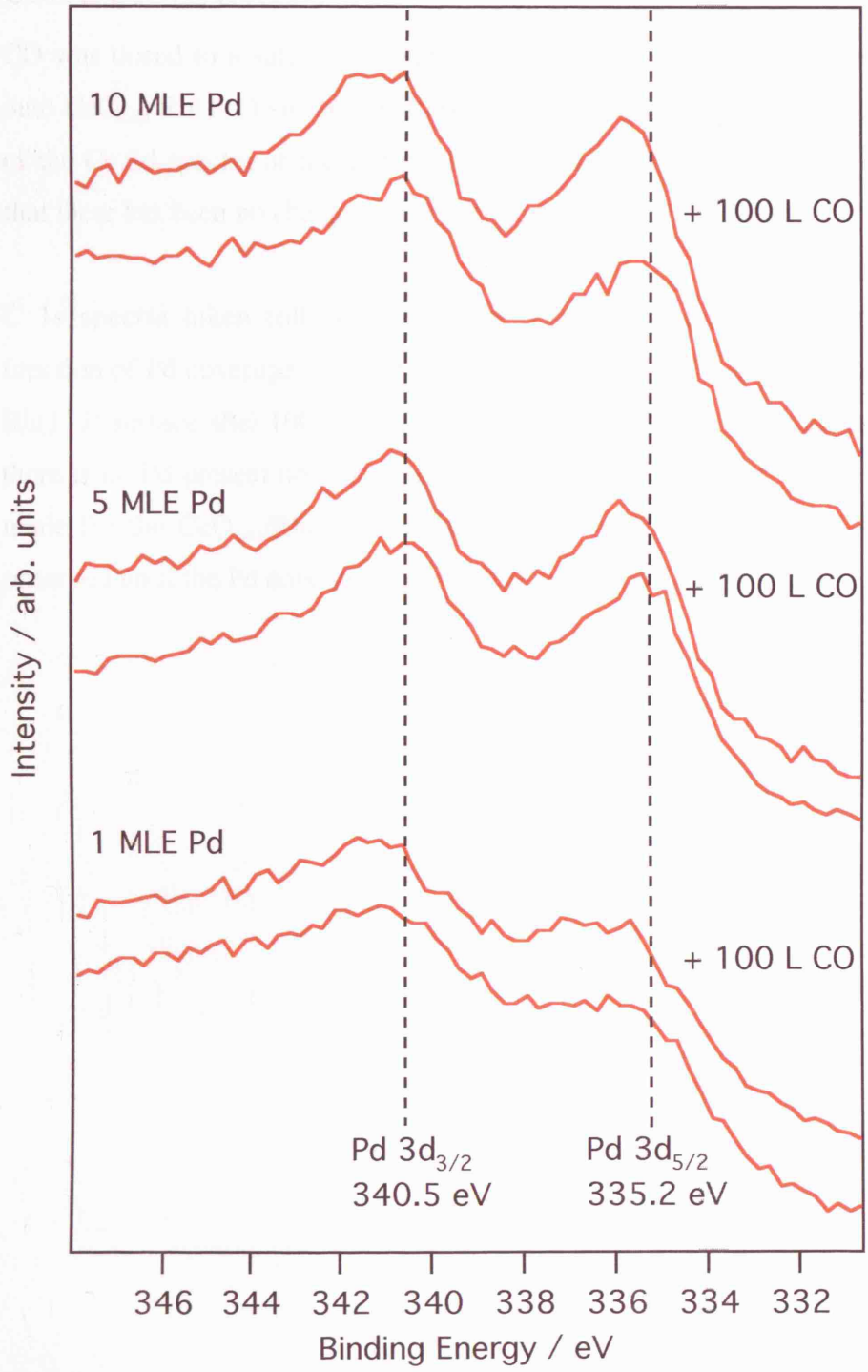

Figure 7.23 Pd $3d_{3/2,5/2}$ XPS spectra of 1 MLE Pd, 5 MLE Pd, and 10 MLE Pd/$CeO_{1.91}$/Rh(111) before and after 100 L CO exposure at room temperature. Before CO exposure the binding energies of the Pd $3d_{3/2}$ and Pd $3d_{5/2}$, peaks were constant for all surfaces, at 340.5 eV and 335.2 eV respectively. All spectra have been taken under identical conditions and are offset for clarity.

CO/Pd/$CeO_{1.84}$/Rh(111)

CO was dosed to a saturation exposure of 100 L, as determined by C 1s XPS, onto $CeO_{1.84}$/Rh(111) surfaces with 0, 1, 5, and 10 MLE Pd coverages. Analysis of the Ce 3d spectra of these surfaces before and after CO exposure has shown that there has been no change in Ce^{3+} concentration on CO adsorption.

C 1s spectra taken following 100 L CO exposure to $CeO_{1.84}$/Rh(111) as a function of Pd coverage are shown in Figure 7.24. The C 1s spectrum of a clean Rh(111) surface after 100 L CO exposure is also included for comparison. When there is no Pd present no C 1s peak is observed, in agreement with observations made for the $CeO_{1.91}$/Rh(111) surface (Figure 7.22). In fact, no C 1s peak is observed until the Pd coverage is increased to 10 MLE (Figure 7.24).

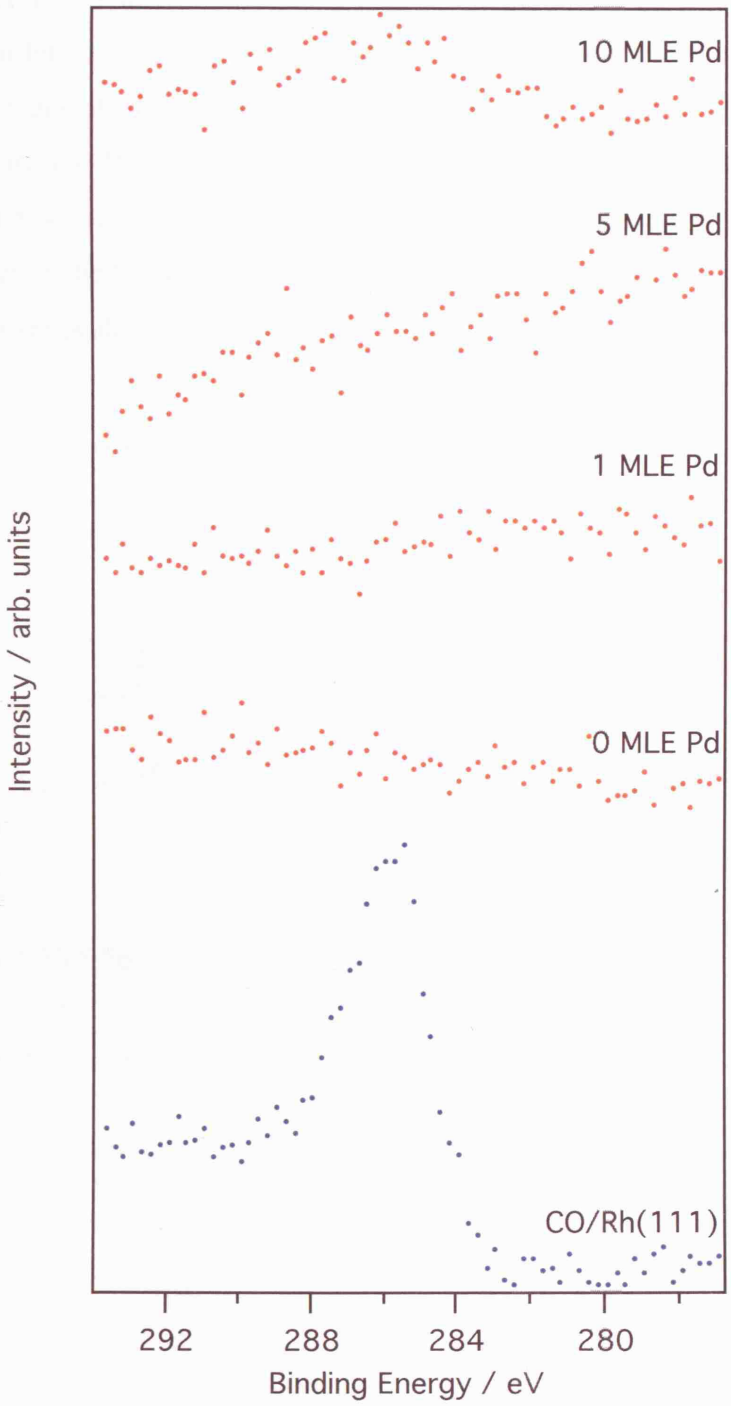

Figure 7.24 C 1s XPS difference spectra (CO-dosed – undosed) of $Pd/CeO_{1.84}/Rh(111)$ surfaces as a function of Pd coverage, after the surface has been exposed to 100 L CO at room temperature. The bottom C 1s difference spectrum is of Rh(111) after 100 L CO exposure at room temperature. All spectra have been taken under identical conditions and are offset for clarity.

Pd 3d spectra were also monitored during CO exposure. Figure 7.25 shows the Pd $3d_{3/2}$ and Pd $3d_{5/2}$ XP spectra for the $CeO_{1.84}$/Rh(111) sample, with 1, 5, and 10 MLE coverages of Pd, before and after CO exposure. It can be seen that after CO exposure the Pd 3d peaks have shifted 0.2 eV to higher binding energy. Exactly the same binding energy shift was observed after CO exposure independent of the Pd coverage, where all binding energies are referred to the Rh $3d_{5/2}$ core level peak.

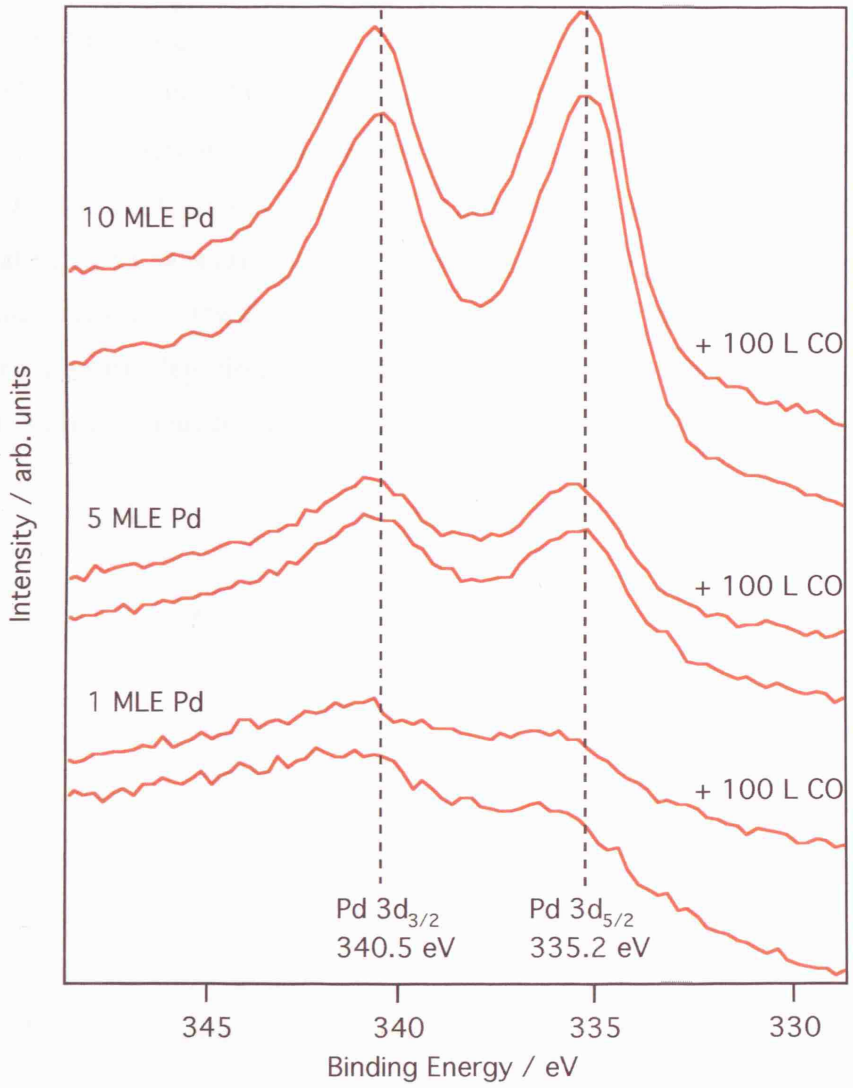

Figure 7.25 Pd $3d_{3/2,5/2}$ XPS spectra of 1 MLE Pd, 5 MLE Pd, and 10 MLE Pd/$CeO_{1.84}$/Rh(111) before and after 100 L CO exposure at room temperature. Before CO exposure the binding energies of the Pd $3d_{3/2}$ and Pd $3d_{5/2}$, peaks were constant for all surfaces at 340.5 eV and 335.2 eV respectively. All spectra have been taken under identical conditions and are offset for clarity.

CO/Pd/$CeO_{1.61}$/Rh(111)

CO was dosed to a saturation exposure of 100 L, as determined by C 1s XPS, onto $CeO_{1.61}$/Rh(111) surfaces with 0, 1, 5, and 10 MLE Pd coverages. Analysis of the Ce 3d spectra of these surfaces before and after CO exposure shows that there is no change in Ce^{3+} concentration on CO adsorption.

C 1s spectra taken following 100 L CO exposure to $CeO_{1.61}$/Rh(111) as a function of Pd coverage are shown in Figure 7.26. The C 1s spectrum of a clean Rh(111) surface after 100 L CO exposure is also included for comparison. When there is no Pd present no C 1s peak is observed, in agreement with observations made for the $CeO_{1.91}$ and $CeO_{1.84}$/Rh(111) surfaces (Figure 7.22 and Figure 7.24), indicating that CO is not adsorbing on CeO_{2-x} at room temperature, independent of oxidation state. The C 1s spectrum for CO adsorption on the $CeO_{1.61}$/Rh(111) surface after the deposition of 1 MLE Pd shows a small C 1s peak (Figure 7.26). The C 1s peak intensity increases as the amount of Pd present is increased.

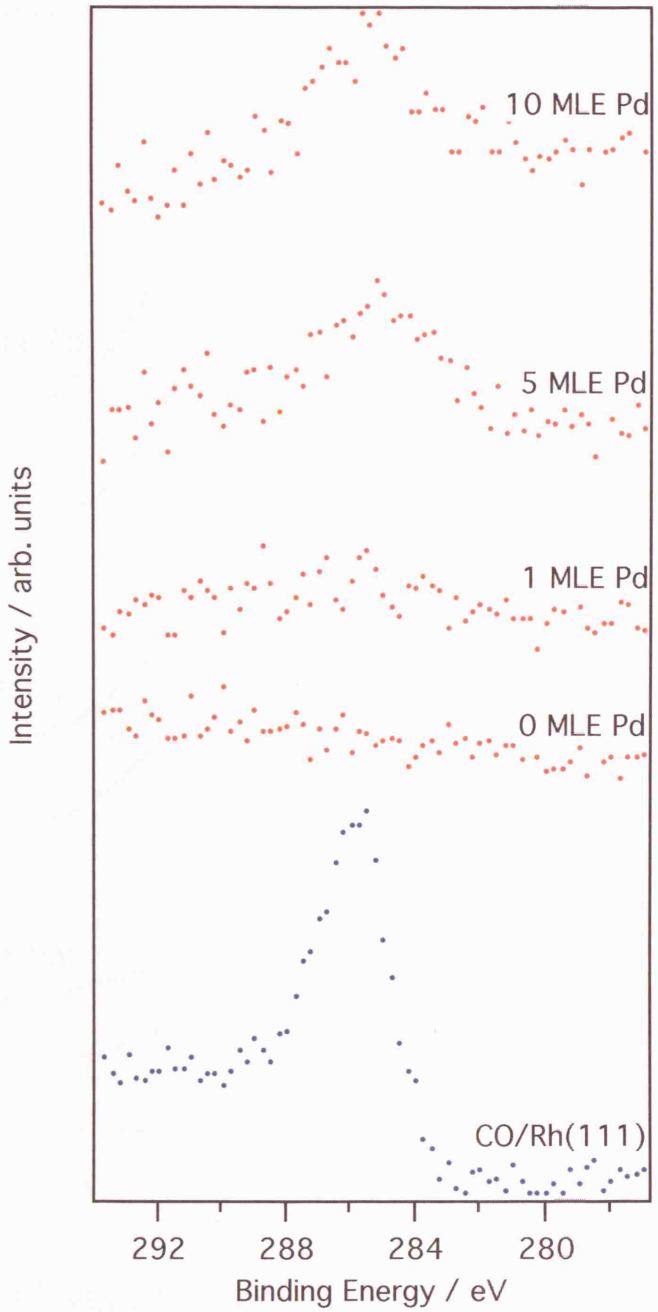

Figure 7.26 C 1s XPS difference spectra (CO-dosed – undosed) of $Pd/CeO_{1.61}/Rh(111)$ surfaces as a function of Pd coverage, after the surface has been exposed to 100 L CO at room temperature. The bottom C 1s difference spectrum is for Rh(111) after 100 L CO exposure at room temperature. All spectra have been taken under identical conditions and are offset for clarity.

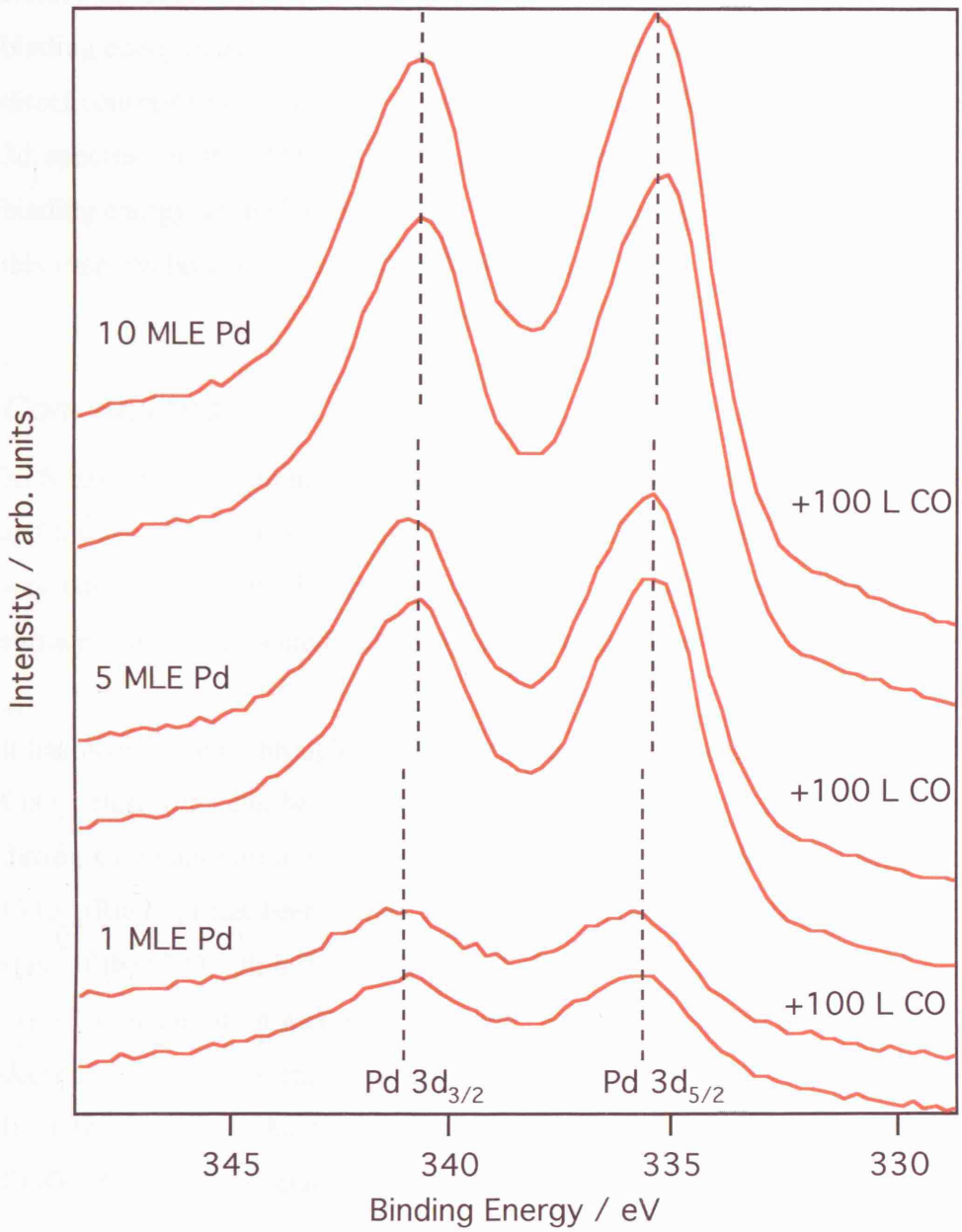

Figure 7.27 Pd $3d_{3/2,5/2}$ XPS spectra of 1 MLE Pd, 5 MLE Pd, and 10 MLE Pd/$CeO_{1.61}$/Rh(111) before and after 100 L CO exposure at room temperature. All spectra have been taken under identical conditions and are offset for clarity.

The Pd 3d spectra were also monitored during CO exposure. Figure 7.27 shows the Pd $3d_{3/2}$ and Pd $3d_{5/2}$ XP spectra for the $CeO_{1.91}$/Rh(111) sample, with 1, 5, and 10 MLE coverages of Pd, before and after CO exposure. As discussed previously the Pd 3d binding energy increases as increasing amounts of Pd are deposited onto the $CeO_{1.61}$/Rh(111) surface (Figure 7.20). However, it can

clearly be seen that after CO exposure the Pd 3d peaks remain at the same binding energies as before CO exposure, independent of Pd coverage. This is in direct contrast to observations made for $CeO_{1.91}$ and $CeO_{1.84}$ thin films, where Pd 3d spectra for the $Pd/CeO_{2-x}/Rh(111)$ surfaces showed an increase in Pd 3d binding energy upon CO adsorption. The lack of change in the binding energy in this case has been attributed to the dispersal of Pd.

Conclusions

XPS has been used to investigate the growth of ceria ultrathin films on Rh(111) and the modification of these films by Pd and CO adsorption. In particular, XPS was employed to provide information about the oxidation state of the CeO_{2-x} surface, and how it is modified by the presence of Pd and CO.

It has been shown, through the use of Ce 3d XPS, that the Ce^{3+} concentration of CeO_{2-x} thin films can be altered by up to 60% by changing the oxygen pressure during Ce evaporation onto the Rh(111) surface. The effect of dosing Pd onto $CeO_{2-x}/Rh(111)$ has been shown to be highly dependent on the initial oxidation state of the CeO_{2-x} thin films. For both $CeO_{1.91}$ and $CeO_{1.84}$ thin films an increase in Ce^{3+} concentration was observed, whereas for $CeO_{1.71}$ and $CeO_{1.61}$ thin films a decrease in Ce^{3+} concentration was observed, as the Pd coverage was increased. It is thought that the more highly reduced ceria thin films exhibit some $Ce_2O_3(0001)$ surface structure, which modifies the growth of the Pd.

When CO is dosed onto the $Pd/CeO_{2-x}/Rh(111)$ surface the C 1s XPS peak increases in intensity as the amount of Pd present increases, independent of the initial Ce^{3+} concentration. The binding energy of the C 1s peak also remains constant independent of Pd coverage, in agreement with SXPS studies of CO adsorption on Rh/CeO_x at 300 K [17]. There is no change in Ce^{3+} concentration on CO adsorption. A small shift in binding energy of the Pd 3d XPS peaks is observed on CO adsorption onto Pd deposited on $CeO_{2-x}/Rh(111)$ for CeO_{2-x} thin films with lower Ce^{3+} concentrations, possibly due to reduced final state screening in the metal nanoparticles adsorbed on the oxide [18]. However, there

is no shift in Pd 3d binding energy on CO adsorption on $Pd/CeO_{1.61}/Rh(111)$, possibly due to Pd dispersal over the surface.

References

1. Hardacre, C., Ormerod, R.M., and Lambert, R.M., *Platinum promoted catalysis by ceria: a study of carbon monoxide oxidation over $Pt(111)/CeO_2$*. J. Phys. Chem., 1994. **98**: p. 10901.
2. Eck, S., Castellarin-Cudia, C., Surnev, S., Ramsey, M.G., and Netzer, F.P., *Growth and thermal properties of ultrathin cerium oxide layers on Rh(111)*. Surf. Sci., 2002. **520**(3): p. 173.
3. Castellarin-Cudia, C., Surnev, S., Schneider, G., Podlucky, R., Ramsey, M.G., and Netzer, F.P., *Strain-induced formation of arrays of catalytically active sites at the metal-oxide interface*. Surf. Sci. Lett., 2004. **554**: p. L120.
4. Eck, S., Castellarin-Cudia, C., Surnev, S., Prince, K.C., Ramsey, M.G., and Netzer, F.P., *Adsorption and reaction of CO on a ceria-Rh(111) "inverse model catalyst" surface*. Surf. Sci., 2003. **536**(1-3): p. 166.
5. Belton, D. and Schmieg, S., *Low temperature oxidation and reduction of ceria particles on Rh(111)*. J. Vac. Sci. Technol. A, 1993. **11**: p. 2330.
6. Seah, M.P., *Quantification of AES and XPS*, in *Practical Surface Analysis - Auger and X-ray Photoelectron Spectroscopy*, D. Briggs and M.P. Seah, Editors. 1983, Wiley. p. 201.
7. Beutler, A., Strisland, F., Sandell, A., Jaworowski, A.J., Nyholm, R., Wiklund, M., and Andersen, J.N., *Adsorption properties of a mixed surface studied by high resolution core level photoemission: CO/0.5 ML Pd/Rh(111)*. Surf. Sci., 1998. **411**(1-2): p. 111.
8. Xiao, W., Guo, Q., and Wang, E.G., *Transformation of $CeO_2(111)$ to $Ce_2O_3(0001)$ films*. Chemical Physics Letters, 2003. **368**(5-6): p. 527.
9. Knappe, P. and Eyring, L., *Preparation and electron microscopy of intermediate phases in the interval Ce7O12---Ce11O20*. Journal of Solid State Chemistry, 1985. **58**(3): p. 312.
10. Thompson, A., Attwood, D., Gullikson, E., Howells, M., Kim, K., Kirz, J., Kortright, J., Lindau, I., Pianetta, P., Robinson, A., Scofield, J., Underwood, J., Vaughan, D., Williams, G., and Winick, H., *X-ray data*

booklet. 2nd ed. 2001, California: Lawrence Berkeley National Laboratory.

11. Pfau, A., Schierbaum, K.D., and Gopel, W., *The electronic structure of CeO_2 thin films: the influence of Rh surface dopants*. Surf. Sci., 1995. **331-333**: p. 1479.
12. Schierbaum, K.D., Fischer, S., Torquemada, M.C., de Segovia, J.L., Roman, E., and Martin-Gago, J.A., *The interaction of Pt with TiO_2(110) surfaces: a comparative XPS, UPS, ISS, and ESD study*. Surf. Sci., 1996. **345**(3): p. 261.
13. Nolan, M., Parker, S.C., and Watson, G.W., *Vibrational properties of CO on ceria surfaces*. Surf. Sci., 2006. **600**(14): p. 175.
14. Nolan, M. and Watson, G.W., *The surface dependence of CO adsorption on Ceria*. J. Phys. Chem. B, 2006. **110**: p. 16600.
15. Beutler, A., Lundgren, E., Nyholm, R., Andersen, J.N., Setlik, B.J., and Heskett, D., *Coverage- and temperature-dependent site occupancy of carbon monoxide on Rh(111) studied by high-resolution core-level photoemission*. Surf. Sci., 1998. **396**(1-3): p. 117.
16. Surnev, S., Sock, M., Ramsey, M.G., Netzer, F.P., Wiklund, M., Borg, M., and Andersen, J.N., *CO adsorption on Pd(111): a high-resolution core level photoemission and electron energy loss spectroscopy study*. Surf. Sci., 2000. **470**(1-2): p. 171.
17. Mullins, D.R., Kundakovic, L., and Overbury, S.H., *The interaction between NO and CO on Rh-loaded CeO_x(111)*. J. Catal., 2000. **195**: p. 169.
18. Mullins, D.R., *Reactions on model emission control catalysts studied by soft X-ray photoemission*. J. Electron Spectrosc. Relat. Phenom., 2001. **114**: p. 333.

Chapter 8 : Comparison of CeO_{2-x}/Pt(111) and CeO_{2-x}/Rh(111) surfaces

Introduction

In this chapter the results presented thus far will be summarised and XPS results for CeO_{2-x} grown on Rh(111) and Pt(111) substrates will be compared to determine if the substrate is having any effect on the chemical behaviour of the ceria thin films. Typically previous studies, where the effect of the substrate was of interest, are of inverse model catalyst surfaces, where submonolayer quantities of a metal oxide are deposited on a noble metal single crystal, leaving bare substrate sites [1]. In studies where a number of monolayers of oxide are deposited on a substrate with no bare sites remaining it is generally assumed that the substrate has no effect on the oxide behaviour [2, 3].

In this study a CeO_{2-x} film thickness of 3 MLE was used for CeO_{2-x} thin films grown on both the Pt(111) and Rh(111) substrates. STM studies of CeO_{2-x} growth on Rh(111) [4] show that no bare substrate sites remain after deposition of a 2 layer oxide, and that as the CeO_{2-x} coverage is increased irregularly shaped, three dimensional islands are observed. STM studies of CeO_{2-x} thin films on Pt(111) [5], grown using the same method employed in this study, show that bare Pt(111) remains. This is in agreement with the RAIRS study of CO adsorption on a CeO_{2-x}/Pt(111) surface presented in chapter 5, where peaks attributed to CO-Pt(111) atop and bridge modes are observed. By comparing the areas under CO-Pt(111) atop peaks before and after CeO_{2-x} deposition onto a clean Pt(111) crystal, it was estimated that 17 ± 2% of the surface was bare Pt(111).

Pd deposition on CeO_{2-x} thin films

In chapters 6 and 7, Pd deposition on CeO_{2-x} thin films, grown on Pt(111) and Rh(111) substrates respectively, have been studied using XPS. The Ce^{3+} concentration of the CeO_{2-x} thin films was calculated using Ce 3d XPS, and

monitored during Pd deposition. On Pd deposition onto $CeO_{1.91}$ and $CeO_{1.84}$ thin films an increase in Ce^{3+} concentration is observed, independent of the substrate used. In both cases this increase in Ce^{3+} concentration was attributed to charge transfer from the Pd nanoparticles to the CeO_{2-x} (see chapters 6 and 7).

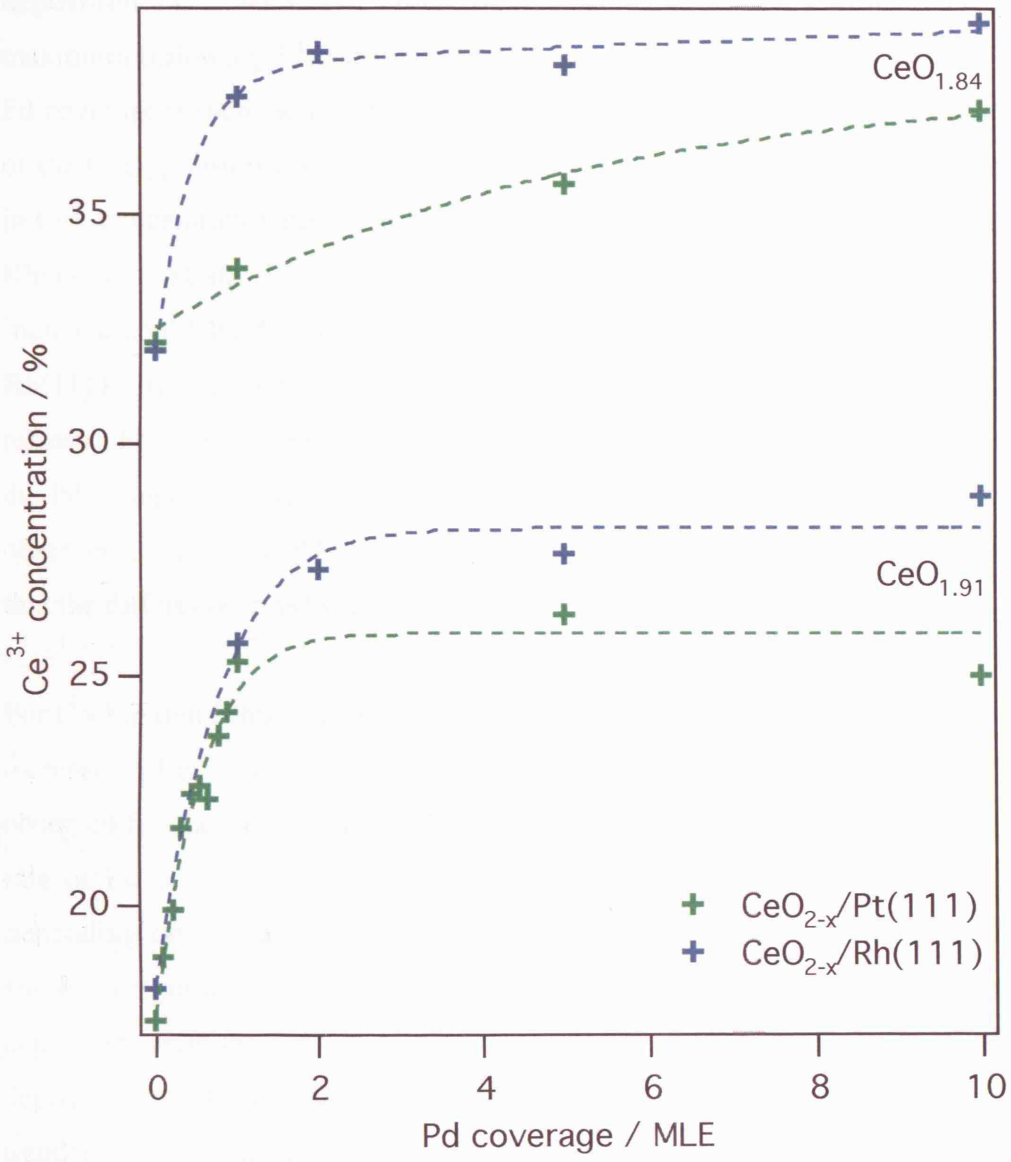

Figure 8.1 A graph showing the change in Ce^{3+} concentration of 3 MLE $CeO_{1.91}$ and $CeO_{1.84}$ thin films grown on Pt(111) and Rh(111), as a function of Pd coverage. Data points for the CeO_{2-x}/Pt(111) surfaces are shown in green, and data points for the CeO_{2-x}/Rh(111) surfaces are shown in blue. The percentage Ce^{3+} concentration has been calculated from deconvolution of the Ce 3d spectra into the 10 Gaussian contributions. Pd was deposited at room temperature.

Figure 8.1 shows the change in Ce^{3+} concentration as a function of Pd coverage for $CeO_{1.91}$ and $CeO_{1.84}$ thin films grown on Rh(111) and Pt(111). For $CeO_{1.91}$ thin films, a very similar pattern of behaviour can be observed independent of the substrate used. In both cases a rapid increase in Ce^{3+} concentration is observed on deposition of 1 MLE Pd, however the Ce^{3+} concentration then reaches a maximum following 2 MLE Pd deposition and remains at a constant level as the Pd coverage is increased to 10 MLE. The only difference between the behaviour of the $CeO_{1.91}$ thin films grown on Pt(111) and Rh(111) is that the total increase in Ce^{3+} concentration observed was slightly larger for the thin film grown on the Rh(111) substrate (Figure 8.1). This slight difference in Ce^{3+} concentration increase could be due to the fact that the $CeO_{1.91}$ thin film covers the entire Rh(111) surface, whereas when Pt(111) is used as the substrate bare Pt(111) sites remain. This would result in a smaller area of $CeO_{1.91}$ and would lead to some of the Pd being deposited on the bare Pt(111). However, the almost identical trends observed suggest that Pd is exhibiting the same growth mode in both cases, and that the difference in substrate is having very little effect on this.

For $CeO_{1.84}$ thin films grown on Pt(111) and Rh(111) substrates, a less substantial increase in Ce^{3+} concentration is observed on Pd deposition, compared to that observed for the $CeO_{1.91}$ thin films (Figure 8.1). A significant difference in the rate of increase in Ce^{3+} concentration is observed for the $CeO_{1.84}$ thin films, depending on the substrate used. For Pd deposition on the $CeO_{1.84}$/Rh(111) surface a significant increase in Ce^{3+} concentration is observed after 1 MLE Pd deposition, with the Ce^{3+} concentration reaching a maximum after 2 MLE Pd is deposited, and then remaining constant as the Pd coverage is increased. This trend is very similar to that observed for Pd deposition on $CeO_{1.91}$ thin films, suggesting that the Pd is growing in the same way. However, for Pd deposition on the $CeO_{1.84}$/Pt(111) surface the initial significant increase in Ce^{3+} concentration is not observed, and instead it increases steadily and does not appear to have reached a maximum by a Pd coverage of 10 MLE. This difference in behaviour between the $CeO_{1.84}$/Pt(111) and $CeO_{1.84}$/Rh(111) surfaces could be attributed to a substrate induced difference in chemical

behaviour, however the fact that there were no such differences for the $CeO_{1.91}$ thin films is suggestive of an alternative explanation. The two $CeO_{1.84}$ thin films were produced using different methods. The $CeO_{1.84}$/Pt(111) surface was produced by annealing the $CeO_{1.91}$ thin film, causing oxygen desorption from the surface. Reduction of the $CeO_{1.91}$ thin film grown on Rh(111) by annealing in UHV was attempted, however this resulted in an insignificant change in oxidation state and the LEED pattern changed, which is undesirable. The $CeO_{1.84}$ thin film grown on Rh(111) was therefore produced by depositing Ce in a lower oxygen pressure than that used to produce the $CeO_{1.91}$ thin film. These two very different methods of producing a more reduced CeO_{2-x} thin film are likely to have produced thin films with different surface morphologies, although in both cases a 1.4 × 1.4 LEED pattern was observed, indicating the same long range order. Such a difference in surface morphology could lead to a difference in the Pd growth mode on the CeO_{2-x} surface, and hence a difference in the increase of Ce^{3+} concentration.

CO adsorption

It was shown for CeO_{2-x} thin films grown on Pt(111) and Rh(111) that CO adsorbed on the Pd nanoclusters in preference to on the CeO_{2-x} surface. After CO adsorption, no significant differences in C 1s and Pd 3d XP spectra between the Pd/CeO_{2-x}/Pt(111) and Pd/CeO_{2-x}/Rh(111) surfaces were observed. It is also interesting to note that in a study of CO dissociation on a Rh/CeO_{2-x}/Ru(0001) surface by Mullins *et al.* [2] it was concluded that the degree of CO dissociation was independent of the size and morphology of the Rh clusters. This could suggest that even though altering the CeO_{2-x} oxidation state could alter the Pd cluster morphology, this will not alter the chemical interaction between the Pd and the CO. However, it has been found that partial reduction of CeO_2(111) influences the interaction of CO with supported Rh nanoparticles [6]. The oxidation state of the CeO_{2-x} therefore appears to be the most important factor when it comes to the catalytic activity of the model catalyst.

Future work

STM will be used to image the CeO_{2-x} thin films discussed in this thesis. Other groups using the same growth method as used for $CeO_{1.91}$ thin films on Pt(111) and Rh(111) have well characterised this surface and studied it using STM. Particular interest will therefore be paid to the surface structure of the further reduced thin films, which have not previously been imaged using STM. Further studies of how Pd grows on these thin films will also be carried out using STM. This could also clarify reasons for the observed differences in Ce^{3+} concentration when Pd is deposited on $CeO_{1.84}$ grown on Pt(111) and Rh(111). Experiments monitoring the surface interactions during the CO oxidation reaction, and comparing the reactivity of the CeO_{2-x}/Pt(111) and CeO_{2-x}/Rh(111) surfaces, will be used to clarify whether or not the substrate effects the chemical behaviour of the CeO_{2-x}.

NC-AFM will also be used to image CeO_{2-x}(111) thin films and bulk CeO_2(111) in order to test the degree to which the CeO_{2-x} thin films mimic the surface of a bulk CeO_2(111) single crystal.

References

1. Schoiswohl, J., Surnev, S., and Netzer, F.P., *Reactions on inverse model catalyst surfaces: Atomic views by STM.* Topics in Catalysis, 2005. **36**(1-4): p. 91.
2. Mullins, D.R. and Overbury, S.H., *CO dissociation on Rh deposited on reduced cerium oxide thin films.* J. Catal., 1999. **188**: p. 340.
3. Mullins, D.R., Overbury, S.H., and Huntley, D.R., *Electron spectroscopy of single crystal and polycrystalline cerium oxide surfaces.* Surf. Sci., 1998. **409**: p. 307.
4. Eck, S., Castellarin-Cudia, C., Surnev, S., Ramsey, M.G., and Netzer, F.P., *Growth and thermal properties of ultrathin cerium oxide layers on Rh(111).* Surf. Sci., 2002. **520**(3): p. 173.
5. Berner, U. and Schierbaum, K.-D., *Cerium oxides and cerium-platinum surface alloys on Pt(111) single-crystal surfaces studied by scanning tunneling microscopy.* Phys. Rev. B, 2002. **65**: p. 235404.
6. Stubenrauch, J. and Vohs, J.M., *Interaction of CO with Rh supported on stoichiometric and reduced $CeO_2(111)$ and $CeO_2(100)$ surfaces.* J. Catal., 1996. **159**: p. 50.

Appendix : CeO_2 film thickness calculations

The following parameters are used to calculate CeO_2 film thickness on a Pt(111) substrate:

Parameter	**Value**
angle between surface perpendicular and the detector	$\theta = 0$
area of the adsorbate	Area under Ce 3d XPS peaks
area of the substrate	Area under Pt 4f XPS peaks
photoionisation cross section for the adsorbate	$\sigma_{Ce\ 3d} = 1.1$ Mb
photoionisation cross section for the substrate	$\sigma_{Pt\ 4f} = 0.3792$ Mb
atom size of the adsorbate	a = 0.326 nm
kinetic energy of the adsorbate	$KE_{Ce\ 3d} = 350$ eV
kinetic energy of the substrate	$KE_{Pt\ 4f} = 1172$ eV

The following parameters are used to calculate CeO_2 film thickness on a Rh(111) substrate:

Parameter	**Value**
angle between surface perpendicular and the detector	$\theta = 0$
area of the adsorbate	Area under Ce 3d XPS peaks
area of the substrate	Area under Rh 3d XPS peaks
photoionisation cross section for the adsorbate	$\sigma_{Ce\ 3d} = 1.1$ Mb
photoionisation cross section for the substrate	$\sigma_{Rh\ 3d} = 0.321$ Mb
atom size of the adsorbate	a = 0.326 nm
kinetic energy of the adsorbate	$KE_{Ce\ 3d} = 350$ eV
kinetic energy of the substrate	$KE_{Rh\ 3d} = 945$ eV